Louisiana State University
LSU Digital Commons

LSU Historical Dissertations and Theses | Graduate School

1983

Computer Analysis of Coastal Ocean Features in Synthetic Aperture Radar Imagery (Japan, Gotoh Islands).

Gary Arthur Mastin
Louisiana State University and Agricultural & Mechanical College

Follow this and additional works at: https://digitalcommons.lsu.edu/gradschool_disstheses

Recommended Citation
Mastin, Gary Arthur, "Computer Analysis of Coastal Ocean Features in Synthetic Aperture Radar Imagery (Japan, Gotoh Islands)." (1983). *LSU Historical Dissertations and Theses*. 3897.
https://digitalcommons.lsu.edu/gradschool_disstheses/3897

This Dissertation is brought to you for free and open access by the Graduate School at LSU Digital Commons. It has been accepted for inclusion in LSU Historical Dissertations and Theses by an authorized administrator of LSU Digital Commons. For more information, please contact gradetd@lsu.edu.

INFORMATION TO USERS

This reproduction was made from a copy of a document sent to us for microfilming. While the most advanced technology has been used to photograph and reproduce this document, the quality of the reproduction is heavily dependent upon the quality of the material submitted.

The following explanation of techniques is provided to help clarify markings or notations which may appear on this reproduction.

1. The sign or "target" for pages apparently lacking from the document photographed is "Missing Page(s)". If it was possible to obtain the missing page(s) or section, they are spliced into the film along with adjacent pages. This may have necessitated cutting through an image and duplicating adjacent pages to assure complete continuity.

2. When an image on the film is obliterated with a round black mark, it is an indication of either blurred copy because of movement during exposure, duplicate copy, or copyrighted materials that should not have been filmed. For blurred pages, a good image of the page can be found in the adjacent frame. If copyrighted materials were deleted, a target note will appear listing the pages in the adjacent frame.

3. When a map, drawing or chart, etc., is part of the material being photographed, a definite method of "sectioning" the material has been followed. It is customary to begin filming at the upper left hand corner of a large sheet and to continue from left to right in equal sections with small overlaps. If necessary, sectioning is continued again—beginning below the first row and continuing on until complete.

4. For illustrations that cannot be satisfactorily reproduced by xerographic means, photographic prints can be purchased at additional cost and inserted into your xerographic copy. These prints are available upon request from the Dissertations Customer Services Department.

5. Some pages in any document may have indistinct print. In all cases the best available copy has been filmed.

University Microfilms International
300 N. Zeeb Road
Ann Arbor, MI 48106

Reproduced with permission of the copyright owner. Further reproduction prohibited without permission.

Reproduced with permission of the copyright owner. Further reproduction prohibited without permission.

8400129

Mastin, Gary Arthur

COMPUTER ANALYSIS OF COASTAL OCEAN FEATURES IN SYNTHETIC APERTURE RADAR IMAGERY

The Louisiana State University and Agricultural and Mechanical Col. PH.D. 1983

University
Microfilms
International 300 N. Zeeb Road, Ann Arbor, MI 48106

Reproduced with permission of the copyright owner. Further reproduction prohibited without permission.

Reproduced with permission of the copyright owner. Further reproduction prohibited without permission.

PLEASE NOTE:

In all cases this material has been filmed in the best possible way from the available copy. Problems encountered with this document have been identified here with a check mark __√__.

1. Glossy photographs or pages ____✓____
2. Colored illustrations, paper or print _____
3. Photographs with dark background ____✓____
4. Illustrations are poor copy _____
5. Pages with black marks, not original copy _____
6. Print shows through as there is text on both sides of page _____
7. Indistinct, broken or small print on several pages ____✓____
8. Print exceeds margin requirements _____
9. Tightly bound copy with print lost in spine _____
10. Computer printout pages with indistinct print _____
11. Page(s) _____ lacking when material received, and not available from school or author.
12. Page(s) _____ seem to be missing in numbering only as text follows.
13. Two pages numbered _____. Text follows.
14. Curling and wrinkled pages _____
15. Other _____

University
Microfilms
International

Reproduced with permission of the copyright owner. Further reproduction prohibited without permission.

Reproduced with permission of the copyright owner. Further reproduction prohibited without permission.

COMPUTER ANALYSIS OF COASTAL OCEAN FEATURES

IN

SYNTHETIC APERTURE RADAR IMAGERY

A Dissertation

Submitted to the Graduate Faculty of the
Louisiana State University and
Agricultural and Mechanical College
in partial fulfillment of the
requirements for the degree of
Doctor of Philosophy

in

Engineering Science

by
Gary A. Mastin
B.A., Ottawa University, 1976
M.S.E.E., University of Missouri - Columbia, 1977
August 1983

Reproduced with permission of the copyright owner. Further reproduction prohibited without permission.

ACKNOWLEDGEMENTS

Special thanks must be given to a number of individuals and organizations that have supported this research task. I am greatly indebted to the Office of Naval Research for financial support and to the Japan Self Defense Air Force for a first class job of collecting the SAR data. Mr. Milt Hoover and Mr. Ralph Reid of the Goodyear Aerospace Arizona Division contributed greatly by making the precision optical correlator available and by providing guidance during data preprocessing. Image digitization services provided by the Remote Sensing Branch of NORDA at NSTL Station, Mississippi, during the repair of the LSU camera system were instrumental in the timely completion of this research. My Ph.D. committee has proven to be an exceptionally instructive and cooperative group of professionals. Dr. Oscar Huh contributed many hours of organizational, technical and moral support above and beyond the call of duty. I also wish to express my deep appreciation to Dr. Charles Harlow who, while at the University of Missouri-Columbia and Louisiana State University, proved to be a valuable and compassionate advisor.

Graditude must also be expressed to several close friends and family members for their support. Mrs. Cynthia Deville, Mr. Don Middleton and Mr. George Ohrberg will always be remembered for keeping the computer up, and therefore my morale. Mrs. Norma Duffy, who drafted the figures in this dissertation, also has been an enjoyable companion. My wife, Jeanette, has been a source of continual support and has

Reproduced with permission of the copyright owner. Further reproduction prohibited without permission.

contributed to proofreading the text. Finally, and most importantly, the author acknowledges the many years of love, money and time invested by his parents, Mary Helen and Arthur W. Mastin, to whom this dissertation is dedicated.

Reproduced with permission of the copyright owner. Further reproduction prohibited without permission.

TABLE OF CONTENTS

Reproduced with permission of the copyright owner. Further reproduction prohibited without permission.

Reproduced with permission of the copyright owner. Further reproduction prohibited without permission.

LIST OF TABLES

Reproduced with permission of the copyright owner. Further reproduction prohibited without permission.

LIST OF FIGURES

Reproduced with permission of the copyright owner. Further reproduction prohibited without permission.

Reproduced with permission of the copyright owner. Further reproduction prohibited without permission.

Reproduced with permission of the copyright owner. Further reproduction prohibited without permission.

Reproduced with permission of the copyright owner. Further reproduction prohibited without permission.

Reproduced with permission of the copyright owner. Further reproduction prohibited without permission.

Reproduced with permission of the copyright owner. Further reproduction prohibited without permission.

Reproduced with permission of the copyright owner. Further reproduction prohibited without permission.

Reproduced with permission of the copyright owner. Further reproduction prohibited without permission.

ABSTRACT

A wide variety of oceanographic phenomena is revealed in synthetic aperture radar (SAR) ocean imagery. Four basic classes of SAR oceanographic phenomena, surface waves, fronts, wind patterns and internal waves, are of oceanographic interest. These classes are defined in light of their generation mechanisms and as a function of Bragg scattering, which accounts for their visualization in SAR ocean imagery. Digital exploitation of SAR imagery offers image enhancement and parameter extraction capabilities and is currently an area of extensive research. The state of the art in digital exploitation of SAR imagery is reviewed, with special attention to SAR speckle reduction and ocean parameter extraction.

Digital processing of SAR optically processed imagery gathered over the Gotoh Islands of Japan is the focus of the dissertation research. Preprocessing is done to digitize the imagery, correct for digitization shading nonlinearities, convert the imagery from the radar slant-plane to the ground-plane, and correct for antenna range dependent power attenuation that may be present. Power spectral techniques are employed to extract wind direction and wavelength, and to estimate wave period, phase speed, wave height, and aerodynamic parameters associated with sea surface roughness through proven empirical models. Imagery with spectra and associated ocean parameters superimposed is generated digitally. Texture analysis techniques are studied to

Reproduced with permission of the copyright owner. Further reproduction prohibited without permission.

determine their applicability to SAR ocean image parameter extraction. The inertia texture measure is shown theoretically and experimentally to extract wavelength. Other texture measures are analyzed for their ability to further characterize image periodicities.

Reproduced with permission of the copyright owner. Further reproduction prohibited without permission.

INTRODUCTION

This dissertation is conceptually divided into two parts, background and new research. Chapters 1, 2, 3, and the appendix present the background information. Chapter 1 reviews the oceanographic problem. It seeks to answer three questions:

1. What are the ocean features we see in synthetic aperture radar imagery?
2. How are the features formed?
3. Why are these features important?

This chapter should be of particular interest to the engineering community whose members are not familiar with oceanic processes. Chapter 2 reviews the state of the art in synthetic aperture radar digital processing. The reader should note the breadth, yet relatively shallow depth, of the unclassified work in synthetic aperture radar digital exploitation. Of special interest is some research performed by the author comparing several coherent speckle reduction algorithms to aid in computer marking of oceanic frontal boundaries. Chapter 3 is an overview of the data preprocessing performed on the imagery analyzed in chapters 4 and 5. Preprocessing encompasses all image manipulations from precision optical correlation through image digitization and geometric correction. The appendix simply presents some basic synthetic aperture radar physics concepts referred to in the dissertation. New research, representing the dissertation's unique contributions, is

Reproduced with permission of the copyright owner. Further reproduction prohibited without permission.

conceptually subdivided in Chapters 4 and 5. Chapter 4 concentrates on geophysical analysis, primarily of interest to the oceanographic community. Chapter 5 concentrates on digital image texture analysis techniques and focuses on the digital image analysis community. Chapter 6 concludes the research in Chapters 4 and 5 and makes recommendations for future work.

Reproduced with permission of the copyright owner. Further reproduction prohibited without permission.

CHAPTER 1

STUDIES OF OCEANOGRAPHIC PHENOMENA AFFECTING SAR SYSTEMS

The task at hand is to identify a limited set of geophysical phenomena of importance to activities in the coastal environment, to link these phenomena to distinctive SAR sea image patterns and to uniquely characterize these image patterns for the purpose of remotely sensing sea states. A limited number of geophysical phenomena combine to create a sea state, but due to the physics of the SAR imaging system, only a few of them are manifested in SAR coastal imagery. Research by SAR ocean imagery investigators has established qualitative links between a few observed SAR image patterns and suspected forcing phenomena. In a few instances supporting information such as maps or surface data has been available to link surface phenomena to image patterns. In most cases the link is subjective and based on the interpretation of an experienced oceanographer.

Four broad classes of SAR image patterns have been chosen in this study. They are:

1. Surface Waves
2. Wind Patterns
3. Internal Waves
4. Oceanic Fronts

The choice of these classes is based on two criteria; 1) the

Reproduced with permission of the copyright owner. Further reproduction prohibited without permission.

detectability of surface waves, wind patterns, internal waves and slicks and 2) the importance of these features to the scientific community.

The following discussion defines the various subclasses of each feature class, describes their manifestation in SAR imagery, and substantiates their importance. It begins with a review of surface waves, the most widespread and fundamental SAR coastal image feature. Theories on surface wave creation are outlined first. The Bragg scattering mechanism, which creates SAR sea return, is also presented, as is the concept of Bragg wave modulation by underlying long waves and its impact on coastal SAR imagery. Then, subclasses of each of the four basic pattern classes that are, or should be, detectable in SAR coastal imagery, are discussed. The subclass discussions are presented to review some basic hydrodynamic and meteorologic processes and to substantiate the value of image analysis of their SAR patterns.

1.1 Surface Waves

One of the most interesting discoveries resulting from the application of SAR to environmental sensing has been surface wave patterns. Crombie [1] was the first to document and hypothesize the mechanism of surface wave radar return. The first order Bragg scattering theory is based upon his observations. Bragg scattering theory tells us that small scale waves (less than 25 cm) of a specific wavelength are responsible for the radar return. The Bragg scatterers are modulated by the underlying longer waves. The late J.W. Wright and his associates at the Naval Research Laboratory have studied this phenomenon extensively and are developing models for two-scale

Reproduced with permission of the copyright owner. Further reproduction prohibited without permission.

scattering that relate directly to SAR imaging [7,20]. A number of theoreticians involved in SAR performance have also joined the modeling effort [9,11]. SAR practitioners continue in an effort to correlate hydrologic and meteorologic factors with SAR surface wave patterns, hoping to extract wave spectra and ocean parameters such as wave direction, wavelength and phase speed. A number of important questions have yet to be completely answered, such as:

1. Do the alternating light and dark wave patterns correspond to crests and troughs?
2. How do wave patterns vary with direction of propagation from the antenna, with velocity, with antenna depression angle, and with radar polarization?

Final answers to these questions will have a profound impact on SAR image analysis but even in their absence, many SAR image patterns demonstrate well known surface wave characteristics, such as refraction, diffraction and breaking , and thereby give valuable clues to wave direction, bathymetry and local meteorological conditions.

The research goal is to analyze image characteristics created by surface waves and measure significant wave parameters which can be used to identify and distinguish specific classes of ocean features. The number of environmental driving forces and modification processes of surface waves is large and the identification of all of these is beyond the scope of this chapter. Of primary interest here are those forces and processes that express themselves as features detectable in SAR imagery. It must be noted that driving forces and modification processes cannot be separated from the radar imaging process. Different factors often affect different imaging geometries. The following

Reproduced with permission of the copyright owner. Further reproduction prohibited without permission.

paragraphs discuss the role of wind straining in wave evolution, present the Bragg scattering theory and consider the modulation of the scatterers by underlying longer waves.

1.1.1. Wind Straining and Wave Evolution

Energy exchanges at the boundary layer between surface winds and the underlying fluid surface account for the existence of almost all waves. Many theories on wave evolution that trace wave growth from capillaries to fully developed seas have been published. Kraus [2] identifies three basic evolutionary mechanisms. The first are resonant interactions. Phillips [3] recognized that turbulent eddies in the mean airflow have components that can resonate with an induced water disturbance, thereby producing ocean surface pressure fluctuations causing wave growth. The resonant theory predicts that the surface wave spectrum will increase linearly with time (or fetch). Initially, the turbulent eddies generate high wave number (short wavelength) components which have slow phase speeds and propagate at many angles with respect to the mean wind direction. With time, the shorter waves saturate and stop growing, while the overall trend is for longer waves propagating in the mean wind direction to continue growing.

The second evolutionary mechanisms are induced interactions. Random pressure fluctuations create wave perturbations over the water, which perturb the mean airflow, thereby inducing new pressure fluctuations which are not random, but linked to the wave structure. Near wave crests, wind streamlines are denser, the wind velocity is faster and the Bernoulli effect accounts for a pressure reduction. The opposite occurs in the troughs. Inertial forces associated with

Reproduced with permission of the copyright owner. Further reproduction prohibited without permission.

streamline curvature balance perturbation pressures,and the system experiences equilibrium, except in a thin air layer at a critical height above the waves. This air layer is called the "matched layer" and is characterized by vorticity. Downward moving air in the matched layer has less vorticity than upward moving air, i.e. vorticity is not conserved. The energy deficit associated with the differing vorticity levels is accounted for by the downward flux of momentum to the air-sea interface. In other words, momentum is supplied to the surface waves from the wind through the matched layer, thereby contributing to wave growth. Induction has been shown to be most effective upon slow and short waves whose matched level is close to the air-sea interface.

The third mechanism is called the maser mechanism of wave generation. This mechanism is principally espoused by Longuet-Higgins [4,5,6]. It addresses three observed phenomena that cannot be associated with the resonance and induction processes:

1. Waves develop faster, or within a shorter fetch, than predicted by resonance and induction,
2. The growth of wave spectral components is not monotonic,
3. Some waves move faster than the wind.

One cause in the discrepancies between these observations and the previously discussed theories is the interaction between waves of different lengths moving in the same direction. The maser mechanism considers the case where short waves interact with very long waves, where the orbital velocities of the longer waves affect energy transport by the short wave components in the same way as an oscillating current. Energy is transferred locally from the short to the long

Reproduced with permission of the copyright owner. Further reproduction prohibited without permission.

waves at a rate which is a function of the modulated short wave momentum change and the local long wave orbital velocity. Short wave energy is concentrated on the forward slope of the long waves which can lead to local breaking there. Breaking causes all the short wave energy and momentum to be impulsively transferred to the horizontal component of the long wave orbital velocity. Momentum is transferred from higher to lower frequency waves in stages. Those waves having the highest orbital velocity components ultimately receive the momemtum. The convergence of energy into the region of the spectral peak over time is comparable to the action of a maser, hence the name.

1.1.2 Bragg Scattering

The fundamental process of SAR ocean imaging is Bragg scattering [1]. When a uniform radar wave is incident on a plane surface roughened by ocean waves, only a single component of the surface wave system with a finite band width contributes to the scattered power. This component is called the Bragg wave. The Bragg condition, which expresses the Bragg wavelength, λ_w, as a function of the radar wavelength, λ_o, the depression angle, θ, and the look angle relative to the surface waves, ϕ, can be readily developed from inspection of Figures 1-1 and 1-2.

For backscattering of the coherent microwave signal, the path of transmittance, $\vec{BC}$, plus the path of backscatter, $\vec{CB}$, must be an integer multiple, n, of the microwave length. The adjacent side of the triangle is therefore of length $(n\lambda_o)/2$. Solving for θ we find,

$$\cos\theta = \frac{n\lambda_o}{2L} \qquad (1\text{-}1)$$

Reproduced with permission of the copyright owner. Further reproduction prohibited without permission.

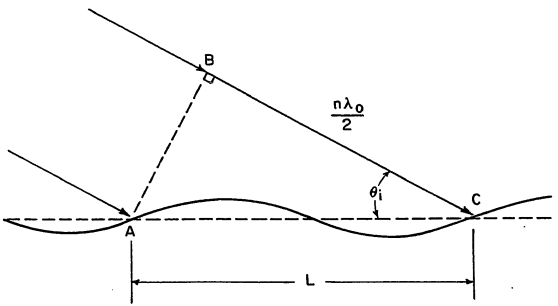

Figure 1-1. Scattering geometry.

Reproduced with permission of the copyright owner. Further reproduction prohibited without permission.

Furthermore,

$$\cos \phi = \frac{\lambda_w}{L} \qquad (1\text{-}2)$$

where L is the perceived ocean wavelength in the look direction as shown in Figure 1-2 [7]. Substituting equation (1-2) and (1-1), we get

$$\cos \theta = \frac{n\lambda_o \cos\phi}{2\lambda_w} \quad . \qquad (1\text{-}3)$$

For an x-band radar having a grazing angle of 45 degrees looking normal to the wave crests and n=1, λ_w=2.3 cm. Making use of the well known physics expression $\nu = V/\lambda$, where v is the propagation velocity,

$$\cos \theta = \frac{nc\nu_w \cos\phi}{2\nu_o V} \qquad (1\text{-}4a)$$

$$\nu_w = \frac{2n'\nu_o V_w \cos\theta}{c \cos\phi} \quad . \qquad (1\text{-}4b)$$

Thus, the frequency of the water wave detected is a function of the grazing angle, look angle, radar frequency and Bragg wave velocity.

It can be shown that the frequency of the Bragg wave is identical to the Doppler shift of a water wave traveling with a radial phase velocity, V_r. If an observer is positioned on the crest of an ocean wave and the observer is illuminated with microwaves, and both the observer and the source are at rest, then the observer receives $(ct)/\lambda_o$ microwaves in a time t, where c is the microwave velocity. If one then considers the frame of reference of the observer on a wave traveling toward the source, the observer perceives the movement of the source toward the wave, which results in an additional $(V_r\ t)\lambda_o$

Reproduced with permission of the copyright owner. Further reproduction prohibited without permission.

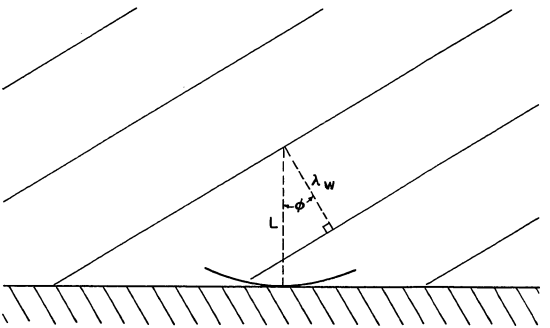

Figure 1-2. Look angle geometry.

Reproduced with permission of the copyright owner. Further reproduction prohibited without permission.

waves in the same time, t. The frequency detected by the observer (wave) is then,

$$\nu' = \frac{(ct)/\lambda_o + (V_r t)/\lambda_o}{t} \tag{1-5}$$

$$= \nu_o + \frac{V_r \nu_o}{t} \tag{1-6}$$

and the Doppler shift is given as

$$\Delta\nu = \frac{V_r \nu_o}{c} \tag{1-7}$$

In the case of backscatter, two shifts occur: one received at the wave surface as a result of the apparent motion of the source toward the wave, and one received at the antenna because of the apparent motion of the new source (scattering wave) toward the receiver. For backscattering, equation (1-7) becomes,

$$\Delta\nu = \frac{2V_r \nu_o}{c} \tag{1-8}$$

Now V_r is related to the slant-range perceived velocity, V_{rw}, by the expression,

$$V_r = V_{rw} \cos\theta \tag{1-9}$$

Making use of the look angle relationship shown in Figure 1-2, equation (1-9) becomes,

$$V_r = V_w \frac{\cos\theta}{\cos\phi} \tag{1-10}$$

so the Doppler shift detected by the radar is given by,

Reproduced with permission of the copyright owner. Further reproduction prohibited without permission.

$$\Delta\nu = \frac{2V_o V_w \cos\theta}{c \cos\phi} \quad . \qquad (1\text{-}11)$$

For n'=1, equations (1-4b) and (1-11) are equivalent, and we can see that the Bragg wave velocity is a function of the grazing angle, look angle, radar frequency and the radar Doppler shift.

An interesting observation is the effect of increasing ϕ from 0 to 90 degrees. Referring to equation (1-3),

$$\lambda_w = \frac{n\lambda_o \cos\phi}{2 \cos\theta} \quad . \qquad (1\text{-}3a)$$

For waves traveling in the antenna look direction, the Bragg wave has its maximum length, but decreases to zero at normal incidence. In the frequency domain, this corresponds to a Doppler shift approaching an indeterminant value. Practically speaking, the first order Bragg scattering model tells us that a backscattered signal can only be detected when there is a small scale wave component normal to the antenna.

1.1.3 Orbital Wave Motion

The orbital motion of ocean waves inherent in simple harmonic representations of ocean waves has a profound effect on the SAR imaging mechanism. Its impact is based on Doppler processing done by the SAR processor to resolve targets in the azimuth (along track) dimension. The unique feature which gives SAR its high azimuthal resolution is described in the following discussion and the impact of orbital motion on the SAR image summarized.

Reproduced with permission of the copyright owner. Further reproduction prohibited without permission.

Consider two points separated in the azimuth dimension as shown in Figure 1-3. If the radar emits a sinusoidal frequency, ν_o, then the receiver detects the instantaneous Doppler shifted frequency, ν_D, given by,

$$\nu_D = \frac{2V\nu_o \cos\gamma}{c} \tag{1-12}$$

which follows a similar development to that of the previous section. For reflection from the points P1 and P2 we get,

$$\nu_{D1} = \frac{2V\nu_o}{c} \cos\gamma_1 \tag{1-12a}$$

$$\nu_{D2} = \frac{2V\nu_o}{c} \cos\gamma_2 \tag{1-12b}$$

The frequency difference between these two scatterers is then,

$$\Delta\nu' = \nu_{D2} - \nu_{D1} = \frac{2V\nu_o}{c} (\cos\gamma_2 - \cos\gamma_1) \tag{1-13}$$

For γ sufficiently large, $R_s \doteq R_1 \doteq R_2$. Recognizing that,

$$\cos\gamma_i = \frac{X_i}{R_s} \tag{1-14}$$

we see

$$\Delta\nu' = \frac{2V\nu_o}{cR_s} (X_2 - X_1) \tag{1-15}$$

$$= \frac{2V}{\lambda_o R_s} \Delta X \tag{1-16}$$

At any range R_s, points in azimuth are linearly resolvable as a function of instantaneous Doppler shift differences. It must be noted

Reproduced with permission of the copyright owner. Further reproduction prohibited without permission.

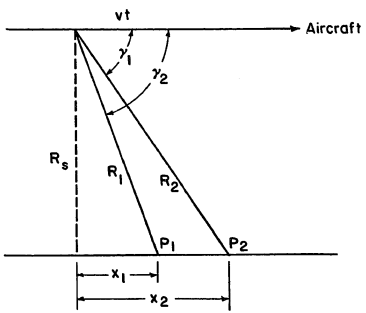

Figure 1-3. Azimuthal resolution in the slant-plane.

Reproduced with permission of the copyright owner. Further reproduction prohibited without permission.

that this analysis depends on stationary scatterers to preserve the Doppler history. Should a scatterer move during the investigation time, the Doppler shift in equation (1-12) cannot be attributed solely to the motion of the aircraft. This results in a miscalculation of ΔX in equation (1-16) which corresponds to misplacement of the scatterers in the azimuth dimension of the SAR image [7,8,9].

Orbital wave motion results in just such a misplacement. Consider the case of swell propagating in the azimuth dimension, as shown in Figure 1-4. From the discussions in the preceding section, it is clear that the Bragg wavelength is short enough that swell alone cannot account for a radar return. Rather, it is the modulation of Bragg waves by the underlying swell that accounts for swell detection in SAR imagery. For the purposes of this discussion, a uniformly distributed scattering field is assumed. Swift [9] and Alpers [10] have investigated this hypothetical situation in some detail. Due to the length of the mathematical discussions involved, the developments will not be shown here; however, their results show the significance of orbital velocities in SAR imagery.

The water particles in the ocean very nearly move in closed circles, as shown in Figure 1-4. The velocity vectors associated with this motion are shown in Figure 1-5. Because the velocity is greater at the top than the bottom of the orbit, the net wave path is lateral. Of particular interest to the SAR is the nonuniform radial velocity component in azimuth, also shown in Figure 1-5. This results in scatterers being shifted nonuniformly in the azimuth dimension of the image plane, as alluded to above, and gives rise to variations in intensity patterns parallel to swell crests and troughs. Alpers [11]

Reproduced with permission of the copyright owner. Further reproduction prohibited without permission.

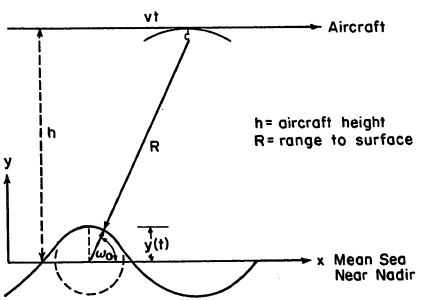

Figure 1-4. Azimuthal swell propagation.

Reproduced with permission of the copyright owner. Further reproduction prohibited without permission.

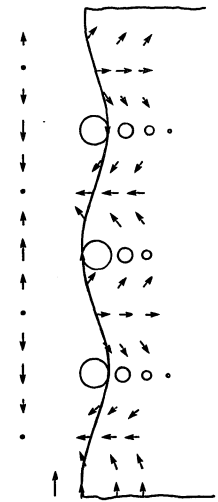

Figure 1-5. Instantaneous velocity vectors and orbital paths, adapted from Neumann [14].

Reproduced with permission of the copyright owner. Further reproduction prohibited without permission.

describes this phenomenon as "velocity bunching". Swift [9] portrays the placement and relative intensities of these patterns in Figures 1-6 and 1-7. The parameter ζ is the ratio of ocean wave amplitude to wavelength and the value of ζ increases with increasing orbital velocity. The important points may be summarized as follows:

1. In the idealized case of azimuth propagating swell and uniformly distributed scatterers, intensity peaks in SAR imagery vary in magnitude and placement as a function of radial velocities induced by orbital motion.
2. For the deep ocean scenario, as demonstrated in Figure 1-6, single peaks align with the swell troughs.
3. For the shallow ocean scenario, as demonstrated in Figure 1-7, multiple peaks per wavelength may appear.

Thus far the case of azimuth traveling swell rather than range traveling has been considered. In the range case, nonuniform radial velocity components exist in the range dimension which alter the Doppler history and therefore create an azimuth shift. For swell having only a range component, this results in spatial displacement along the image intensity peaks. Unlike the azimuthal propagating case, displacement of intensity peaks from wave crests is not encountered.

The above listed factors, coupled with environmental modification processes such as refraction, diffraction, etc.,create SAR surface wave patterns. Despite what appears to be an unmanageable set of variables, SAR imaged surface waves demonstrate consistent patterns due to environmental modification related to bathymetry. Waves diffracted or refracted tend to have long crestlengths and wavelengths that vary in a

Reproduced with permission of the copyright owner. Further reproduction prohibited without permission.

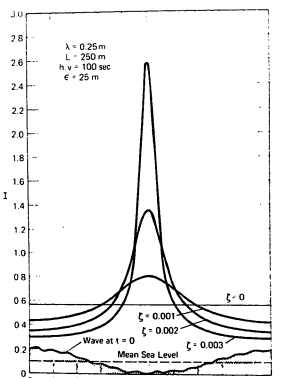

Figure 1-6. Image intensity versus normalized distance along a propagating ocean wave of uniform scattering cross section. From Swift [9].

Reproduced with permission of the copyright owner. Further reproduction prohibited without permission.

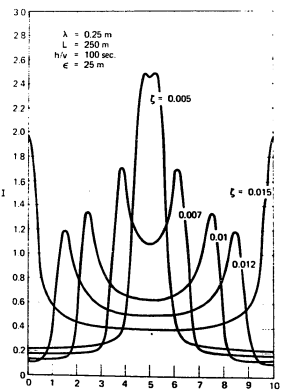

Figure 1-7. Image intensity versus normalized distance along a propagating ocean wave of uniform scattering cross section. From Swift [9].

Reproduced with permission of the copyright owner. Further reproduction prohibited without permission.

predictable manner. Open water waves usually have short crestlengths, probably due to the complex superposition of several different wave trains propagating in various directions, and wavelengths are often difficult, if not impossible to define. Figures 1-8 through 1-10 demonstrate the visual consistency of these patterns for different locations and different days. Our ability to visually extract data such as crestlength or wavelength gives credence to the stated research task of extracting significant wave parameters, although the full range of extractable parameters and their reliability is unknown. The ability of the computer to analyze scenes more quantitatively and consistently than a human interpreter may result in defining measures that uniquely characterize surface wave patterns which are imperceivable to the human interpreter. The long range potential of this research may be an automatic image segmentation algorithm which can flag surface wave patterns in desired classes and present wave parameters of interest to navigation, coastal engineering and military operations.

1.2 Wind Patterns

Wind patterns and slicks are grouped together because several wind patterns owe their visibility to the concentration of sea surface material by the wind. Slicks also play a significant role in the identification of internal waves, but this will be discussed in the following section.

The three categories of wind patterns, wind rows, wind streaks and random turbulence zones, are water surface perturbations involving relatively small masses of water whose oscillations are governed, not so much by gravity, but by surface tension. As mentioned in the previous

Reproduced with permission of the copyright owner. Further reproduction prohibited without permission.

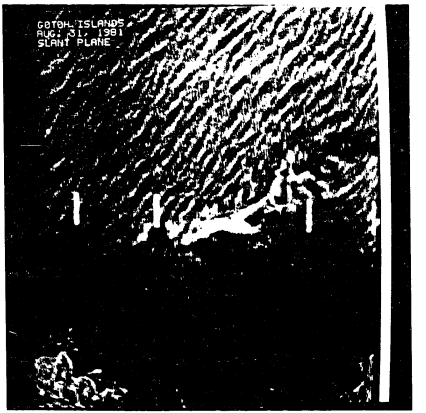

Figure 1-8. SAR image near Fukuejima in the Gotoh Islands of Japan. Note the change in crest length when going from open water to coastal water. Also note the diffraction caused by the small island.

Reproduced with permission of the copyright owner. Further reproduction prohibited without permission.

Figure 1-9. SAR image near Fukuejima in the Gotoh Islands of Japan. The long-crested swell pattern is well defined. The periodicity of the swell pattern is consistent across the image.

Reproduced with permission of the copyright owner. Further reproduction prohibited without permission.

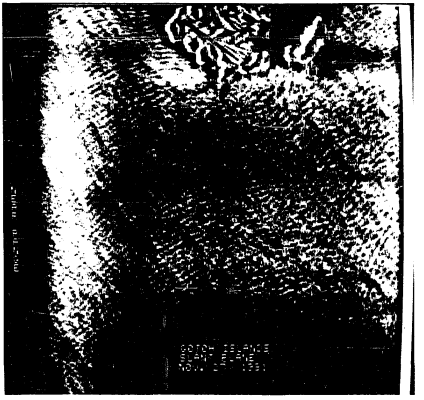

Figure 1-10. SAR image near Fukuura in the Gotoh Islands of Japan. The superposition of two swell patterns is quite evident.

Reproduced with permission of the copyright owner. Further reproduction prohibited without permission.

section, wind waves have a profound effect on the momentum exchange between the atmosphere and the sea surface.

Wind rows are linear modifications (or destructions) of periodic surface wave patterns, or the flat sea, found in coastal areas where local topography causes blocking and funneling of surface winds. The increased wind speeds over seas downwind from topographic funnels create increased wind stress and give rise to capillaries and short fetched seas, while seas blocked from the wind have comparatively low capillary/short wavelength populations. Tilting of the stressed surfaces creates facets that reflect sunlight and make these regions visible in aerial photographs. The orientation of wind rows, as well as their structure,shows a marked dependence on wind speed and direction. Figure 1-11 is an SAR image of wind rows.

Wind streaks are periodic zones of smooth water aligned parallel to the wind direction and show a considerable permanence. They appear in appropriate locations where the wind speed exceeds about 3 to 5 m/s. Two methods of creation have been identified by Roll, both of which involve the action of the wind in concentrating surface films. The first is a system of convective rolls. Woodcock [13, 14] identified evaporative cooling due to the wind as the source of thermal instability in the surface layer of water which initiated convection. The convective vortices then concentrate oil, seaweed, etc. in convergence zones and deplete the material in divergence zones, forming alternating rows of capillary damped and wind strained seas. Figure 1-12 demonstrates this. Some evidence has also been supplied by Miles [15] showing that the convection vortices are asymmetrical, the larger vortices being the clockwise rotating ones. This has been attributed to

Reproduced with permission of the copyright owner. Further reproduction prohibited without permission.

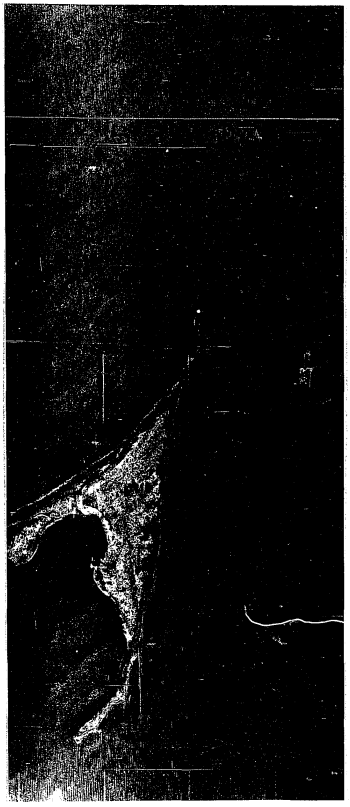

Figure 1-11. SAR image off Cape Fear. Note the wind rows in the bay. These result from topographic wind funneling.

Reproduced with permission of the copyright owner. Further reproduction prohibited without permission.

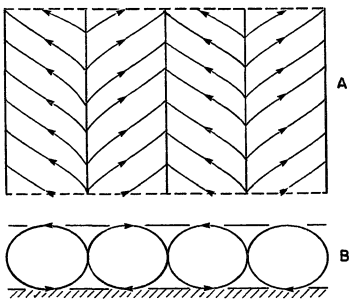

Figure 1-12. System of convective rolls in water due to wind action. a. view from above; b. side view [12].

Reproduced with permission of the copyright owner. Further reproduction prohibited without permission.

the Coriolis effect. Welander's study [16] supports the concept of wind driven circulation, although he tends to discount the Coriolis effect. Welander goes on to identify rain's effect on band dissipation. A second suggested method of creation involves slick pressure on capillaries. Stommel [17] suggested that the capillaries exert pressure on surface slick material, compressing it into streaks. This mechanism has yet to be confirmed. Figure 1-13 is an example of wind streaks taken from the Japanese data. Fu and Holt [18] also document their appearance in SEASAT SAR imagery.

Random turbulent zones encompass a wide variety of small scale capillary patterns. Terms such as "cat's paws" or "puffs" have been used to describe them. They are primarily distinguished by their short lifetimes, often on the order of a few seconds, and by their unpredictable appearance. Figure 1-14 shows an example taken from SEASAT [18].

Wind direction, wind speed, the SAR imaging geometry and Bragg scatterer suppression determine SAR wind pattern detection. The basic mechanism of wind pattern imaging is the same as that described for surface detection. The short wave components generated by the wind field saturate near underlying long wave crests. The saturated short waves are of the magnitude of SAR sensitive Bragg scatterers. Because the Bragg waves interact weakly with the underlying long waves and strongly with the wind, Bragg waves propagate at virtually any angle relative to the long wave propagation direction. This accounts for the detectability of the modulating long waves independent of the SAR squint angle. Wright [20] has studied wind speed and geometry effects in some depth. Two observations are significant in SAR wind pattern imaging:

1. Modulation of the Bragg scatterers looking downwind

Reproduced with permission of the copyright owner. Further reproduction prohibited without permission.

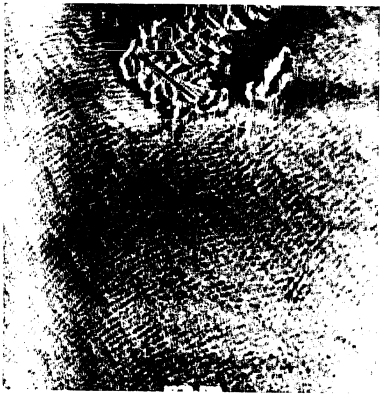

Figure 1-13. Wind streaks on the northern tip of the Gotoh Islands of Japan. Winds are from the scene's lower left at a speed of 9.9 m/s.

Reproduced with permission of the copyright owner. Further reproduction prohibited without permission.

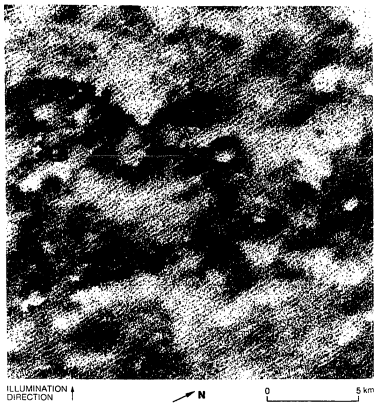

Figure 1-14. SEASAT image of "cat's paws" caused by surface wind turbulence. This image was taken at about 400 km. southwest of Vancouver, Canada [18].

Reproduced with permission of the copyright owner. Further reproduction prohibited without permission.

nearly vanishes in the midrange of wind speeds (20-45 cm/s) because the orientation and amplitudes of small waves are modulated.

2. Modulation of the Bragg scatterers, looking upwind, is higher in amplitude than for the reverse and is prominent at all wind speeds. This is because small waves in the upwind situation are tilted toward the antenna.

Shuchman [19] has done some experiments with aircraft mounted SAR that support the observations of Wright.

Slicks dampen Bragg scatterers and therefore decrease the energy returned to the radar antenna. DeLoor [23] documents the detection of oil slicks and further comments that slicks are marginally detectable under light winds and clearly discernable under stronger winds. It is likely that the contrast between damped and slick-free zones is enhanced by increased Bragg scattering in the capillary rich, slick-free zones.

Wind pattern analysis in SAR imagery has the potential for making a profound contribution to boundary-layer meteorology. A suggestion by Hsu (personal communication) is to calculate the dynamic roughness length [25],

$$z_o = \frac{a^*}{2\pi}\left[\frac{H}{(c/U_*)^2}\right] \qquad (1\text{-}17)$$

where

$$U_* = \frac{U_z k}{\ln(z/z_o)} \qquad (1\text{-}18)$$

Reproduced with permission of the copyright owner. Further reproduction prohibited without permission.

and

H = avg. wave height,

c = avg. phase velocity of the dominant wave,

U_* = shear velocity over the water,

a^* = unknown constant, approximately equal to 1,

U_z = wind speed at a height z above the surface,

k = von Karman constant,

from insitu measurements of H,c and U_*, and then to correlate SAR image textures with z_0. The dynamic roughness length, when physically interpreted, specifies the scale of the turbulent wind eddies that are generated by the surface roughness elements. Young wind-generated small scale seas tend to have high values of z_0, while well developed large scale seas support more laminar air flow and have small values of z_0. Furthermore, changes in z_0 reflect changes in thermal stratification on the wind profile over the sea. From a theoretical point of view, z_0 is important to the determination of the momentum flux which transfers energy from the wind to the seas, thereby creating waves. From a more immediately practical point of view, if z_0 and the surface wind speed U_z can be extracted from SAR image textures, then the shear velocity U_* can be used to calculate the drag coefficient, c_z, which can then be linked to wave breaking [26]. Wave breaking determines the concentration of aerosols in the boundary layer. The aerosol concentration, in turn, affects optical, microwave and accoustic propagation [27]. This is especially important to military operations in the coastal environment where the formation of internal boundary layers, due to changes in surface roughness at the coastline, alters the refractive index of air, thereby limiting the reliability of ground-based

Reproduced with permission of the copyright owner. Further reproduction prohibited without permission.

coastal radar surveillance and laser guidance systems.

The sensitivity of wind row and wind streak alignment to wind direction makes their detection important to remotely detecting surface wind direction. The large area coverage of SAR imagery allows the image analyst to determine the instantaneous wind direction at all points in the scene. Figure 1-15,taken from the Japanese data set, is an example.

Finally, capillary damping by slicks accounts for our ability to monitor pollutant propagation in coastal regions. The increased incidence of oil spills in recent years, coupled with public desire to enforce environmental protection laws, makes slick monitoring a priority in its own right.

1.3 Internal Waves

Internal waves are common in coastal regions at the horizontal interface between the more buoyant surface layer and the denser water below. Orbital motion of the propagating internal wave induces circulation in the lower density layer, thereby creating surface convergence zones halfway between each internal wave crest and the following trough [28] (Figure 1-16). In the presence of natural oils or man-made pollutants, slicks form at the convergence zones, creating bands. When the internal wave is progressive, the bands propagate at the phase speed of the internal waves. There is some evidence that internal waves orient their long axes nearly at a right angle with the wind [18]. In shallow water, their orientation may be a function of bottom topography.

Two processes can be identified which will render internal wave

Reproduced with permission of the copyright owner. Further reproduction prohibited without permission.

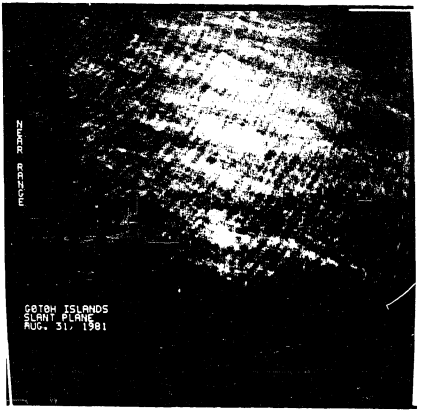

Figure 1-15. Wind rows superimposed over a swell pattern.

Reproduced with permission of the copyright owner. Further reproduction prohibited without permission.

Reproduced with permission of the copyright owner. Further reproduction prohibited without permission.

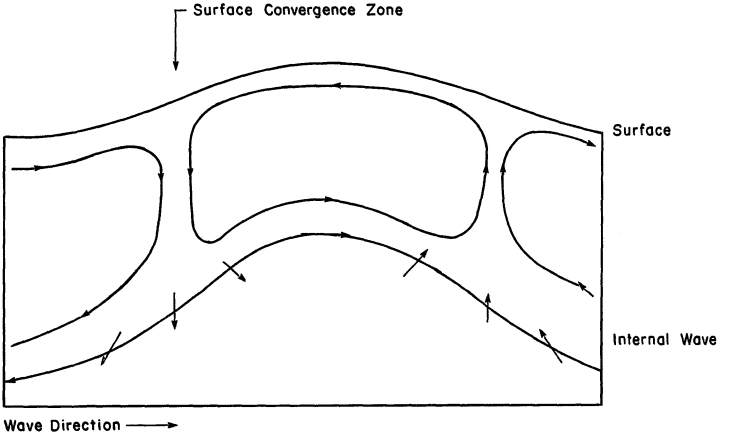

Figure 1-16. Upper layer circulation induced by the propagation of an internal wave.

patterns visible in SAR imagery. Both involve the convergence of surface circulation induced in the upper layer by the internal wave. The first process involves the presence of slick material. LaFond and LaFond [29] note that the wind stress is greater on the slick-free intervening water than on the slick, which aids in moving the surface water toward the slick and helps develop a greater convergence on the upwind side of the slick. The increased wind stress and the convergence of water at the slick band edges generates a greater population of Bragg scatterers. The contrast in scattering in the wind stressed areas versus capillary damping in the slick bands renders the internal wave pattern visible. The second process is supported by Gargett and Hughes [21,22]. They state that the surface circulation induced by the internal wave interacts with short capillary/gravity waves producing a periodic height modulation of the short capillary/gravity waves, thereby producing banded patterns of roughness and slicks. They further theorize that occasional highly-peaked, long-crested waves result from resonant interaction between surface waves overriding the internal wave.

A number of investigators have documented internal wave patterns in radar imagery. DeLoor [23] documents them in real aperture imagery of the North Sea. Gower and Hughes [24] compared SAR imagery and surface observations in the Gulf of Georgia and correlated SAR image intensity with wave height and slope. SEASAT images show internal wave patterns throughout the world in a wide variety of environments [18]. Figures 1-17 and 1-18 are examples of a SAR internal wave pattern.

1.4 Oceanic Fronts

Fronts are more complex in structure than their surface expression

Reproduced with permission of the copyright owner. Further reproduction prohibited without permission.

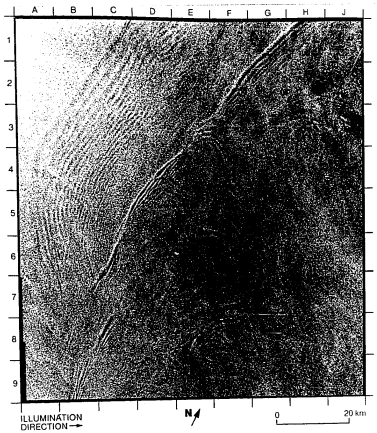

Figure 1-17. SEASAT internal wave image from the Labrador Sea about 150 km east of Hudson Straight, Canada [18].

Reproduced with permission of the copyright owner. Further reproduction prohibited without permission.

Figure 1-18. Internal waves detected north of the Gotoh Islands of Japan.

Reproduced with permission of the copyright owner. Further reproduction prohibited without permission.

reveals, yet it is their surface expression that is sensed by the SAR. The surface expression of a front is called a surface front and is a sharp boundary zone between adjacent water masses of dissimilar properties. They form where there are horizontal variations in energy generation and dissipation [30]. Uda [31] notes that fronts have been known to sailors and fishermen for centuries and have been named in many different tongues for the various properties they exhibit, such as shearing sounds, visible lines of floating debris and foam, and marked differences in color or visual texture on opposing sides of the front. Their scale and lifetime vary from a few meters and several hours to hundreds of kilometers and years. There are essentially six types of fronts, each distinguished by their mechanisms of creation [30]. They are:

1. Plume fronts
2. Shallow water and estuarine fronts
3. Current boundary fronts
4. Shelf-break fronts
5. Upwelling fronts
6. Ekman convergence fronts

Plume fronts form at the mouths of rivers where fresh water runoff overrides denser seawater. A density discontinuity occurs at the interface. The front reflects the equilibrium between seaward inertia of the fresh water and laterally directed buoyant forces. Wright, et.al. [32] give an unusually good description of plume frontogenesis. Flow deceleration and river effluent deconcentration result primarily from vertical mixing rather than lateral mixing. Vertical mixing causes the fresh water temperatures to approach the seawater temperature with

Reproduced with permission of the copyright owner. Further reproduction prohibited without permission.

increasing seaward flow. Surface temperatures of the plume front remain fairly constant for a distance from the channel of approximately four channel widths, then abruptly approach the seawater temperature within a finite band. The most intense vertical mixing takes place within the band. Over the distance from the channel to this band, the depth of the saltwater-freshwater interface decreases rapidly, causing currents to accelerate [32,33]. Seaward from the vertical mixing band, surface currents decelerate. This accounts for the distributary mouth bar crest being situated beneath the vertical mixing band. Beyond the band, periodic zones of lateral expansion and vertical mixing occur. The seaward decrease in lateral expansion rates produces parabolic plume boundaries defined as a result of water-mass convergence. This phenomena, coupled with the periodic vertical mixing zones, yields a periodic pattern of parabolic boundaries. The average geometry of the steady-state fresh water plume tends to be independent of absolute water discharge.

Plume fronts are modified by semi-diurnal as well as seasonal effects. Where there is a strong, reversing tidal flow, plume fronts will form only during ebb tide. During flood tide, Bowman [34] notes, the strong reversal of seawater overrides the plume and it disappears. Plume formation is also modified by seasonal trends in riverine discharge.

Plume fronts are detectable in SAR imagery, as shown in Figure 1-19. The presence of internal waves and surface current convergence at the boundary renders the front visible, although the exact electromagnetic scattering mechanism is yet conjecture. Several contributing factors have been suggested. The first factor is wind straining and

Reproduced with permission of the copyright owner. Further reproduction prohibited without permission.

Figure 1-19. SAR image of a plume front taken near Pensacola, Florida.

Reproduced with permission of the copyright owner. Further reproduction prohibited without permission.

wave steepening of Bragg scatterers which are modulated by underlying longer waves. Wind straining gives rise to a greater population of Bragg scatterers at the boundary, where water mass exchange is inhibited. Furthermore, when short waves are superimposed on longer ones, the shorter waves tend to become both shorter and steeper at the long wave crests [4]. The increased population of Bragg scatterers and tilting of the modulated short waves toward the radar antenna enhance detectability of waves at the boundary [20]. A second factor is fresh water convergence, particularly at the outer plume boundary, which is the surface expression of the saltwater-freshwater interface, but also at the periodic zones of vertical mixing within the plume. Surface current convergence produces higher frequency wave populations. A third factor is the air-sea temperature difference between zones of vertical mixing and those of lateral expansion. During periods of atmospheric instability, where the overlying air is cooler than the seawater, increased wind stress will occur in warm water zones within the plume, thereby increasing the capillary population. Finally, the convergence of flotsom at the boundary can increase scattering.

Shallow water and estuarine fronts are distinguished only by their location in the coastal environment, and like plume fronts, form as a result of fresh water runoff. They differ from plume fronts by the mechanism that creates the frontal interface. Consider the estuarine front. Buoyant fresh water in an estuary creates a stratified layer that is bounded, parallel to the axis of the estuary, by a surrounding turbulent layer. This is shown in Figures 1-20 and 1-21. Lateral shearing resulting from tidal motion is the dominant mechanism in these fronts [34]. During ebb tide, a mass deficit is created offshore which

Reproduced with permission of the copyright owner. Further reproduction prohibited without permission.

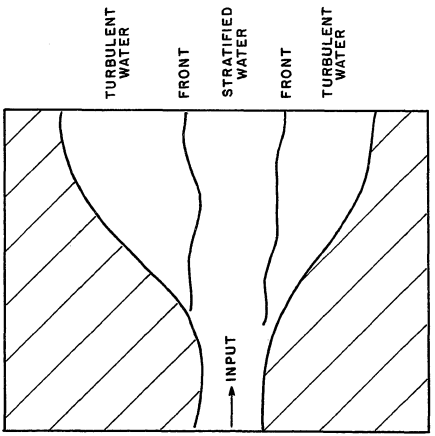

Figure 1-20. Estuarine front, plan view.

Reproduced with permission of the copyright owner. Further reproduction prohibited without permission.

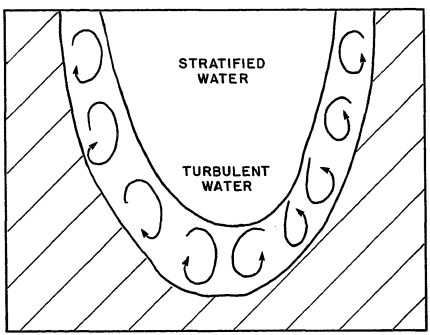

Figure 1-21. Estuarine front, cross section.

Reproduced with permission of the copyright owner. Further reproduction prohibited without permission.

causes higher salinity (denser) estuarine water to flow out of the estuary, in turn causing turbulent bottom stirring and lateral shearing between the stratified water and the turbulent, higher salinity water. Just as for plume fronts, flood tide tends to dissipate estuarine fronts by overrunning the stratified layer or advecting the front away from its source.

The phenomenon just described has been observed in real aperture radar (RAR) imagery by DeLoor [35] in the vicinity of the Rhine River. Lateral shearing produces a locally confused sea state along the frontal boundary which is rich in short waves. The increased population of Bragg scatterers and short wave tilting account for the visibility of the front in radar imagery. Estuarine frontal zones are known for the vast amounts of suspended particulates found in the turbid regions, including sediments, phytoplankton and pollutants. The concentration of particulates contrast the frontal boundary in photographic imagery (Figure 1-22) and can be expected to increase the microwave scattering cross section when the circulated particulates encounter the surface.

Plume fronts, shallow water and estuarine fronts show the pattern of sediment, pollutant and biological material transport in the coastal environment, and this is the primary value in their study. Sediment transport is particularly important in navigable waterways which must often be dredged. Damage done to the coastal environment by pollutants carried down river into estuaries is often the source of lawsuits. One must be able to determine the paths of transported pollutants to substantiate damage claims. The concentration of biological material is a key factor in fish populations in the coastal regions. This influences

Reproduced with permission of the copyright owner. Further reproduction prohibited without permission.

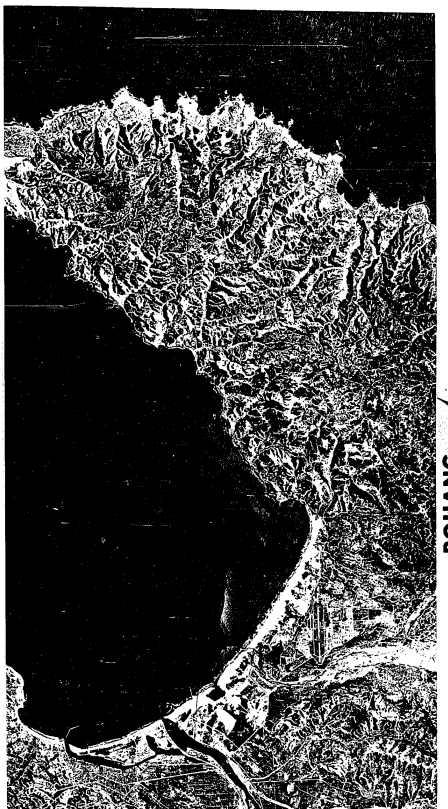

Figure 1-22. Aerial photograph of a shallow water front near Pohang, Korea. Suspended particulates contrast the frontal boundary.

Reproduced with permission of the copyright owner. Further reproduction prohibited without permission.

fishing, both by man and other animals.

Current boundary fronts occur due to convergence or pronounced lateral shear at the interface between large scale currents such as the Kuroshio,Oyashio or the Gulf Stream and slope shelf water. These currents transport large volumes of warm tropical water poleward to offset the polar energy deficit. Their frontal boundaries therefore exhibit a pronounced thermal gradient, too. Frontal variability is a function of seasonal flow changes, tidal oscillations and bathymetry. The volume of warm water carried by major currents and their flow velocities vary seasonally, thereby moving frontal boundaries. Tidal oscillations impact frontal location semi-diurnally in coastal regions. Bathymetry, such as the Charleston Rise on the eastern U.S., can have a pronounced impact on frontal location [36]. Channeling of a major current induced by bathymetry in a shallow coastal region will alter current velocities and thereby change the surface expression of a front.

The presence of current boundary fronts in radar imagery is well documented in the literature [18,36,37,38,39,40] and some effort has been made at identifying factors contributing to their visibility in the imagery. Moskowitz [39] states that two adjacent water masses moving in opposing directions or in the same direction at different speeds form an SAR detectable boundary due to steepening of short waves at the interface. Weissman's studies [38] implied that the backscattered radar cross section is proportional to the surface stress which is a function of the local wind, the surface current, the air and sea temperatures. He sited Parsons [41] to further substantiate the importance of air-sea temperature difference for current front detection. Hayes [36] attributes tonal and textural differences near the fronts

Reproduced with permission of the copyright owner. Further reproduction prohibited without permission.

to thermally induced effects of wind stress on surface roughness.

In contrast to large scale current boundary fronts that exhibit distinct thermal gradients, small scale fronts resulting from the convergence of water flow past headlands, promontories, islands, etc. exist and are seen in radar imagery. They are often referred to as headland fronts [42]. They are periodic with respect to their times of expression, based on tidal oscillations in the shallow headland regions. Bathymetry determines the velocities of tidal flow and therefore the location and intensity of shear at the frontal boundary. Shemdin, et. al. [43] have studied this phenomena in SEASAT SAR imagery over the Columbia River mouth in Oregon. Similar examples appear in the MARSEN X-band data near the island of Sylt. Figures 1-23 and 1-24 are examples from the Japanese data set, created at ebb tide where tidal currents as large as 3 knots exist.

The detection and analysis of current boundary fronts in SAR imagery has the potential to influence a number of oceanographic interests. These include navigation, coastal engineering, fisheries, antisubmarine warfare, hydrographic and marine geologic surveys, as well as the determination of air-sea temperature characteristics of importance to scientific studies of wind stress in the coastal environment. Wave-current interactions causing changes in wave direction, height and length affect engineering projects and navigation at river mouths. James [44] documents how wave-current interactions in the open ocean are related to large waves in high speed currents. Furthermore, currents refract ocean waves and influence wave energy propagation that may be important to coast line protection. Mapping of the Kuroshio or the Gulf Stream, for example, affects the fishing community, general

Reproduced with permission of the copyright owner. Further reproduction prohibited without permission.

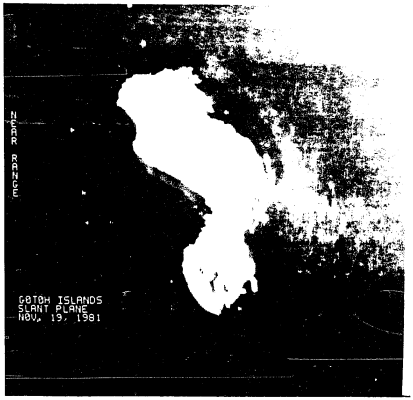

Figure 1-23. This headland front contours the island and extends in the direction of the tidal flow.

Reproduced with permission of the copyright owner. Further reproduction prohibited without permission.

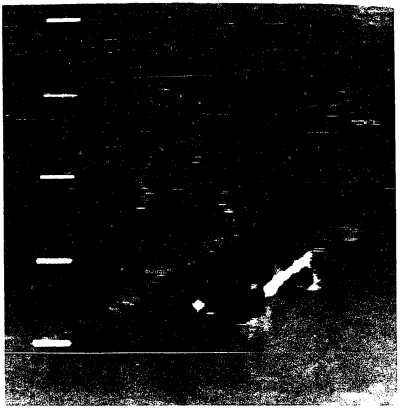

Figure 1-24. A headland front near one of the smaller Gotoh Islands of Japan. The "tail" of this front extends beyond this scene.

Reproduced with permission of the copyright owner. Further reproduction prohibited without permission.

navigation and military interests. The thermal gradients as well as nutrient concentrations, make the frontal boundaries areas of high marine productivity and, therefore, prime areas for commercial fishing. Japanese fishermen have long documented the large catches often made along the Kuroshio [31], and American whalers are responsible for the discovery of the Gulf Stream off the eastern U.S. coast [45]. Large scale currents can both serve and hinder coastal navigation. Sailing with the currents allows more timely travel and reduces fuel consumption. Avoiding stemming the currents is equally valuable. The case of delayed mail between Great Britain and the American colonies in the late 1760's is a classic example [45]. Massive shears at the boundaries can also stear ships off course or even destroy smaller craft. The thermal gradient at the Kuroshio and Gulf Stream boundaries presents a unique problem to acoustical tracking of submarines and is an issue of great military concern. The mapping of shallow water bathymetry has profound importance to coastal engineering and navigation. SAR offers the opportunity to monitor channels and sediment transport. DeLoor's discovery of sand dune patterns in the bottom of Rotterdam Harbor is one example of SAR's potential for detecting bathymetric features [35]. It is conceivable that quantitative measures related to wind stress as a function of air-sea temperature difference can be extracted from SAR imagery. This applies to a broad range of coastal features, of which current boundary fronts are one example. More will be said of this later in the chapter.

Shelf-break fronts are retrograde (anti-parallel to the shelf slope) fronts that usually straddle the continental shelf breaks. These fronts represent the interface between cold, fresh, along-shore

Reproduced with permission of the copyright owner. Further reproduction prohibited without permission.

transported shelf water and warmer, higher salinity continental slope water. Temperature and salinity gradients tend to have compensating effects on density and thereby minimize density contrast at the front. Shelf-break fronts are quite sensitive to seasonal characteristics. The characteristically cold along-shore water interfacing with warmer continental slope water indicates a winter scenario. The increasing solar radiation and more constant weather patterns of spring permit the formation of a seasonal thermocline, thereby creating a subsurface front. The thermocline dominates the frontal process in spite of increased fresh water runoff which enhances the salinity front.

Shelf-break fronts are subjected to variations induced by wind forcing, warm core eddies and calving. Large scale Ekman transport as well as small scale wind patterns are the source of wind forced variations. Warm core eddies are bodies of warm water that break off from large scale warm currents such as the Gulf Stream and impinge on shelf-break fronts. Calving is the process where lens-shaped parcels of shelf water propagate through the frontal interface below the surface [46]. Although important to frontal variation, their subsurface expression is difficult to detect.

Upwelling fronts are also found along the continental shelf region. In contrast to shelf-break fronts, upwelling fronts are prograde (aligned parallel to the continental shelf slope). They are also characterized by a marked temperature gradient, but the mechanism and scale of frontogenesis differs from that of shelf-break fronts. Upwelling fronts are caused by water mass deficits resulting from Ekman transport, as stated by Moores, et al. [46]. The western coast of the U.S. is an example. Prevailing surface winds are alongshore, southward throughout

Reproduced with permission of the copyright owner. Further reproduction prohibited without permission.

the spring and summer due to Pacific high pressure and the Arizona heat low (see Fig. 1-25 and 1-26). These winds induce an offshore Ekman transport. The nearshore mass deficit from the transport is replenished with cold bottom water. A tilt of the temperature/density surface between the upwelled and transported water forms the frontal interface. When surface winds are strong in a southward direction, the tilt can cause the emergence of a surface front. Wind patterns favoring upwelling intensify throughout the summer as the Pacific subtropical high moves poleward.

Although shelf-break and upwelling fronts exhibit characteristics that should lend themselves to SAR imaging, I have found no examples or discussions of them in the radar literature. Two properties should make them visible. The first is the temperature gradient across the fronts. Depending on the atmospheric conditions at the air-sea interface, there is likely to be increased wind stress on one side of the surface front. This same scenario is attributed to detection of the Gulf Stream [36], cold water rings [47] and warm water rings [48]. A second property is the concentration of particulate matter in waters adjacent to the surface front. This should be especially true in upwelling fronts. Surface slicks and flotsom at the front should contribute markedly to the radar signature. The large scale of these fronts, as compared to plume or shallow water fronts, may impede their definition, or classification, in aircraft SAR imagery, but should be easily distinguishable in SEASAT SAR imagery.

Large scale prograde and retrograde shelf edge fronts are of prime interest to the military and to marine productivity. Prograde and retrograde fronts create a thermal acoustic barrier that extends from

Reproduced with permission of the copyright owner. Further reproduction prohibited without permission.

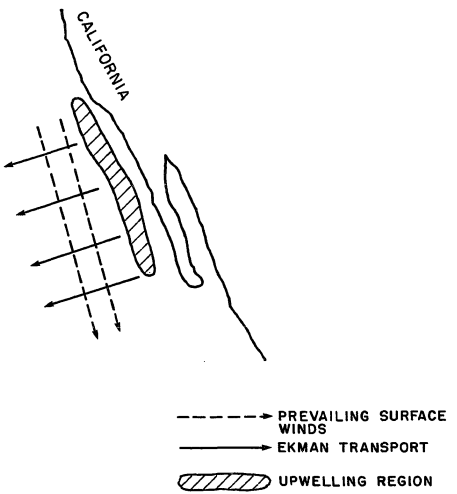

Figure 1-25. The creation of an upwelling front.

Reproduced with permission of the copyright owner. Further reproduction prohibited without permission.

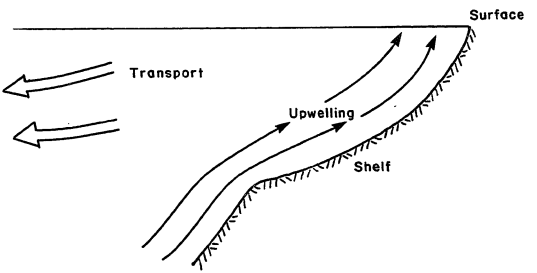

Figure 1-26. Cross section of upwelling front formation.

Reproduced with permission of the copyright owner. Further reproduction prohibited without permission.

the shelf to the surface, or near surface. Furthermore, processes such as calving, warm water impingement and wind forcing of shelf-break fronts continually alter their acoustic structure. The ability of submarines to cruise undetected along continental shelves is a sensitive national security matter. Of all the fronts discussed in this chapter, upwelling fronts have the greatest impact on marine productivity. Upwelled water comes from depths of 100 to 200 meters, raising significant volumes of nutrients into the Euphotic zone. Many ecosystems and some local economies rely on upwelling for survival. When it ceases, surface water temperatures rise due to solar heating, and biological activity decreases. In Peru, for example, the cessation of upwelling allows the warm El Nino current to spread southward. The current shift coupled with higher surface water temperatures causes instability in the overlying atmosphere, accompanied by excessive rain causing floods and erosion. There is an increased odor from decomposing organic matter, and the hydrogen sulfide liberated from organic decomposition blackens paint on ships [28].

Ekman convergence fronts are the sixth and final class of fronts. They are global scale fronts occurring in the Horse latitudes due to the convergence of water masses from Ekman transport in the Pacific and Atlantic. Unlike the fronts previously discussed, these have faint surface definitions. Because of their distance from inhabited coastal regions and their global and seasonally predictable nature, they have not been the center of frontal research. Neither have they been imaged by SAR. It is interesting to note, in passing, that Ekman convergence fronts are the hydrologic analogy of the intertropical convergence zone of meteorology which brews tropical storms and hurricanes.

Reproduced with permission of the copyright owner. Further reproduction prohibited without permission.

Although there are six subclasses of fronts, five of which have been or can be detected in radar imagery, only two subclasses of fronts are covered in this study. They are:

1. Open water fronts,
2. Headland fronts.

Apart from their mechanisms of formation, these two subclasses differ only in the adjacency of land when seen in SAR imagery. Subtle differences in image expression of shallow water fronts and shelf-break fronts, for example, can easily be obscured by underlying surface waves and wind effects, making visual classification difficult, if not impossible. Furthermore, there is presently no expertise for making precise visual discriminations of sea features in SAR imagery. It is hoped that quantitative analysis of subclasses will aid in this task. The approach is to start with obvious, albeit crude, image class descriptions and to refine them with experience. Plume fronts are not found in the Japanese data and are not included as an image subclass, although they are distinctive enough to comprise a third subclass, were they present.

1.5 Summary

The four basic classes of SAR image patterns chosen for this study have been broken down into subclasses and examined. These subclasses have been chosen as a function of their documented occurrence in radar imagery, or by their potential for detection. The hydrologic and meteorologic factors that create and modify the seas, which, in turn, result in radar backscatter sensed by the radar, have been outlined. The significance of the sea features that produce the radar pattern

Reproduced with permission of the copyright owner. Further reproduction prohibited without permission.

subclasses have been presented to substantiate the study's usefulness to mankind.

Reproduced with permission of the copyright owner. Further reproduction prohibited without permission.

REFERENCES

1. Crombie, D.C., "Doppler Spectrum of the Sea Echo at 13/56 Mc/s," Nature.,Vol. 175, (1955), pp. 681-682.

2. Kraus, E.B., Atmosphere-Ocean Interaction. London:Oxford Press, 1972, pp. 116-127.

3. Phillips, O.M., "On the Generation of Waves by Turbulent Wind," J. Fluid Mech., Vol. 2 (1957), pp. 417-445.

4. Longuet-Higgins, M.S. and R. W. Stewart, "Changes in the Form of Short Gravity Waves on Long Waves and Tidal Currents," J. Fluid Mech., Vol. 8 (1960), pp. 565-583.

5. Longuet-Higgins, M.S. and R. W. Stewart, "The Changes in Amplitude of Short Gravity Waves on Steady Non-Uniform Currents," J. Fluid Mech., Vol. 19 (1961), pp. 529-549.

6. Longuet-Higgins, M.S., "The Instabilities of Gravity Waves of Finite Amplitude in Deep Water, Part I, Superharmonics," Proc. Roy. Soc., A360 (1978), pp. 471-488.

7. Plant, W. J., "Microwave Radars Used as Two-Scale Wave Probes," Personal communication.

8. Brown, W.M. and L. J. Porcello, "An Introduction to Synthetic Aperture Radar," IEEE Spectrum , (Sept. 1969), pp. 52-62.

9. Swift, C.T. and L. R. Wilson, "Synthetic Aperture Radar Imaging of Moving Ocean Waves," IEEE Trans. Antennas And Prop., Vol. AP-27, No. 6 (Nov. 1979), pp. 725-729.

10. Alpers, W.R. and C.L. Rufenach, "The Effect of Orbital Motions on Synthetic Aperature Radar Imagery of Ocean Waves," IEEE Trans. Antennas And Prop., Vol. AP-27, No. 5 (Sept. 1979), pp. 685-690.

11. Alpers, W.R. and L. Jones, "The Modulation of the Radar Backscattering Cross Section by Long Ocean Waves," in Proc. 12 Intl. Symp. Remote Sensing Environ., Manilla, Phillipines, (April 20-26, 1978), pp. 1597-1608.

12. Roll, H.U.,Physics Of The Marine Atmosphere. New York: Academic Press, 1965, pp. 115-117.

13. Woodcock, A.H., "Surface Cooling and Streaming in Shallow Fresh and Salt Waters," J. Marine Research , Vol. 4 (1941), pp. 153-161.

Reproduced with permission of the copyright owner. Further reproduction prohibited without permission.

14. Woodcock, A.H., "A Theory of Surface Water Motion Deduced from the Windinduced Motion of the Physalia," J. Marine Research , Vol. 5, No. 3 (1944).

15. Miles, J.W., "On the Generation of Surface Waves by Shear Flow: Part 1-Part 4," J. Fluid Mech., Part 1: Vol. 3 (1957), pp. 185-204; Part 2: (1959), pp. 583-598; Part 4: Vol. 13 (1962), pp. 433-448.

16. Welander, P., "On the Generation of Wind Streaks on the Sea Surface by Action of Surface Film," Tellus , Vol. 15, No. 1 (1963), pp. 67-71.

17. Stommel, H., "Streaks on Natural Water Surfaces," Geophys. Research Papers (U.S.) , No. 19, (1952), pp. 145-154.

18. Fu. L.L. and B. Holt, SEASAT Views Oceans And Sea Ice With Synthetic Aperture Radar , JPL Pub. 81-120. Pasadena, CA: Jet Propulsion Lab., 1982

19. Shuchman, R.A., E.S. Kasischke, and A. Klooster, Synthetic Aperture Radar Ocean Wave Studies , ERIM Final Report, NOAA Contract No. 7-35328, Ann Arbor, MI: ERIM, Sept. 1978.

20. Wright, J.W., "Detection of Ocean Waves by Microwave Radar: The Modulation of Short Gravity-Capillary Waves," Boundary-Layer Metereology , Vol. 13 (1978), pp. 87-105.

21. Gargett, A.E. and B.A. Hughes, "On the Interaction of Surface and Internal Waves," J. Fluid Mech., Vol. 52 (1972), pp. 179-191.

22. Hughes, B.A., "On the Interaction of Surface and Internal Gravity Waves: Uniformly Valid Solution by Extended Stationary Phase," J. Fluid Mech., Vol. 74 (1976), pp. 667-683.

23. De Loor, G.P. and H.W. Brunsveld Van Hulten, "Microwave Measurements Over the North Sea," Boundary-Layer Meteorology , Vol. 13 (1978), pp. 119-131.

24. Gower, J.F.R. and B.A. Hughes, "Radar and Ship Observations of Coastal Sea Surface Roughness Patterns in the Gulf of Georgia," in Proc. 13 Intl. Symp. Remote Sensing Environ., Vol. 1, Ann Arbor, MI: ERIM (April 23-27, 1979), pp. 103-105.

25. Hsu, S.A., " Dynamic Roughness Equation and Its Application to Wind Stress Determination of the Air-Sea Interface," J. Phys. Ocean., Vol. 4 (1974), pp. 116-120.

26. Amorocho, J. and J. DeVries, "Wind Stress Over Water," J. Geo-Phys. Research , Vol. 85, C-1 (Jan. 1980), pp. 433-442.

27. Burk, S.D., "Temperature and Humidity Effects on Refractive Index Fluctuations in Upper Regions of the Convective Boundary Layer," J. Applied Meteor., Vol. 20 (June 1981), pp. 717-721.

Reproduced with permission of the copyright owner. Further reproduction prohibited without permission.

28. Neumann, G. and W.J. Pierson, Jr., Principles of Physical Oceanography , Englewood Cliffs, N.J.: Prentice Hall, 1966, pp. 381-383.

29. LaFond, E.C. and K.G. LaFond, "Sea Surface Slicks," Tech. Report, NAVSHIPS. contract SR 1040301, task 0596, pp. 75-103.

30. "Proceedings of the Workshop," in Ocean Fronts In Coastal Processes.,Workshop Proceedings, Stony Brook, N.Y.: Marine Sciences Research Center (May 1977), pp. 2-5.

31. Uda, M., "Researches on 'Siome' or Current Rip in Seas and Oceans," Geophy. Mag., No. 11 (1938), pp. 307-373.

32. Wright, L.D., J.M. Coleman and J.N. Suhayda, "Periodicities in Interfacial Mixing," in Coastal Studies Bulletin, No. 7, Tech. Report No. 133, Coastal Studies Institute, Baton Rouge, LA (Jan. 1973), pp. 127-135.

33. Kashiwamura, M. and S. Yoshida, "Transient Accelerations of Surface Flow at a River Mouth," Coastal Engineering In Japan , Vol. 14 (1971), pp. 135-142.

34. Bowman, M.J. and R.L. Iverson, "Estuarine and Plume Fronts," in Ocean Fronts In Coastal Processes , Workshop Proceedings, Stony Brook, N.Y.: Marine Sciences Research Center (May 1977), pp. 87-104.

35. DeLoor, G.P., "The Observation of Tidal Patterns, Currents and Bathymetry with SLAR Imagery of the Sea," IEEE J. Oceanic Engr., Vol. OE-6, No. 4 (Oct. 1981), pp. 124-129.

36. Hayes, R.M., "Detection of the Gulf Stream," in Spaceborne Synthetic Aperture Radar For Oceanography , Baltimore, MD: Johns Hopkins Univ. Press, 1981, pp. 146-160.

37. Ross, D.B., "The Wind Speed Dependency of Ocean Microwave Backscatter," in Spaceborne Synthetic Aperture Radar For Oceanography , Baltimore, MD.: Johns Hopkins Univ. Press, 1981, pp. 75-86.

38. Weissman, D.E., "Modulation of Sea Surface Radar Cross Section by Surface Stress: Wind Speed and Temperature Effects Across the Gulf Stream," J. Geophys. Research , Vol. 85, C-9 (Sept. 1980), pp. 5032-5042.

39. Moskowitz, L.J., "The Feasibility of Ocean Current Mapping via Synthetic Aperture Radar Methods," Proc. Amer. Soc. Photogr., Part II (Oct. 2-5, 1973), pp. 760-771.

40. Hayes, J.G. and R.A. Shuchman, "SEASAT SAR Ocean Surface Current and Shallow Water Wave Refraction," Proc. Cospar/Scor/Iucrum Symp. Ocean. From Space , (1981).

Reproduced with permission of the copyright owner. Further reproduction prohibited without permission.

41. Parsons, C.L., "An Observational Study of the Variations in the Vicinity of the Gulf Stream," in Skylab S-193 Radar Altimiter Experiment Analysis And Results , ed. G.S. Brown, NASA, Washington, D.C., 1971.

42. Pringree, R.D., M.J. Bowman and W.E. Esaias, "Headland Fronts," in Ocean Fronts In Coastal Processes , Workshop Proceedings, Stony Brook, N.Y.: Marine Sciences Research Center (May 1977), pp. 35-39.

43. Shemdin, O.H., A. Jain, S.V. Hsiao, L.W. Gotto, "Inlet Current Measured with SEASAT-1 Synthetic Aperture Radar," Shore And Beach , Vol. 48 (1980), pp. 35-39.

44. James R.W., "Dangerous Waves Along the North Wall of the Gulf Stream," Mariners Weather Log., Vol. 18 (1974), pp. 363-366.

45. Richardson, P.L., "Benjamin Franklin and Timothy Folger's First Printed Chart of the Gulf Stream," Science , Vol. 207, No. 4431 (1980), pp. 643-645.

46. Moores, C.N.K., C.N. Flagg and W.C. Boicourt, "Prograde and Retrograde Fronts," in Ocean Fronts In Coastal Processes , Workshop Proceedings. Stony Brook, N.Y.: Marine Sciences Research Center (May 1977), pp. 43-58.

47. Cheney, R.E., "A Search for Cold Water Rings," in Spaceborne Synthetic Aperture Radar For Oceanography , Baltimore, MD.: Johns Hopkins Univ. Press, 1981, pp. 161-170.

48. Lichy, D.E., M.G. Mattie and L.J. Mancini, "Tracking of a Warm Water Ring," in Spaceborne Synthetic Aperture Radar For Oceanography , Baltimore, MD.: Johns Hoplins Univ. Press, 1981, pp. 171-182.

Reproduced with permission of the copyright owner. Further reproduction prohibited without permission.

CHAPTER 2

THE STATE OF THE ART IN DIGITAL EXPLOITATION OF SAR IMAGERY

Digital exploitation of SAR imagery in unclassified research covers a fairly wide range of activities, but is severely limited in scope. The relative abundance of optical SAR systems, limited availability of affordable computer resources, and a lack of digital exploitation expertise likely account for the limited content in these activities. Five principal activity areas are presented in this chapter. They are:

1. Digital correlation
2. Coherent speckle reduction
3. Ocean wave spectra (including geometric conversion)
4. Texture analysis
5. Image simulation

2.1 Digital Correlation

Digital correlation is not exploitation in the sense that the detected image is processed, but digital techniques are utilized in creating SAR imagery. This allows greater image creation flexibility which is germane to exploitation activities such as speckle reduction and texture analysis. Identification of correlation alternatives is therefore a worthwhile endeavor for certain analysis.

Correlation is the process of creating an error-free detected

Reproduced with permission of the copyright owner. Further reproduction prohibited without permission.

image from recorded phase information. The acquisition of the phase data is described by SAR imaging theory. A detailed discussion of SAR theory is beyond the scope of this chapter, although a brief mathematical development is included in Appendix 1 for completeness. Brown [1,2] also offers a good introduction.

A fundamental insight of SAR theory is that fine azimuth resolution is achieved by synthesizing a large aperture, recording and processing the Doppler history over the synthesized aperture. Image processing requires the assignment of intensities at locations in the image plane determined by both the signal propagation delay (range dimension) and the zero Doppler point (azimuth dimension) of each scatterer. The processor is conceptualized as a two-dimensional filter matched to the signal generated and recorded by each point scatterer [3]. The image is the result of a two-dimensional cross-correlation of the recorded return signal and a reference function. The processor is therefore called a correlator.

Correlation is traditionally done on an optical bench [1]. The scattered radar signal is coherently mixed to video frequencies and used to modulate the intensity of a CRT trace. Each point on the trace represents a different range return. The azimuth phase history is recorded by transporting film past the CRT at a rate proportional to the SAR velocity (Figure 2-1). The phase history film is actually a hologram. Image generation results from wavefront reconstruction using coherent light and optics. The optics perform integration via the spatial Fourier transform and additionally provide the reference function [4]. The input phase history film and the output image film are synchronously translated through the processor, thereby

Reproduced with permission of the copyright owner. Further reproduction prohibited without permission.

Reproduced with permission of the copyright owner. Further reproduction prohibited without permission.

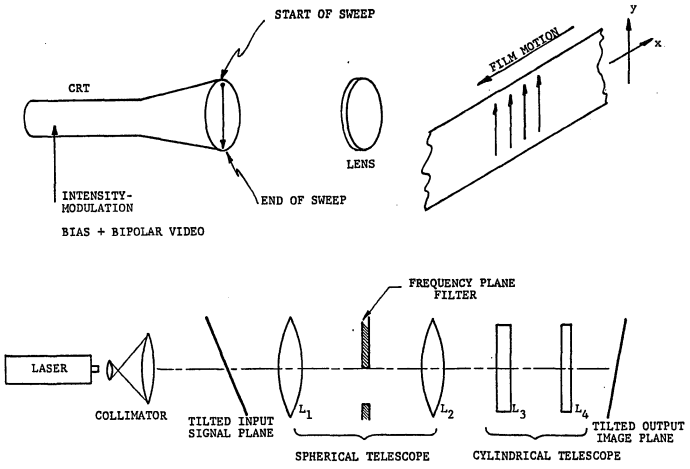

Figure 2-1. a) Phase history film recording. b) The coherent optical correlator. Taken from Ausherman [3].

implementing cross-correlation. The developed output film is a slant-range representation of coherent scattering in the scene.

Digital correlation is analagous to optical correlation, yet flexible in its implementation. A notable advantage of digital correlation is the elimination of the optical bench, thereby opening the door to full or partial airborne correlation. Digital processing is still composed of two distinct data storage and correlation stages; however, different systems implement them in manners unique to their application. Kirk [5] provides a thorough review of correlation implementations. Inherent in his discussions is airborne collection and correlation performance using dedicated hardware to reduce space and processing time. He also identifies imaging modes aside from the conventional stripmap format which may be easily accommodated through digital collection and correlation. These include the spotlight mode, in which one predesignated coordinate is imaged during antenna syntheses; and the scan mode in which many spotlighted areas are mosaiced forming a scan path virtually unconstrained by the aircraft path. Ausherman [3,6] contrasts optical and digital SAR processing as implemented at the Environmental Research Institute of Michigan (ERIM). The ERIM approach is to store the phase data on high density tape and correlate it with specialized programs in a general purpose computer. Digital processing ranges from aircraft motion compensation and two-dimensional Fourier transforms to polar formatting and higher order focusing in spotlight and scan mode imagery. Wu [7,8,9] discusses the SEASAT digital processing system. Additional processing requirements for satellite SAR data include digital downlinking to the ground for storage and geometric correction due to earth and microwave

Reproduced with permission of the copyright owner. Further reproduction prohibited without permission.

wavefront curvature. Van de Lindt [10] also provides a rather comprehensive discussion of spaceborne SAR processing.

Digital correlation benefits SAR image exploitation in a fundamental way. It gives the image analyst access to the raw phase history, as well as the detected image, through the computer. This expands the scope of exploitation activities tremendously. Phase perturbations of any mathematical order may be introduced to refocus imagery, an activity prohibited by optical correlation. Visual image quality may be improved through speckle reduction techniques such as frequency and angular diversity without the use of an optical bench. Digital pattern analysis may also be done in the phase history domain, as well as in the spatial domain image. Unfortunately, almost all higher resolution unclassified SAR data is optically correlated, thereby restricting exploitation to the detected image.

2.2 Coherent Speckle Reduction

Speckle gives SAR imagery its characteristic grainy appearance and results from interference of diffusely scattered coherent radiation recorded by the SAR. The condition for diffuse scattering is that surface variations of an illuminated area be large relative to the radar wavelength. X-band radiation, for example, has a wavelength of approximately 3 cm, which assures that many of the natural surfaces of our environment satisfy this condition. The phase of coherent radiation returned to the SAR antenna from these rough surfaces varies significantly over the range of $-\pi$ to π. Summation of the complex phase amplitudes from the SAR resolution cell determines the image intensity at a point. Each resolution cell is an independent

Reproduced with permission of the copyright owner. Further reproduction prohibited without permission.

summation of randomly distributed complex phase amplitudes, thereby giving SAR imagery a noisy appearance.

Some statistical aspects of speckle are worth noting, especially as they apply to SAR ocean imagery. Goodman [11] models speckle as a random walk problem. Each scatterer of the illuminated surface contributes a complex amplitude phasor. The amplitude and phase of any phasor is independent of the amplitude and phase of other phasors. The phase of the scattered signals is equally likely to lie anywhere in the range $(-\pi, \pi)$. Provided that the number of scatterers is large, the real and imaginary parts of the scattered signal are independent, zero mean, identically distributed Gaussian random variables, and the intensity has a probability density function of the form,

$$p(I) = \begin{cases} (1/\bar{I}) \exp(-I/\bar{I}), & I \geq 0 \\ 0, & \text{elsewhere} \end{cases} \qquad (2\text{-}1)$$

where $\bar{I}$ is the mean intensity. Since the standard deviation equals the mean in an exponential distribution, the contrast of a polarized speckle pattern, C, is

$$\sigma_I / \bar{I} \qquad (2\text{-}2)$$

where σ_I is the pattern standard deviation. This ratio is always unity. Any surface which produces phase shifts of 2π radians or more adequately defines the speckle statistics. No change will occur in these statistics for rougher (in radar wavelength terms) surfaces.

A characteristic of SAR ocean imagery which conceivably could alter speckle statistics is scene partial coherence. The term "partial coherence" describes the event of scatterers moving in a nondeterministic fashion during the integration time of the SAR. For integration times

Reproduced with permission of the copyright owner. Further reproduction prohibited without permission.

longer than approximately 100 ms (for X-band) Raney [22] notes that scene coherence time variations will be mapped as brightness variations. This is in contrast to the desire of SAR imagery to reflect surface roughness. When the SAR processor is adjusted to match the scene coherence, Raney [13] notes that the speckle variance decreases causing severely attenuated ocean waves to become more apparent. Otherwise, image detail fades into the speckle background. While partial coherence can affect the visibility of ocean waves, Raney [13] explicitly states that the variance-to-mean-squared ratio for a SAR scene, or C^2 from equation (2-2)is not a function of coherence time. He further states [14] that speckle statistics remain unchanged for a variety of minor focus alterations. These observations attest to the robustness of the first order speckle statistics despite SAR ocean imaging peculiarities.

Speckle reduction in SAR imagery has received a small variety of attention in the literature. Most authors treat the SAR case as an example of the more general problem of multiplicative noise reduction. Porcello, et. al. [15], Guenther [16] and Dicaprio, et. al. [17] represent the non-coherent integration approach to speckle suppression. Frost, et. al. [18] and Lee [19] espouse the adaptive filtering technique.

Non-coherent integration is best presented by Porcello, et.al. [15]. The technique is to sum N independent estimates of the backscatter associated with each resolution cell. The sum has a probability density function

Reproduced with permission of the copyright owner. Further reproduction prohibited without permission.

$$p(I) = \begin{cases} \dfrac{1}{(\bar{I}/N)(N-1)!}\left(\dfrac{I}{\bar{I}/N}\right)^{N-1}\exp\left(\dfrac{-I}{\bar{I}/N}\right), I \geq 0 \\ 0 \qquad\qquad \text{,elsewhere} \end{cases} \tag{2-3}$$

and a reduced speckle contrast ratio

$$c = \sigma_{I/\bar{I}} = N^{1/2} \tag{2-4}$$

The simplest implementation of non-coherent integration is to sum geometrically registered passes of the same scene. This is uneconomical and dangerous in some military applications. Porcello introduces the idea of polarization, angular and frequency diversity which is based on the fact that, "...uncorrelated images result from signals whose spectra are nonoverlapping [15]." These uncorrelated images may then be summed, producing a reduced speckle image similar to that created by summing registered passes. Dual polarized SAR's generate uncorrelated images since diffuse scatterers depolarize the scattered radiation. Angular diversity is based on subdividing the azimuthal Doppler spectrum into N_D nonoverlapping intervals, generating N images from these intervals and incoherently summing them. This is done by operating the radar with a larger angular beamwidth. From Appendix 1, the azimuth resolution is

$$\rho_A = \frac{\lambda_o}{2\beta} \tag{2-5}$$

so increasing the beamwidth, β, by N_D corresponds to

$$\beta = N_D \frac{\lambda_o}{2\rho_A} \tag{2-6}$$

This results in a greater Doppler spectrum width,

Reproduced with permission of the copyright owner. Further reproduction prohibited without permission.

$$\Delta\nu' = N_D \left(\frac{V}{\rho_A}\right) \tag{2-7}$$

and a corresponding resolution degradation of

$$\rho_A = N_D(\rho_A)_{\text{coherent}} \tag{2-8}$$

Frequency diversity is based on subdividing the range sensing backscattered signal spectrum into N_R nonoverlapping intervals, generating an image from each and incoherently summing. Appendix 1 shows that the backscattered signal bandwidth is

$$W = \frac{c}{2\rho_R} \tag{2-9}$$

where c is the velocity of light and ρ_R is the range resolution. Subdividing the bandwidth into intervals of $c/2\rho_R$ implies a bandwidth increased by N_R so that

$$W = N_R \left(\frac{c}{2\rho_R}\right) \tag{2-10}$$

and the corresponding range resolution degradation is expressed as

$$\rho_R = N_R(\rho_R)_{\text{coherent}} \tag{2-11}$$

Combination of angular and frequency diversity is a partitioning of the two-dimensional complex phase history into $N_R N_D$ subintervals yielding speckle reduction at the expense of both azimuth and range resolution.

Reproduced with permission of the copyright owner. Further reproduction prohibited without permission.

The sacrifice of resolution through angular and frequency diversity is acceptable for most SAR ocean feature discrimination at single look resolution on the order of a few meters. The greatest restriction to image analysis is the requirement of an optical correlator to reprocess the phase history. Until digital correlation becomes available to digital image exploiters, non-coherent integration will largely be left to the discrimination of the data supplier. In the meantime, speckle reduction in detected imagery is of interest. Adaptive filtering addresses this problem. The adaptive filters of both Frost [18] and Lee [19] will be presented.

The adaptive Frost filter is based on a multiplicative noise model,

$$I(x,y) = [r(x,y).n(x,y)]*h(x,y) \qquad (2\text{-}12)$$

where

$I(x,y)$ = observed image

$r(x,y)$ = "ideal" image

$n(x,y)$ = speckle noise component

$h(x,y)$ = system impulse response

and "*" denotes convolution. Frost attempts to estimate $r(x,y)$ from $I(x,y)$ by deriving a minimum mean squared error (MMSE) filter based on local scene statistics. The impulse response of his filter is

$$M(x,y) = k\ \alpha\ \text{esp}\ \{-\alpha|(x,y)|\} \qquad (2\text{-}13)$$

where

k = normalizing constant over the local window

α = filter decay constant.

Frost estimates α from the local sample mean and variance.

Reproduced with permission of the copyright owner. Further reproduction prohibited without permission.

Specifically,

$$\alpha^2 \propto \sigma_I^2/\bar{I}^2 \tag{2-14}$$

where

σ_I^2 = local variance

$\bar{I}^2$ = local image mean squared

The "ideal" image is obtained from the observed image via the operation,

$$r(x,y) = I(x,y)*m(x,y) \tag{2-15}$$

where m(x,y) is adapted for each positioning of the local window.

Lee's adaptive filter is also based on a multiplicative noise model

$$I = rn \tag{2-16}$$

where the indices (x,y) have been dropped for notational convenience. Lee linearizes the relationship by expanding the model in a first order Taylor series about the means $(\bar{r},\bar{n})$,

$$I = \bar{n}r + \bar{r}(n-\bar{n}) \tag{2-17}$$

The filtering algorithm is developed from a MMSE argument yielding

$$\hat{r} = \bar{r} + k(I-\bar{n}\bar{r}) \tag{2-18}$$

where

$$k = \frac{\bar{n}\,\sigma_r^2}{\bar{r}^2\sigma_n^2+\bar{n}^2\sigma_r^2} \tag{2-19}$$

and

σ_r^2 = "ideal" image variance

σ_n^2 = speckle noise variance

Reproduced with permission of the copyright owner. Further reproduction prohibited without permission.

$\hat{r}$ = estimate of the "ideal" image

Upon implementation, Lee approximates σ_r^2 by

$$\sigma_r^2 = \frac{\sigma_I^2 + \bar{I}^2}{\sigma_n^2 + \bar{n}^2} - \bar{r}^2 \qquad (2\text{-}20)$$

where $\bar{r}^2$ is estimated as the local window mean squared, $\bar{I}^2$. Lee assumes n=1. For single look imagery (not non-coherently integrated), $\sigma_n^2 < 1$. In these cases, σ_n^2 is estimated from image histograms.

Both adaptive filters have the advantage of preserving image edge contrast. This is because the variance-to-mean-squared ratio in local edge windows is large, resulting in very slight attenuation by the filter. Lee [20] has refined his algorithm to smooth speckle near edges by computing local statistics from a reduced set of pixels, depending on the orientation of the edge. Edge preservation is especially important in detecting and mapping the location of linear SAR features such as fronts, significant wave trains and land/water boundaries.

Marr and Hildreth [21,22] have suggested a combination band-pass filter and edge detecting algorithm which is espoused to model human visual processing and the retina. In his well known 1980 paper, Marr [21] states that the optimal smoothing filter is one that satisfies two conflicting requirements.

1. The filter's spectrum should be smooth and roughly band-limited in the frequency domain, thereby reducing the range of gray levels over which intensity changes take place. In other words, the frequency variance

Reproduced with permission of the copyright owner. Further reproduction prohibited without permission.

$\Delta\omega$, should be small.

2. Filtering should be spatially localized. The sources of intensity change in imagery define their spatial scales of effect. The scale for mountain shadows in a SAR image, for example, is different than that of Bragg scattering along an ocean front. Stated another way, the spatial variance, Δx, should be small.

The one distribution function that optimizes these requirements is the Gaussian, which expressed in the two-dimensional Fourier domain, is

$$G(r) = (1/2\ \pi\ \sigma^2)\ \exp\ (-r^2/2\sigma^2) \quad . \tag{2-21}$$

Edges correspond to zero-crossings in the second derivative of intensity. To find the edges in a Gaussian filtered image, one implements the operation,

$$f(x,y) = D^2[G(r) * I(x,y)] \tag{2-22}$$

where

D^2 = second derivative,

$*$ = convolution

$f(x,y)$ = filtered image .

By the derivative rule for convolution,

$$f(x,y) = D^2G(r) * I(x,y) \quad . \tag{2-23}$$

The Laplacian gives an orientation independent second derivative, which in two dimensions, is

Reproduced with permission of the copyright owner. Further reproduction prohibited without permission.

$$\nabla^2 G(r) = \frac{-1}{\pi\sigma^4}\left[1 - \frac{r^2}{2\sigma^2}\right] \exp\left(\frac{-r^2}{2\sigma^2}\right) \quad . \qquad (2\text{-}24)$$

Marr [21] has shown that this relationship is identical, within a scaling constant, to a difference of Gaussian filter. The significance of this relationship is that the retinal ganglion cells of the eye yield a sensitivity distribution which is described mathematically as the difference of two concentric Gaussian distributions. Therefore, equation (2-23) models human visual data processing. Filtering and edge detection are performed simultaneously by equations (2-22) and (2-24) upon convolving the second derivative filter and the image. The input parameters required are a window dimension, r_{max}, and a variance, σ^2.

Mastin [23] conducted an experiment to qualitatively evaluate the utility of five speckle reduction filters on edge detection. These were:

1. 5 by 5 sliding window average filter,
2. 5 by 5 sliding window median filter,
3. 5 by 5 adaptive Frost filter
4. 5 by 5 adaptive Lee filter,
5. The Marr filter.

Edge detection was used as an evaluation criteria. Most edge detectors are based on gray level differencing, and are therefore quite sensitive to speckle. The test image was a highly speckled scene of an internal wave pattern near Pensacola, Florida. It was collected by a Goodyear AN/UPD-4 SAR system mounted on an F-4 Phantom jet. The data

Reproduced with permission of the copyright owner. Further reproduction prohibited without permission.

were optically recorded and correlated, then digitized by an Optronics drum scanner sampling at 1000 points/inch with a dynamic range of 256 gray levels. The resulting spatial resolution was approximately 3 m/pixel. The entire 512 by 512 pixel image was processed by each filter, then processed by a 3 by 3 pixel Robert's gradient.

The original test image and its gradient, as well as the filtered images and their gradients, is shown in Figures 2-2 through 2-7. The processing parameters in Figure 2-7a were chosen to smooth the speckle, but not to mark edges as zero crossings [23].

One important conclusion can be drawn about speckle reduction filters for SAR ocean imagery. Simple and time efficient filters such as the average or median work as well, and in the case of the Frost filter, better than more theoretically and computationally complex filters. This is true from the standpoint of both visual quality and simple gradient edge detection. To emphasize the computational efficiency consideration, it should be noted that both the Lee and Frost filters required over an hour each to process on a Perkin-Elmer 8/32 minicomputer, while the average and median filters each required fifteen minutes or less.

For the time involved in the Lee, Frost and Marr filterings, Marr filtering provides the most favorable result and is the most easily adjusted in a predictable manner. The nonadaptive nature of the filter has definite advantage computationally over Lee and Frost filtering. Secondly, little knowledge of scene statistics is needed to set filter parameters. Only one parameter aside from the processing window size is needed, and reasonable values of σ^2 are easily chosen by considering equation (2-24). The third advantage is the dual role

Reproduced with permission of the copyright owner. Further reproduction prohibited without permission.

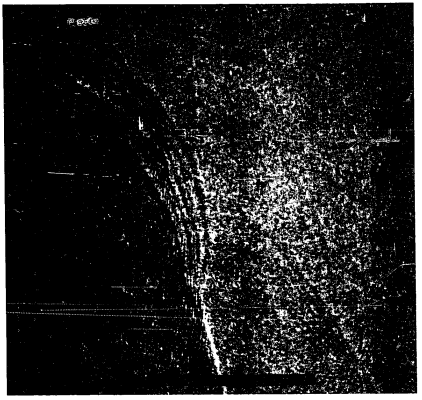

Figure 2-2a. Original speckle image of internal waves near Pensacola, Florida.

Reproduced with permission of the copyright owner. Further reproduction prohibited without permission.

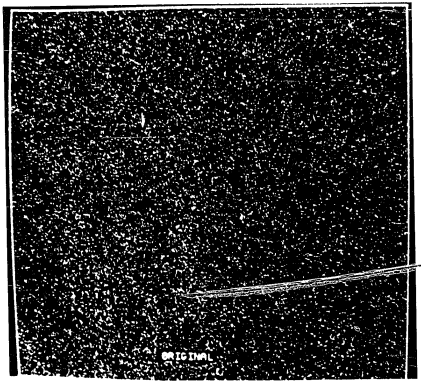

Figure 2-2b. Result of implementing a Robert's gradient edge detector on the original speckle image.

Reproduced with permission of the copyright owner. Further reproduction prohibited without permission.

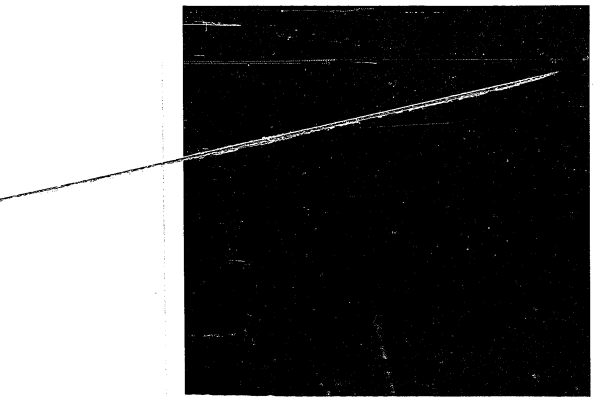

Figure 2-3a. After 5 by 5 average filtering.

Reproduced with permission of the copyright owner. Further reproduction prohibited without permission.

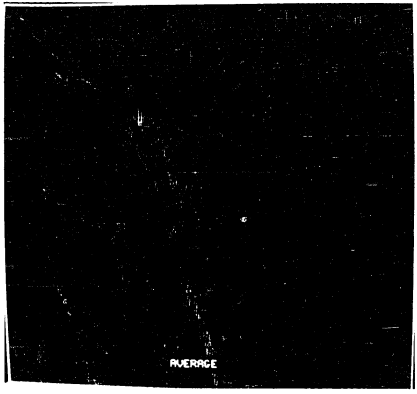

Figure 2-3b. The Robert's gradient edge detector implemented on the average-filtered image.

Reproduced with permission of the copyright owner. Further reproduction prohibited without permission.

Figure 2-4a. After 5 by 5 median filtering.

Reproduced with permission of the copyright owner. Further reproduction prohibited without permission.

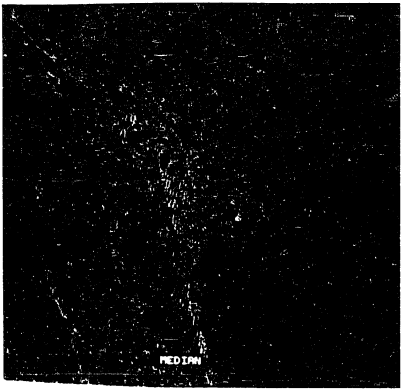

Figure 2-4b. The Robert's gradient edge detector implemented on the median-filtered image.

Reproduced with permission of the copyright owner. Further reproduction prohibited without permission.

Figure 2-5a. After 5 by 5 Lee filtering. σ_n^2 = .00613 within the window.

Reproduced with permission of the copyright owner. Further reproduction prohibited without permission.

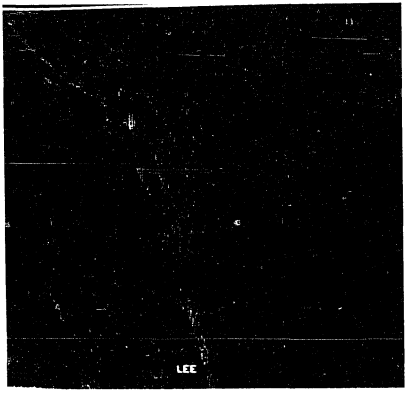

Figure 2-5b. The Robert's gradient edge detector implemented on the Lee-filtered image.

Reproduced with permission of the copyright owner. Further reproduction prohibited without permission.

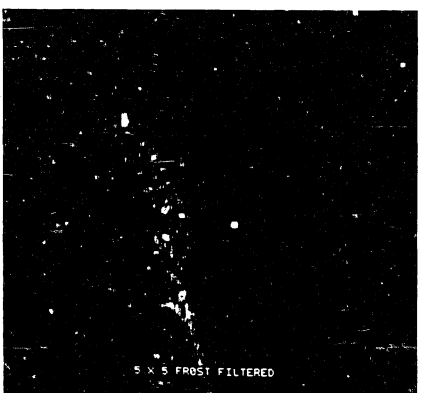

Figure 2-6a. After 5 by 5 Frost filtering. NF=40, α_m=.021, K=20.

Reproduced with permission of the copyright owner. Further reproduction prohibited without permission.

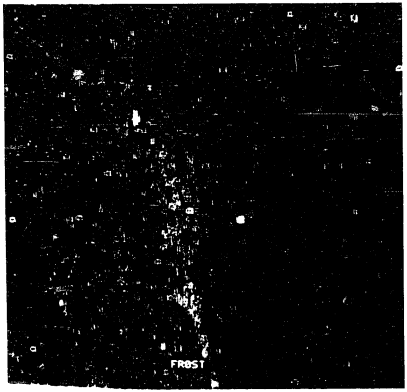

Figure 2-6b. The Robert's gradient edge detector implemented on the Frost-filtered image.

Reproduced with permission of the copyright owner. Further reproduction prohibited without permission.

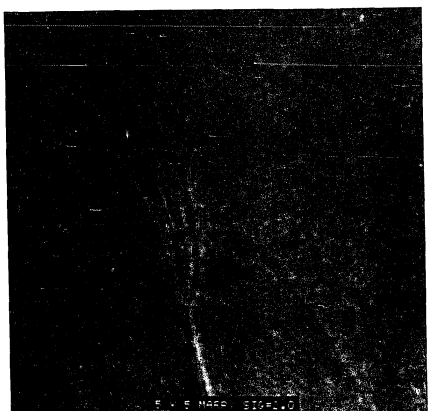

Figure 2-7a. After 5 by 5 Marr filtering. σ^2=2.0. No zero crossings exist.

Reproduced with permission of the copyright owner. Further reproduction prohibited without permission.

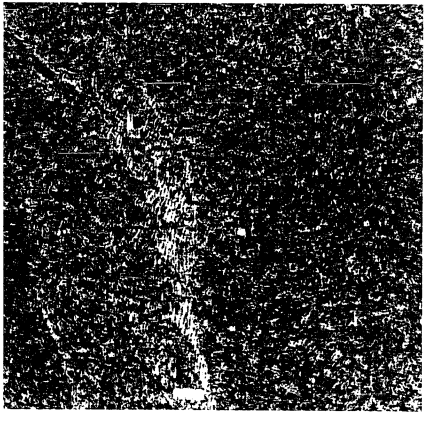

Figure 2-7b. The Robert's gradient edge detector implemented on the Marr-filtered image.

Reproduced with permission of the copyright owner. Further reproduction prohibited without permission.

of smoother/edge detector that the Marr filter can play by the selection of σ^2. The use of the Marr filter in no way precludes further edge detection, if appropriate values of σ^2 are chosen.

Speckle filters may also be valid preprocessing steps for texture analysis. Speckle is a noise process that should corrupt ideal scene texture statistics, although the uselessness of speckle in texture classification is not yet substantiated by experience.

2.3 Ocean Wave Spectra

Wave spectra creation is probably the most active area of SAR coastal image exploitation [24,25,26,27,28,29,30]. These spectra provide estimates of important environmental parameters such as wavelength, wave direction, straightness of wavefronts, wavefront continuity, and amount of refraction and diffraction. Spectra are created both optically and digitally. Digital spectra are created from the magnitude of the Fast Fourier Transform (FFT) of a scene. An integral part of digital spectra creation is geometric correction from the slant-plane to the ground-plane. This assures that extracted parameters reflect real world phenomena which have not been perturbed by SAR imaging geometry. The correction of range dependent intensity nonuniformity resulting from power drop-off in the antenna pattern provides an even better presentation of a scene with minimal imaging system distortion.

A digital slant-plane-to-ground-plane correction algorithm has been developed by Feldkamp [31]. The problem is depicted in Figure 2-8. A sinusoidal ocean wave in the ground plane would be imaged in the slant-plane having a higher frequency nearer the aircraft. The

Reproduced with permission of the copyright owner. Further reproduction prohibited without permission.

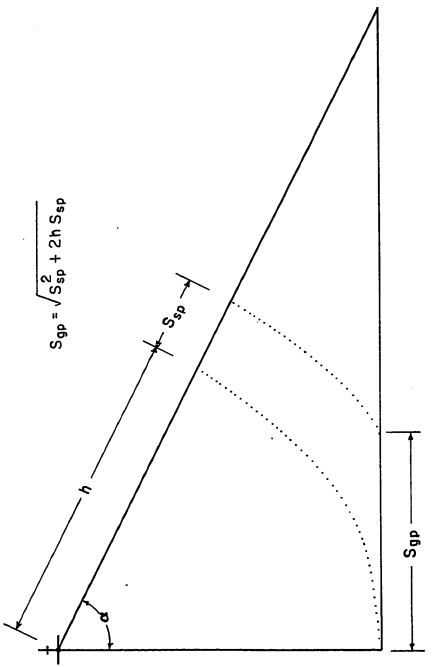

Figure 2-8. Projecting equally spaced samples in the slant-plane to the ground-plane.

Reproduced with permission of the copyright owner. Further reproduction prohibited without permission.

slant-plane spectrum would therefore be an incorrect representation of the true surface conditions, causing spreading in the frequency domain. It should be noted that this is only a range distortion. No correction is needed in azimuth. The solution is to project the slant-plane image samples into the ground-plane, then perform the FFT. Equally spaced samples in the slant-plane, when projected into the ground-plane are unequally spaced. The intersample distance increases nearer the radar. FFT routines require equally spaced samples. Therefore, the task is to interpolate between projected slant-plane samples to produce equidistant ground-plane samples for input to the FFT. This is done by convolving the projected slant-plane signal with a weighted "sinc" function. Feldkamp [31] implements this in an especially efficient manner by quantizing the number of possible interpolation sample positions to N. Then only N sampled versions of a continuous interpolation function need to exist, one for each possible interpolation output sample.

Range dependent intensity nonuniformity creates imagery brighter in near-range than far-range. Not only is the image less visually appealing, but it reveals energy attenuation unique to the imaging system rather than the environment. Some systems try to compensate for this in hardware. Goodyear SAR systems employ sensitivity time control (STC) circuitry to control gain as a function of altitude and depression angle [32]. Unfortunately, STC circuits assume that the aircraft operates within specific depression angle and altitude limits. SAR ocean imaging is usually done outside the STC design limits, causing over-compensation in far range for some cases. A digital gain correction is therefore necessary.

Reproduced with permission of the copyright owner. Further reproduction prohibited without permission.

Feldkamp [33] performs an approximate correction by realizing that the range intensity variation is a very low frequency spatial component. An array having as many elements as image pixels in a range scan is used to accumulate a mean range intensity function. This is done by summing all pixels at each range for an entire image, then dividing each sum by the number of pixels in an azimuth scan. The mean array is then low pass filtered to isolate a low frequency component which is an estimate of the antenna gain pattern. The multiplicative inverse of the filtered gain array, bounded by a maximum gain of approximately 20 dB, is then multiplied with each range scan in the image.

Digital exploitation of corrected wave spectra includes many activities traditionally done optically, as well as some activities unique to digital analysis. Annular rings in the frequency domain are used to calculate the energy within ocean wave frequency bands. The relative energy in different bands identifies dominant wave frequencies of the scene. Wedges in the frequency domain are analyzed to estimate energy in specific directions and to identify frequency and directional spreading of waves. These traditional concepts have been employed in the work of Mattie, et.al. [25], Meadows, et.al. [26] and Hayes, et.al. [27] to identify directional components and dominant wave frequencies. Meadows [26] performed frequency domain smoothing to reduce coherence before creating spectra and contour plots. Directional spreading due to wave shoaling was investigated by Mattie [25] who averaged spectra from different regions. Comparisons of averaged spectra from different regions revealed the shoaling effect.

2.4 Texture Analysis

Image textures are unit intensity patterns placed throughout the

Reproduced with permission of the copyright owner. Further reproduction prohibited without permission.

scene. By definition, textures are defined over regions. A unique spatial relationship characterizes each region and is a function of backscattered microwave interference in SAR imagery. Regions are not necessarily unique entities, although easily distinguished by the eye. They are often composed of smaller patterns placed in an order that creates a visually unique region. The smallest representative patterns are called unit patterns. The goal of texture analysis is therefore two-fold; to identify the unit patterns and to articulate the placement rules within a region.

An analytical tool for texture analysis that has proven itself is the gray level co-occurrence(GLC) matrix [34,35,36]. Each matrix, $S_\theta(d)$ is composed of elements, $S_\theta(i,j|d)$, each of which represents the probability of going from gray level i to gray level j in the θ direction, given that the intersample distance is d. The dimensions of $S_\theta(d)$ are the number of gray levels in the image. For computational efficiency, a maximum of sixteen gray levels is used. Gray level compression is routinely done on each image as a preprocessing step.

The only article in the literature which exploits radar image texture bases its analysis on the GLC matrix [37]. Measures defined on GLC matrices are then evaluated for their success at discriminating between regions. Shanmugan, et. al. [37] analyzed segments of a digitally correlated SEASAT scene over Tennessee. Six common measures were defined for the GLC matrices. These measures were:

1. Uniformity (or energy)

$$\sum_{i=0}^{N_G-1} \sum_{j=0}^{N_G-1} [S_\theta(i,j|d)]^2 \qquad (2\text{-}25)$$

Reproduced with permission of the copyright owner. Further reproduction prohibited without permission.

2. Contrast (or inertia)

$$\sum_{i=0}^{N_G-1} \sum_{j=0}^{N_G-1} (i-j)^2 S_\theta(i,j|d) \tag{2-26}$$

3. Correlation

$$\sum_{i=0}^{N_G-1} \sum_{j=0}^{N_G-1} (i-\mu_x)(j-\mu_y) S_\theta(i,j|d)/\sigma_x\sigma_y \tag{2-27}$$

4. Entropy (sometimes negated)

$$\sum_{i=0}^{N_G-1} \sum_{j=0}^{N_G-1} (S_\theta(i,j|d) \log S_\theta(i,j|d)) \tag{2-28}$$

5. Inverse difference moment (of which local homogeneity is a subset with $\rho=1$, $v=2$

$$\sum_{i=0}^{N_G-1} \sum_{j=0}^{N_G-1} S_\theta(i,j|d)^\rho / |i-j|^v \tag{2-29}$$

6. Maximum probability

$$\text{Max } S_\theta(i,j|d) \tag{2-30}$$

where

N_G = number of compressed gray levels ranging from 0 to N-1

$$\mu_x = \sum_{i=0}^{N_G-1} \sum_{j=0}^{N_G-1} S_\theta(i,j|d) \tag{2-31}$$

Reproduced with permission of the copyright owner. Further reproduction prohibited without permission.

$$\mu_y = \sum_{j=0}^{N_G-1} j \sum_{i=0}^{N_G-1} S_\theta(i,j|d) \qquad (2\text{-}32)$$

$$\sigma^2_x = \sum_{i=0}^{N_G-1} (i-\mu_x)^2 \sum_{j=0}^{N_G-1} S_\theta(i,j|d) \qquad (2\text{-}33)$$

$$\sigma^2_y = \sum_{j=0}^{N_G-1} (j-\mu_y)^2 \sum_{i=0}^{N_G-1} S_\theta(i,j|d) \qquad (2\text{-}34)$$

Four image textures representing different geological stress features were chosen. Only four of the six measures were applied and analyzed, uniformity, contrast, maximum probability and the inverse difference moment. GLC matrices were computed for d=1,2,4 and 8 pixels and θ=0,45,90 and 135 degrees. All four measures discriminated the four texture classes for all d's.

Alexander and Kritikos [38] did not exploit SAR imagery, but analyzed photographic and microwave scatterometer data to discriminate farm field roughness patterns. Photographic image textures were analyzed with six methods, the GLC method, annular rings and wedges in the Fourier domain [36], difference of regional averages [34], the gray level run length method [40], autocorrelation and Mitchell's Max.-Min. [41]. Of particular significance were eleven microwave roughness measures used in conjunction with the visible image textures. The functional relationship between the backscattered data against frequency or antenna depression angle for rough and smooth surfaces was the basis for the roughness measures. The functions were fit with a straight line as well as several other functions suggested by scattering theory. Measures of goodness of fit, slope, etc. became the

Reproduced with permission of the copyright owner. Further reproduction prohibited without permission.

feature measures used in discrimination. Alexander and Kritikos noted that the microwave measures were superior in differentiating field roughness. The implication for SAR ocean image analysis is encouraging since SAR's are essentially uncalibrated scatterometers. It is reasonable to assume that SAR texture measures based on modeled sea return will provide better discrimination results than general texture measures.

2.5 Image Simulation

Simulated SAR image generation has been studied as a mechanism for modeling SAR imagery. Successful modeling provides quantitative insight into SAR image information which may be exploited for various applications.

Holtzman, et. al. [42,43,44] has developed a point scattering model for image simulation. Extensive ground truth and radar system data are needed to create scenes that simulate speckle, terrain tilt, elevation differences and range layover. When ground truth, such as empirical backscatter data for different terrain types and elevations, is available, simulated radar images that an imaging, terrain following vehicle might create for navigation can be generated. Such an empirical backscatter data base also makes SAR image classification possible by matching actual image classes with simulated classes whose gray levels are a function of empirical data. Digitally simulated imagery of agricultural, flat land sights in Kansas demonstrated a visual quality very similar to the original radar imagery of the sight. Such images may be used to evaluate the human interpretation potential of proposed SAR systems. Optimized systems for specific

Reproduced with permission of the copyright owner. Further reproduction prohibited without permission.

visual analysis tasks may then be designed.

Stiles, et.al. [45] identified exploitation techniques for actual SAR imagery which may be developed from statistical modeling used in simulation. The adaptive speckle filter of Frost [18] is one example. Another technique is geometric registration of an actual SAR image by matching it with a simulated, correctly registered, reference image. Investigations have also been made on model based data compression, compressing not only for reduced signal processing during correlation, but to reduce the bandwidth of raw SAR signals. A final technique is to simulate SAR complex phase histories by generating Gaussian random samples for the in-phase and quadrature received voltage signals. This would allow angular, frequency or polarization diversity to be introduced to digital correlation, resulting in SAR improvements in detected imagery through non-coherent integration.

Reproduced with permission of the copyright owner. Further reproduction prohibited without permission.

REFERENCES

1. Brown, W.M. and L.J. Porcello, "An Introduction to Synthetic Aperture Radar," IEEE Spectrum , (Sept. 1969), pp. 52-62.

2. Brown, W.M., "Synthetic Aperture Radar," IEEE Trans. Aero. Elect. Syst., Vol. AES-3, No. 2 (Mar. 1967), pp. 217-229.

3. Ausherman, D.A., "Digital vs. Optical Techniques in SAR Data Processing," Technical article, Environmental Research Institute of Michigan, Ann Arbor, MI.: ERIM, 1978.

4. Cutrona, L.J., E.N. Leith, L.J. Porcello, W.E. Vivian, "On the Application of Coherent Optical Processing Techniques to Synthetic Aperture Radar," Proc. IEEE , Vol. 54, no. 8 (Aug. 1966), pp. 1026-1032.

5. Kirk, J.C., "A Discussion of Digital Processing for Synthetic Aperture Radar," IEEE Trans. Aero. Elect. Syst., Vol. AES-11, No. 3 (May 1975), pp. 326-337.

6. Ausherman, D.A., W.D. Hall, J.N. Latta, J.S. Zelenka, "Radar Data Processing and Exploitation Facility," Proc. IEEE Intl. Radar Conf., (1975), pp. 493-498.

7. Wu, C., "A Digital System to Produce Imagery from SAR Data," Proc. Aiaa Syst. Design Driven Sensors Conf., Paper No. 76-968, Pasadena, CA. (Oct. 1970).

8. Wu, C., B. Barkan, H. Honeycutt, C. Leang, S. Prang, An Introduction To The Interim Digital SAR Processor And The Characteristics Of The Associated SEASAT SAR Imagery , JPL Pub. 81-26, Pasadena, CA.: Jet Propulsion Lab., 1981.

9. Wu, C., "A Digital Fast Correlation Approach to Produce SEASAT SAR Imagery," in Proc. IEEE 1980 Intl. Radar Conf., Arlington, VA. (1980), pp. 153-160.

10. Van de Lindt, W.J., "Digital Technique for Generating Synthetic Aperture Radar Images," IBM J. Res. Dev., Vol. 21, No. 5 (Sept. 1977), pp. 415-432.

11. Goodman, J.W., "Some Fundamentals of Speckle," J. Opt. Soc. Amer., Vol. 21, No. 5 (Sept. 1977), pp. 415-432.

12. Raney, R.K. and R.A. Shuchman, "SAR Mechanisms for Imaging Waves,"

Reproduced with permission of the copyright owner. Further reproduction prohibited without permission.

in 5th Canadian Symposium Remote Sensing Proc., PROC. (Aug. 1980), pp. 495-505.

13. Raney, R.K., "SAR Response to Partially Coherent Phenomena," IEEE Trans. Ant. Prop., Vol. AP-28, No. 6 (Nov. 1980), pp. 777-787.

14. Raney, R.K., "SAR Processing of Partially Coherent and Sinusoidally Dynamic Ocean Waves," in Oceanography From Space , J.F.R. Gower, ed., New York, N.Y.: Plenum, 1981, pp. 497-504.

15. Porcello, L.J., N.G. Massey, R.B. Innes, J.M. Marks, "Speckle Reduction in Synthetic Aperture Radars," J. Opt. Soc. Amer., Vol. 66, No. 11 (Nov. 1976), pp. 1305-1311.

16. Guenther, B.C., "Digital Processing of Speckle Images," Proc. 1978 Conf. Pattern Recog. Image Proc., Chicago, IL. (May 1978), pp. 85-90.

17. Dicaprio, G.R. and J.E. Wasielewski, "Radar, Image Processing, and Interpreter Performance," Photogram. Eng. Remote Sensing , Vol. 52 (Aug. 1976), pp. 1043-1048.

18. Frost, V.S., J.A. Stiles, K.S. Shanmugan, J.C. Holtzman, "A Model for Radar Images and its Application to Adaptive Digital Filtering of Multiplicative Noise,: IEEE Trans. Pattern Anal. Mach. Intell., Vol. PAMI-4, No. 2 (Mar. 1982), pp. 157-166.

19. Lee J.S., "Speckle Analysis and Smoothing of Synthetic Aperture Radar Images," Comp. Graph. Image Proc., Vol. 17 (1981), pp. 24-32.

20. Lee, J.S., "Refined Filtering of Image Noise Using Local Statistics," Comp. Graph. Image Proc., Vol. 15 (1981), pp. 380-389.

21. Marr, D. and E.C. Hildreth, "Theory of Edge Detection," Proc. R. Soc. Lond., Vol. B-207 (1980), pp. 187-217.

22. Hildreth, E.C., "Edge Detection in Man and Machine," Robotics Age , Vol. 3, No. 5 (Sept.-Oct. 1981), pp. 8-14.

23. Mastin, G., C.A. Harlow and R.W. Conners, "Digitization and Preprocessing of SAR Optical Ocean Imagery," RSIP Tech. Report No. RSIP TR 103.83, Remote Sensing and Image Processing Lab., Louisiana State University, Baton Rouge, LA, March 1983.

24. Gonzalez, F.I., R.C. Beal, W.E. Brown, J.F.R. Gower, "SEASAT Synthetic Aperture Radar: Ocean Wave Detection Capabilities," Science , Vol. 204 (June 1979), pp. 1418-1421.

25. Mattie, M.G., S.V. Hsiao, D.D. Evans, "Wave Direction Measured by Four Different Systems," IEEE J. Oceanic Engineering , Vol. OE-6, No. 3 (July 1978), pp. 87-93.

Reproduced with permission of the copyright owner. Further reproduction prohibited without permission.

26. Meadows, G.A., E.S. Kasischke, R.A. Shuchman, "SAR Observations of Coastal Zone Conditions," Proc. 14th Intl. Symp. Remote Sensing Environ., Vol. 2 (Ann Arbor, MI.: ERIM, April 1980), pp. 845-863.

27. Hayes, J.G. and R.A. Shuchman, "SEASAT SAR Ocean Surface Current and Shallow Water Wave Refraction," in Oceanography From Space, J.F.R. Gower, ed., New York, N.Y.: Plenum, 1981, pp. 469-476.

28. Shuchman, R.A., E.S. Kasischke, G.A. Meadows, "Detection of Coastal Zone Environmental Conditions Using Synthetic Aperture Radar," Digest IEEE Geosci. And Remote Sensing Soc., Vol. 2, Washington, D.C.: (June 8-10, 1981), pp. 756-767.

29. Shuchman, R.A., E.S. Kasischke, A. Klooster, "Synthetic Aperture Radar Studies," ERIM Final Report, NOAA Contract No. 7-35328, Environmental Research Institute of Michigan, Ann Arbor, MI.: ERIM, Sept. 1978.

30. Shuchman, R.A., E.S. Kasischke, "Refraction of Coastal Ocean Waves," in Spaceborne Synthetic Aperture Radar For Oceanography, Baltimore, MD.: Johns Hopkins Univ. Press, 1981, pp. 128-135.

31. Feldkamp, G.B., "Correction of SAR-Induced Distortion in SEASAT Imagery," Paper presented SPIE Conf. Appl. Digital Image Proc., San Diego, CA. (Aug. 1978).

32. Goodyear Aerospace Co., "SAR: Fundamentals of Synthetic Aperture Radar System Employing Optical Correlation," Report No. GIB-9399A, Goodyear Aerospace Arizona Division, Litchfield Park, AZ., Aug. 1978.

33. Feldkamp, G.B., Personal communication.

34. Weszka, J.S., C.R. Dyer, A. Rosenfeld, "A Comparative Study of Texture Measures for Terrain Classification," IEEE Trans. Syst. Man Cybernet., Vol. SMC-6 (April 1976), pp. 269-285.

35. Conners, R.W. and C.A. Harlow, "A Theoretical Comparison of Four Texture Analysis Algorithms," IEEE Trans. Pattern Anal. Mach. Intell., Vol. PAMI-2, No. 3, (May 1980), pp. 204-222.

36. Conners, R.W. and C.A. Harlow, "Toward a Structural Textural Analyzer," Comp. Graph. Image Proc., Vol. 12, No. 3 (March 1980), pp. 224-256.

37. Shanmugan, K.S., V. Narayanan, V.S. Frost, J.A. Stiles, J.C. Holtzman, "Texture Features for Radar Image Analysis," IEEE Trans. Geo. Remote Sensing, Vol. GE-119, No. 3 (July 1981), pp. 153-156.

38. Alexander, L., and H. Kritikos, "An Investigation of the Relation Between Radar Images and Visible Texture," Proc. 5th Intl. Conf. Pattern Recog., Vol. 2, Miami Beach, FL. (Dec. 1-4, 1980) pp. 795-799.

Reproduced with permission of the copyright owner. Further reproduction prohibited without permission.

39. Bajcsy, R., "Computer Description of Textured Surfaces," Third Intl. Joint Conf. Artif. Intell., Stanford Univ., (Aug. 1973).

40. Galloway, M.M., "Texture Analysis Using Gray Level Run Lengths," Comp. Graph. Image Proc., No. 4 (1975), pp. 172-179.

41. Mitchell, O.R., C.R. Myers, W. Boyne, "A Max-Min Measure for Texture Analysis," IEEE Trans. Comp., Vol. C-26, No. 4 (April 1977), pp. 408-414.

42. Holtzman, J.C., V.H. Kaupp, R.L. Martin, E.E. Komp, V.S. Frost, "Radar Image Simulation Project: Development of a General Simulation Model and an Interactive Simulation Model and Sample Results," RSL Tech. Report No. 234-13, Remote Sensing Lab., Univ. Kansas Center for Research, Lawrence, Kan., Feb. 1976.

43. Holtzman, J.C., V.H. Kaupp, J.L. Abbott, V.S. Frost, E.E. Komp, E.C. Davison, "Radar Image Simulation: Verification of the Point Scattering Method," Tech. Report, Remote Sensing Lab., Univ. Kansas Center for Research, Lawrence, Kan., Sept. 1977.

44. Holtzman, J.C., V.S. Frost, J.L. Abbott, V.H. Kaupp, "Radar Image Simulation," IEEE Trans. Geosci. Elect., Vol. GE-16, No. (Oct. 1978), pp. 296-303.

45. Stiles, J.A., V.S. Frost, K.S. Shanmugan, J.C. Holtzman, "A Model for Simulation and Processing of Radar Images," Digest IEEE Geosci. Remote Sensing Soc., Vol. 1, Washington D.C.: (June 8-10, 1981), pp. 273-283.

Reproduced with permission of the copyright owner. Further reproduction prohibited without permission.

CHAPTER 3

PREPROCESSING

Preprocessing is the preparation process which takes the raw SAR phase histories through precision correlation, digitization, and geometric correction to the point where the digital imagery can be analyzed by the computer. The following paragraphs document the preprocessing steps implemented on the Japanese SAR data analyzed in this dissertation. The final two sections of this chapter document antenna pattern shading correction and speckle reduction, optional steps whose use depends upon the characteristics of the SAR and the analysis desired.

3.1 The Data

The SAR data used in these studies was collected by the Japan Self Defense Air Force using a Goodyear AN/UPD-4 radar installed in an American-made F4 Phantom. The resolution of the SAR is 2.3 m in the range (across track) dimension and 3.0 m in azimuth (along track). Three missions were flown over the Gotoh Islands and the island of Tsushima on August 31, 1981, November 19, 1981, and November 27, 1981 (see Figure 3-1). All data were optically collected and processed. Along with the raw complex phase history data, field correlation prints were supplied by the Japanese. The prints included encoded data blocks every five nautical miles (nmi) in azimuth giving flight parameters such as altitude, latitude, longitude, date, time, radar mode, pitch, roll, drift, heading and barometric altitude. Figure 3-2 shows the

Reproduced with permission of the copyright owner. Further reproduction prohibited without permission.

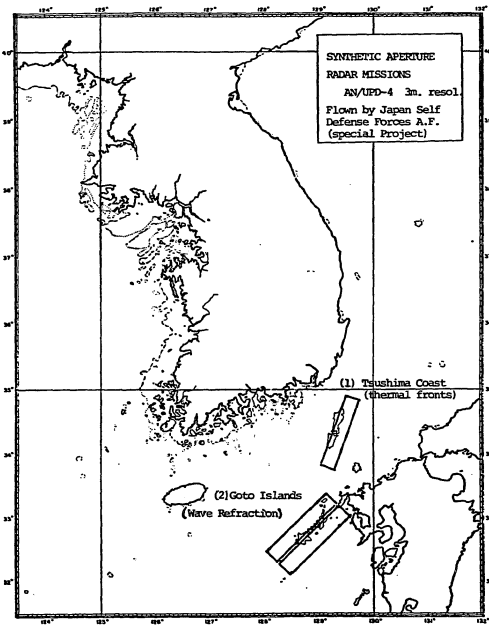

Figure 3-1. Synthetic aperture radar missions, flight paths, and image swaths. (1) Tsushima coast for thermal fronts and possible reflected surface waves. (2) Goto Islands for tidal inlets and wave refraction.

Reproduced with permission of the copyright owner. Further reproduction prohibited without permission.

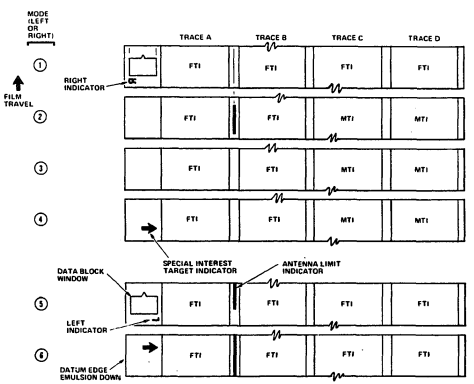

Figure 3-2. 9.5 inch image film format [1].

Reproduced with permission of the copyright owner. Further reproduction prohibited without permission.

field-correlated data format of the prints, with trace A being near-range and trace D, far-range.

The raw complex phase histories for the three missions were re-correlated on the precision optical correlator at the Goodyear Aerospace Corporation in Litchfield Park, Arizona. Unlike the field correlator which correlates all four traces at once, the precision optical correlator correlates each trace independently and records it on a 70 mm wide film strip. This permits greater flexibility in focusing and enhancing sea return for all four traces. Correlation and film developing parameters were tightly controlled and were recorded for later reference. Each film processing was preceded by a step wedge which was later calibrated with a micro-densitometer. This information was used to determine the film gamma, as well as the digitization dynamic range, which is discussed next.

3.2 Digitization

The precision correlated image data was digitized for subsequent analysis by computer. Two systems were used to digitize the data, each of which is capable of producing a dynamic range of 256 gray levels. The film data contains both sea and land return, but only sea return was of interest here. Therefore, a representative subset of the sea return for all three missions was measured with a calibrated micro-densitometer. The dynamic range of the sea return was then indicated on the step wedge preceding each film processing. The dynamic range of the camera digitizing system was then centered about these step wedge values for digitization.

The first digitizations were done at the Naval Oceanographic

Reproduced with permission of the copyright owner. Further reproduction prohibited without permission.

Research and Development Activity (NORDA) computer facility at NSTL Station, Mississippi. A set of twelve, 512 x 512 pixel scene digitizations and twelve calibration images of the same size were made. The calibration images were made to later correct for intensity nonlinearities introduced by the vidicon camera and light source. The digitization system was an I^2S model 70,running with an HP-3000 minicomputer.

All other digitizations were done at the Remote Sensing and Image Processing (RSIP) laboratory at Louisiana State University. A Hamamatsu C1000 vidicon camera system interfaced with a Perkin-Elmer 3220 minicomputer performed the digitization.

The same digitizing procedure was followed at both the NORDA and RSIP facilities. Figure 3-3 outlines the procedure. The 50 x 50 mm digitization window corresponds to the full width of data recorded on the 70 mm film by the precision optical correlator. The resampled resolution is 0.098 mm/pixel in the film, or approximately 10 m/pixel in the scene. Assuming that the digitized image is band-limited to a spatial frequency of 0.5 cycles/pixel, the Nyquist criteria tells us that the smallest spatial period recorded in the resampled image is 0.195 mm/wave cycle. Therefore, the data were adequately sampled for ocean wave analysis. All digitization was done so that the azimuth dimension corresponded to the vertical dimension of the displayed image, and the range dimension corresponded to the horizontal display dimension. This was necessary for slant-range-to-ground-range correction during later preprocessing.

3.3 Digitization Shading Correction

Gray level nonuniformities are always introduced during digitization and must be corrected before performing computer image analysis.

Reproduced with permission of the copyright owner. Further reproduction prohibited without permission.

Nonuniformities arise from two sources; 1) nonlinear response characteristics of the vidicon camera as a function of time and position in the field of view, and 2) nonuniformity of the light source (backlighting the film) as a function of position. Time nonlinearities in the vidicon can be compensated by digitizing calibration scenes periodically. In this work, a step wedge, a white scene, a gray scene and a black scene were digitized ahead of each trace's data, thereby compensating for time nonlinearities. Three algorithms for position nonuniformity correction were considered. These were, 1) simple subtraction of a white scene from each image, 2) a method suggested by Sawchuck [1], and 3) a method suggested by Onoe, et.al [2]. The latter two methods are based on a shading model having additive and multiplicative components, while the first method ignores the multiplicative component.

Sawchuck [1] models imaging system shading as,

$$g(\mu_1, \mu_2) = R_{\mu_1,\mu_2}(f(\mu_1,\mu_2)) \qquad (3\text{-}1)$$

where

$(\mu_1,\mu_2) = \vec{\mu}$ = a point in the two-dimensional image plane,

$f(\vec{\mu})$ = input image intensity at a point,

$g(\vec{\mu})$ = output image intensity at a point,

R_{μ_1,μ_2} = system intensity distortion function.

The fact that R_{μ_1,μ_2} is a function of $f(\vec{\mu})$ and $\vec{\mu}$ attests to its nonlinearity. R_{μ_1,μ_2} is a actually a set of pointwise distortion functions having as many elements as picture points. By expanding $g(\vec{\mu})$ in a Taylor series about a fixed intensity level, $f_0(\vec{\mu})$, and keeping the first two terms, one gets

Reproduced with permission of the copyright owner. Further reproduction prohibited without permission.

$$g(\vec{\mu}) = a_0(\vec{\mu}) + a_1(\vec{\mu})f(\vec{\mu}) \tag{3-2}$$

where $a_0(\vec{\mu})$ is the additive component and $a_1(\vec{\mu})$ is the multiplicative component. Correction is done by implementing

$$f(\vec{\mu}) = \frac{g(\vec{\mu}) - a_0(\vec{\mu})}{a_1(\vec{\mu})} \tag{3-3}$$

When a black image is scanned, $f(\vec{\mu}) = 0$ and

$$g(\vec{\mu}) = a_0(\vec{\mu}) \tag{3-4}$$

which is a measure of the additive component. When a white image is scanned, $f(\vec{\mu}) = k$ and

$$a_1(\vec{\mu}) = \frac{1}{k}(g(\vec{\mu}) - a_0(\vec{\mu})) \tag{3-5}$$

which is a measure of the multiplicative component. Sawchuck [1] corrects the image via equation (3-3). Onoe et.al. [2] quite similarly computes a multiplicative scale factor,

$$M(\vec{\mu}) = \frac{k\, a_1(\vec{\mu})_{max}}{a_1(\vec{\mu})} \tag{3-6}$$

where k is chosen to set the dynamic range of the output, and corrects via the equation

$$f(\vec{\mu}) = g(\vec{\mu})\, M\, (\vec{\mu}) \tag{3-7}$$

Onoe's method was implemented on the Japanese data.

Reproduced with permission of the copyright owner. Further reproduction prohibited without permission.

DIGITIZATION PROCEDURE

1. Warm up the camera for approximately 30 min.

2. Set up the camera height so that a 50 x 50 mm window is imaged. Secure the camera. Don't change the height again.

3. Set the focus by examining an SAR image on the monitor. Don't change the focus.

4. Set the light source intensity as high as possible.

5. Be sure the film is oriented so that the right side of the resulting image corresponds to near-range. This is important for geometric correction and antenna compensation.

6. Before digitizing a trace's worth of data:
   a) Scan the portion of that trace's step wedge corresponding to the sea return microdensitometer results. Save the image. Don't adjust the aperture again for this trace.
   b) Scan the exposed, clear portion of the film just behind the step wedge. Save the image.
   c) Put a filter over the clear portion just scanned. Scan this intermediate gray shade. Save the image.
   d) Put the lens cap on the camera. Scan. Save the image.

7. Digitize that trace's data. Don't change any camera settings.

8. Go to step 6 until done.

Figure 3-3. SAR Optical Imagery Digitization Procedure

Reproduced with permission of the copyright owner. Further reproduction prohibited without permission.

3.4 Slant-Range-to-Ground-Range Correction

Slant-range-to-ground-range correction of the digitized imagery was performed with Feldkamp's algorithm [3,4]. Required input to the algorithm was aircraft altitude, range resolution (in this case, the resampled resolution) and the distance to the near-edge of the scene in slant-range. The software expects the left-hand side of the digital image to be near-range. In some cases, this required the digitized image to be digitally flipped, right side over the left, after digitization shading correction. These cases occurred whenever a) digitizing the image film with the emulsion side down resulted in an inverted image, or b) the film was digitized with the near-range and far-range dimensions swapped.

Computation of the distance to the near-edge of the scene is a critical factor in slant-range-to-ground-range correction, especially for image trace A. The distance to the near-edge of the scene is determined by the timing of the SAR's range gate. For the AN/UPD-4 system operating in mode 1, as it did for all the Japanese data, the range gate time is held constant, independent of aircraft altitude, and the slant-range to the scene's near-edge is always 2.46 nmi (4556 m) [5]. The distance to the scene's near-edge, however, is not the range in the slant-plane to the beginning of trace A. Each trace allows space for 0.25 nmi of scene overlap from the previous trace. This assures there are no gaps in the scene despite being composed of four traces. Since trace A is the first trace, there is no preceding trace to overlap onto trace A. The first 0.25 nmi of trace A (approx. 3/16 in on the film) are included as part of the distance to the scene's near-edge. When computing the near-edge distance for traces

Reproduced with permission of the copyright owner. Further reproduction prohibited without permission.

B through D, the distance to the near-edge of trace A was offset by the slant-plane range of each preceding trace. Each trace is 2.5 nmi wide and includes 0.25 nmi of overlap. Range marks separated by 0.5 nmi often occur in the traces and are helpful in determining the offsets.

As a final note, it should be mentioned that slant-range-to-ground-range correction maps the 512 range points of the input image into 512 ground-range output points, but due to the correction geometry, the corrected scene will be smaller in extent than the input scene. For example, for an aircraft altitude of 3850 m, the 4630 m of extent in slant-plane trace A maps to 6608 m in ground-range. Since the interpolation done for correction preserves pixel resolution, only 4630 m of the full ground-range extent of 6608 m can be corrected and displayed. To correct the far-range data in trace A, an appropriate offset to be added to the distance to the scene's near-edge must be calculated.

3.5 Antenna Shading Correction

Power attenuation with range in the main antenna lobe results in a shading nonuniformity in the range dimension of SAR imagery. Some SAR systems do not attempt to correct this problem, so a pseudo antenna correction must be done in software. A method suggested by Feldkamp [6] is to sum columns of the slant-range imagery and compute a mean intensity vector for the range dimension, low-pass filter the vector to isolate the low frequency antenna component, and multiply each line of the image by the inverse of the filtered vector. This capability is supported by the RSIP SAR preprocessing software, but was not used

Reproduced with permission of the copyright owner. Further reproduction prohibited without permission.

on the Japanese data. The AN/UPD-4 system includes sensitivity time control (STC) hardware to correct for range-dependent power attenuation. The Japanese data was collected by flying the aircraft at a lower altitude than recommended for mode 1 reconnaissance. The STC hardware should, theoretically, over-compensate for the near-range data in this case. Examination of digital intensity profiles in range for twelve images showed no trend toward over-compensation. Therefore, antenna shading correction was not performed on the Japanese data. The STC hardware correction was considered to be adequate.

3.6 Speckle Reduction

Speckle reduction, as discussed in Chapter 2, was not performed on the Japanese data. The speckle content of the digitized Japanese data is quite low. This can be attributed to two factors. First, and the most minor factor, is the transfer function inherent in film recording. The film performs a logarithmic encoding of the data which can be conceptualized as a filtering function. The major factor is resampling by the optics of the vidicon camera during digitization. The transfer function of the optics acts to low-pass filter the data, thereby reducing the speckle content of the data. Figure 2 of Chapter 2 was sampled at a much higher resolution by a process which does not involve an optical transfer function, and therefore does not demonstrate digitization speckle reduction. Higher spatial resolution digitizations with the vidicon camera, however, would likely require some digital speckle reduction processing.

Reproduced with permission of the copyright owner. Further reproduction prohibited without permission.

REFERENCES

1. Sawchuck, A.A., "Real-Time Correction of Intensity Nonlinearities in Imaging Systems." IEEE Trans. Comp., Vol. C-26, No. 1 (Jan. 1977), pp. 34-39.

2. Onoe, M., M. Ishizuka, K. Tsuboi, "Real-Time Shading Corrector for a Television Camera Using a Microprocessor," in Real Time/Parallel Computing , M. Onoe, K. Preston, A. Rosenfeld, Ed., New York: Plenum, 1981, pp. 339-346.

3. Feldkamp, G.B., "Correction of SAR-Induced Distortion in SEASAT Imagery," Paper presented SPIE Conf. Appl. Digital Image Proc., San Diego, CA., (Aug. 1978).

4. Mastin, G.A., "Digital Interpolation of Synthetic Aperture Radar Data Using Digital Filters," Software Documentation, Remote Sensing and Image Processing Lab., Louisiana State University, Baton Rouge, LA., 1981.

5. Goodyear Aerospace Co., "AN/UPD-4 Side-Looking Radar System: Principles of Mission Planning," Report No. GIB-9369B, Goodyear Aerospace Arizona Division, Litchfield Park, Ariz., April 1975.

6. Feldkamp, G.B., Personal communication.

Reproduced with permission of the copyright owner. Further reproduction prohibited without permission.

CHAPTER 4

SYNOPTIC SAR OCEAN SCENE ANALYSIS: THE GEOPHYSICAL PERSPECTIVE

Several key scenes highlighting unique wave, wind and frontal patterns are presented here for qualitative and quantitative analysis. From the qualitative point of view, the purpose is to identify SAR discernible features and, with the available auxiliary data, to relegate the features to one of the four classes of ocean patterns identified in chapter 1. Unique examples of feature classes must be identified if the long-range goals of automatic or semi-automatic digital scene analysis are to be achieved. From the quantitative point of view, the accepted technique of spectrum analysis is exploited a) to extract wave parameters directly which may be used in some cases to estimate hydrodynamic and aerodynamic parameters not previously discussed in SAR literature, b) to extract wind directions directly which is impossible in L-band SEASAT SAR and which has not been reported in the literature for aircraft SAR data, and c) to exploit digital processing to generate encoded imagery imparting more synoptic information to interpreters than the imagery itself. For clarity's sake, each scene or scene type will be discussed under a separate heading. The scene by scene analysis shall be preceded by a discussion of the analytical techniques used and their justification.

Reproduced with permission of the copyright owner. Further reproduction prohibited without permission.

4.1 Analytical Techniques

A fundamental goal of synoptic SAR scene analysis of surface waves is to extract wave length, period, direction, phase speed and height at any point within the scene. Wavelength and direction extraction from SAR imagery is well documented [1,2,3,4]. These parameters are traditionally extracted from two-dimensional digital or optical Fourier transforms. Vesecky and Stewart [5] report an average error between SEASAT extracted wavelengths and in situ measurements of 12%. Shuchman, et.al. [4] report RMS errors between aircraft SAR extracted wavelengths and in situ measurements of 7.9% for X-band and 8.3% for L-band during the Marineland experiment. RMS wave direction errors for the Marineland experiment were 9.8% for X-band and 16.3% for L-band. The significance of these results is that wave direction and length are reasonably extracted from SAR imagery, despite differences in radar wavelength, whether the SAR is airborne or spaceborne, or whether the data are digitally or optically processed. Deep water wave relations allow wave period and phase speed to be calculated from the wavelength. Wave height, however, is not directly discernible from the imagery. Jain [6] and Harger [7] have suggested somewhat involved processes of estimating wave height from the SAR optical and digital complex phase histories, respectively. In many cases, facilities and the full ensemble of data needed for these techniques are not available. Empirical models, however, are known for estimating wave height from wavelength, wind speed and fetch [8,9].

The quantitative analysis carried out in this chapter is based on direction and wavelength extraction from two-dimensional digital fast Fourier transforms (FFT's) and parameter estimation with empirical re-

Reproduced with permission of the copyright owner. Further reproduction prohibited without permission.

lations. Dominant components in the magnitude of the fast Fourier transforms (mag. FFT) were judged visually after 3 by 3 pixel median filtering of the log encoded mag. FFT, followed by thresholding at the mean plus one standard deviation. These components were usually characterized by clusters of approximately four to nine pixels, having gray levels four or more counts higher than those adjacent to the clusters. The brightest pixel in a median filtered image cluster was chosen as the dominant frequency component. Less dominant components were judged as clusters having lower gray level and/or less dense pixel groupings. These frequency components were converted to wavelengths by a computer program which then calculated wave period and phase speed, assuming a deep water scenario. The deep water scenario is well suited to data around the Gotoh Islands because of the rugged and deep bathymetry. Based on an in situ wind speed entered by the user, the program estimated the wave height, wind shear velocity, the wind shear coefficient, the dynamic roughness length and the whitecap percentage from empirical relations documented in the literature. The specific relations shall be discussed shortly. Not all wavelengths or SAR scene environments lend themselves to estimation of all these parameters. Auxiliary information about the scene was used to judge which parameters were meaningful. Parameters such as wind shear velocity or the dynamic roughness length are impossible to verify with surface truth. The empirical relations for estimating these parameters, however, are based on analysis of very large data sets, globally gathered, and are not without meaning in SAR scene analysis. Their use here is to emphasize their utility when reliable wind speed and wavelength data can be provided, wholly or partially, from a SAR sensor. Despite the shortcoming

Reproduced with permission of the copyright owner. Further reproduction prohibited without permission.

of verification, SAR scene analysis is the best mechanism for all weather, day/night parameter estimation, and, as such, is a unique contribution.

The empirical relations are presented here before discussing the analysis of specific scenes. Hasselmann, et.al. [9] developed an empirical wave forecasting model as a function of fetch, wave frequency and wind speed using laboratory and JONSWAP field experimental data. This model allows the significant wave height in a scene to be estimated, knowing only the significant wave period, T_w, and the wind speed, U_{10SEA}.

$$\sigma = \left(\frac{U_{10SEA}}{g}\right)^2 4 \times 10^4 \left(\frac{22\ g\ T_w}{2\pi\ U_{10SEA}}\right)^{3/2} \qquad (4\text{-}1)$$

where g is the acceleration due to gravity in m/s-s and σ is the surface displacement.

$$H \simeq 4\sigma \qquad (4\text{-}2)$$

where H is the significant wave height. The key to using this relation is to verify that the dominant wavelength measured from the SAR mag. FFT is coupled with the wind generating the wave field whose speed is supplied by the analyst. In those cases where U_{10SEA}, the wind speed measured 10 m above the sea, cannot be directly measured, corrections must be made. A wind speed from a land based station is an example. First, the power wind profile relation [10] must be used to correct the wind speed from a station height, z m, to 10 m:

$$U_{10} = U_Z\left(\frac{10}{Z}\right)^{1/7}. \qquad (4\text{-}3)$$

Reproduced with permission of the copyright owner. Further reproduction prohibited without permission.

The power 1/7 has been suggested by Blackadar [11] and is related to thermal stability. Correction from land wind speed to sea wind speed is given by [12],

$$U_{10SEA} = 3U_{10}^{2/3} \tag{4-4}$$

Amorocho and DeVries [13] have developed an empirical model for calculating the wind shear velocity, U_*. The wind shear velocity is an indication of aerodynamic roughness at the boundary layer.

$$U_* = \left\{ 0.0015 \left[1 + \exp\left(-\frac{U_{10SEA} - 12.5}{1.56}\right)\right]^{-1} + 0.00104 \right\}^{\frac{1}{2}} U_{10SEA} \tag{4-5}$$

where

$U_* <= 0.23$ m/s	low roughness,
0.23 m/s $< U_* <$ 0.98 m/s	transitional roughness,
$U_* >= 0.98$ m/s	high roughness.

The wind stress coefficient, C_{10}, can also be calculated.

$$C_{10} = 0.0015 \left[1 + \exp\left(\frac{U_{10SEA} - 12.5}{1.56}\right)\right]^{-1} + 0.00104 \tag{4-6}$$

Given H, U_* and the wave phase speed, c, the dynamic roughness length, Z_0, can be calculated [14]:

$$Z_0 = \left[\frac{1}{2\pi} \frac{H}{(c/U_*)^2}\right] . \tag{4-7}$$

Wu [15] averaged results obtained by different investigators under various stability conditions to relate whitecap coverage, W, to wind speed:

$$U_{10SEA} = 0.87W^{0.267} \tag{4-8}$$

Reproduced with permission of the copyright owner. Further reproduction prohibited without permission.

where W is expressed in parts per million (ppm). The whitecap percentage is significant in aerosol studies. Laboratory studies by Wu [16,17] have led to an expression for the droplet concentration, in droplets/cm-s, as a function of elevation, h (in m), wind speed at 10 m height, U_{10SEA} (in m/s), wind shear velocity, U_* (in m/s), and a reference elevation, h_0 (in m).

$$N = \exp[\, 2.5\ (U_{10SEA} - 7.5 - 4.9\ h_0)]h^{\,(3.3+2.6U_*)} \qquad (4\text{-}9)$$

The parameter h_0 is the key value to be used when determining the droplet concentration in the sea, rather than the lab. The 10 cm reference height used in the laboratory is too small for use in the sea. No value for h_0 in the sea has been determined [17], therefore, valid prediction of droplet concentration from SAR imagery is not yet possible. This information is necessary for anticipating acoustic and electromagnetic wave propagation attenuation by spray in the coastal environment (see chpt. 1).

4.2 Qualitive and Quantitative Scene Analysis

The location of the scenes highlighted here are shown in figures 4-1 through 4-3. There is one map for each of the missions: August 31, November 19, and November 27, 1981. Each square of a map represents a 512 by 512 pixel image and is assigned a unique scene identifier. The form of the identifier is the date, followed by the trace, followed by a three character frame identifier. For example, N27B.FM5 means November 27, 1981, trace B, digitized frame number 5. Some scenes in this section are slant-plane images, while others have been digitally converted to the ground-plane. The imaging plane is identified in each case.

Reproduced with permission of the copyright owner. Further reproduction prohibited without permission.

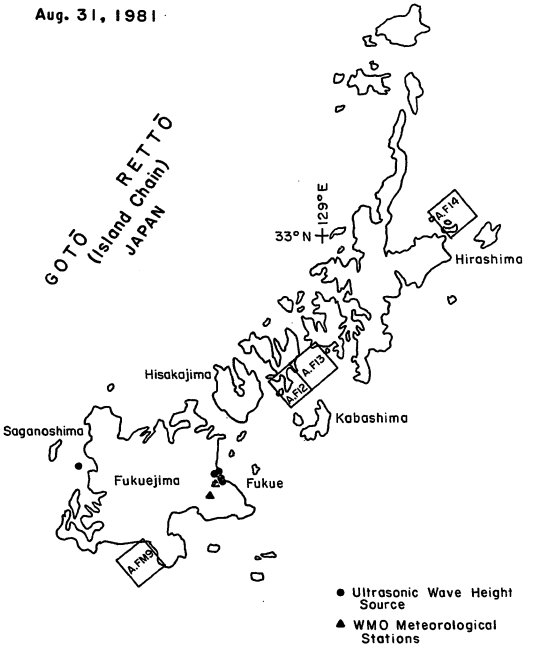

Figure 4-1. Map of the Gotoh Islands showing key scenes for the August 31, 1981 mission.

Reproduced with permission of the copyright owner. Further reproduction prohibited without permission.

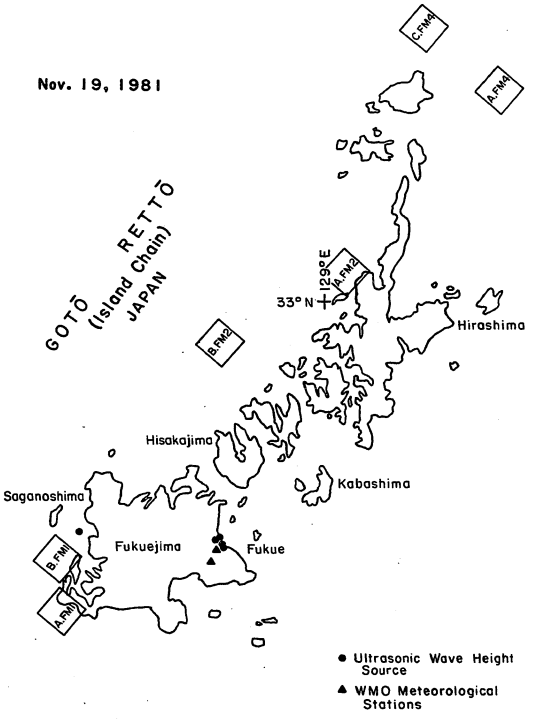

Figure 4-2. Map of the Gotoh Islands showing key scenes for the November 19, 1981 mission.

Reproduced with permission of the copyright owner. Further reproduction prohibited without permission.

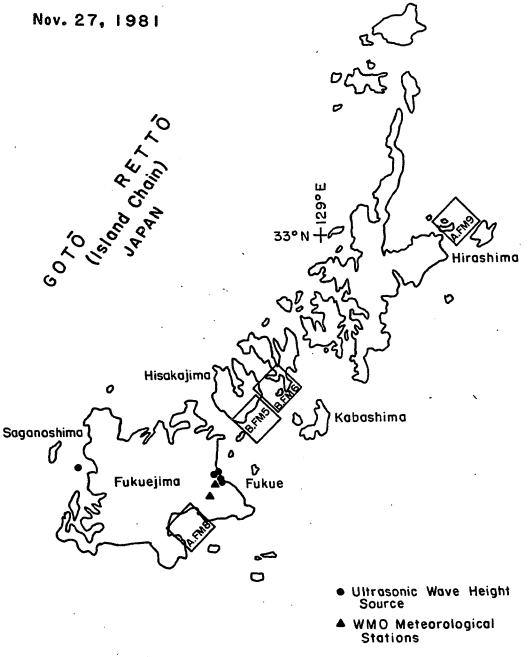

Figure 4-3. Map of the Gotoh Islands showing key scenes for the November 27, 1981 mission.

Reproduced with permission of the copyright owner. Further reproduction prohibited without permission.

A31A.FM9

Apart from being an excellent example of the contrast between open water seas and wavelength filtered, diffracted coastal seas, spectral analysis reveals a wave component not usually perceivable. The seas impinging upon the southern coast of Fukuejima were created by typhoon Agnes, situated at 27 degrees N, 124 degrees E, several hundred uninterrupted nautical miles to the southwest. Three 128 by 128 pixel regions were extracted and Fourier transformed (figure 4-4). The spectra show a fairly wide dispersion of wave energy. In the open water region and just inside the diffraction area, the energy dispersion pattern takes on an inverted, sleeping "S" shape. This signature is less noticeable in the more proctected area. Despite the wide angular dispersion, a single low frequency component is discernible in all three spectra. In the open water, the component is propagating at 354 degrees with a wavelength of 199 m. A bathymetric chart shows the water depth in this region to be around 60 m, so at this point the long wave component has "felt the bottom" and begun to refract toward shore. Storms such as a typhoon generate a full spectrum of ocean wavelengths, but the lower frequency components propagate faster. Such a component is presented here. The significance is not the presence of the component, but its detectability by the SAR. We see more than a simple two scale process where Bragg scatterers are modulated by a single swell component. The modulating is done by a superposition of many components, yet one very long wave component emerges amidst a broad band of frequency returns.

Reproduced with permission of the copyright owner. Further reproduction prohibited without permission.

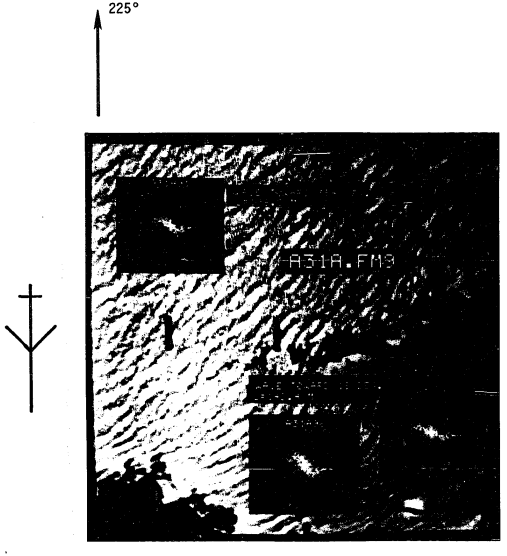

Figure 4-4. Scene A31A.FM9. Note the contrast between the open sea, to the top, and diffracted, long-crested waves between the land masses. The three 128 by 128 pixel areas of spectral analysis are shown, with the low frequency component marked. This is a ground-plane corrected image.

Reproduced with permission of the copyright owner. Further reproduction prohibited without permission.

A31A.F14

Vesecky and Stewart [5] report that SAR imagery has not yet yielded directional wind information, but this scene rebuffs that claim. Three classes of wind features are revealed in the August 31 and November 27 data. This scene contains two of them: wind rows and cat's paws (figure 4-5). This scene, and several that follow, demonstrate a trend in wind patterns. Waters beneath winds uninterrupted by topography have fewer organized Bragg scatterers than those downwind from major topographic features. The World Meterological Organization (WMO) weather station on Fukuejima at the time this scene was imaged reported a wind of 6.8 m/s from the southeast. When corrected for seas at 10 m elevation, the wind speed becomes 9.8 m/s. A ship of opportunity five and one half hours later, 20 nmi northwest of the scene, reported a wind speed of 12.4 m/s from 140 degrees. The wind directions agree. The calm, dark band across the scene is a path of uninterrupted wind flow. The cat's paws above this band result from wind wake behind the visible land mass. The wind rows below the dark band apparently result from winds perturbed by the island of Hirashima, just to the left of the scene. Two 128 by 128 pixel regions and a 64 by 64 pixel region were analyzed (figure 4-6). In addition to two dominant wave spectral components, a directed spread of energy is revealed at 107 degrees in the left-most larger region, and at 112 degrees in the right-most larger region. These correspond to wind row lineations oriented perpendicular to the wind direction, i.e. wind from 197 and 202 degrees. Figure 4-7 is a blow-up of the raw spectrum from the right-most region.

The wind rows highlight wave patterns whose components show up in the spectra. The most dominant wave component in all three regions a-

Reproduced with permission of the copyright owner. Further reproduction prohibited without permission.

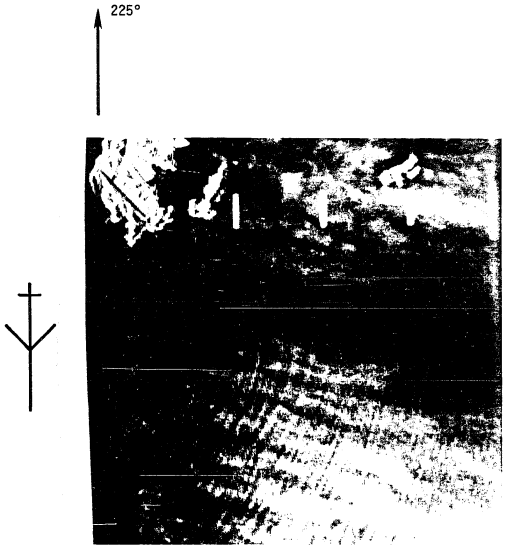

Figure 4-5. Scene A31A.F14. SAR detected wind patterns. Cat's paws appear in the upper portion of the scene, wind rows in the lower portion. This image is in the radar slant-plane.

Reproduced with permission of the copyright owner. Further reproduction prohibited without permission.

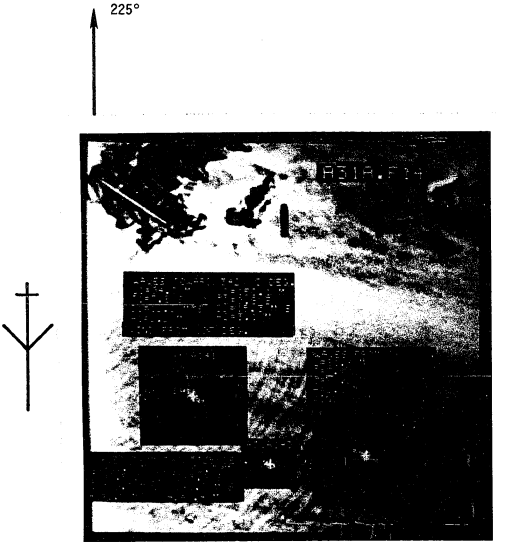

Figure 4-6. Scene A31A.F14 in the ground-plane with regional spectra superimposed. The gray levels are inverted from Figure 4-5.

Reproduced with permission of the copyright owner. Further reproduction prohibited without permission.

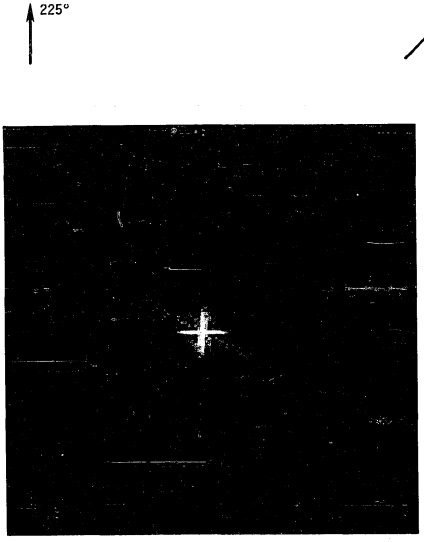

Figure 4-7. Mag. FFT of region A312A142 from scene A31A.F14. Notice the energy spread directed at 112 degrees.

Reproduced with permission of the copyright owner. Further reproduction prohibited without permission.

ligns with the wind direction and corresponds to wavelengths of 81 to 94 m. A less dominant component detected in the left-most larger region has a wavelength and direction similar to the low frequency typhoon component in A31A.FM9, detected at the south end of the Gotohs.

The correspondence between the dominant wave component and the wind direction should make wave parameter estimation reliable. Table I presents the digitally extracted and estimated environmental parameters.

N27A.FM9

Scene N27A.FM9 covers the same area as A31A.F14. Of significance here, again, is wind direction. Here the wind feature class revealed is wind streaks. Wind streaks result from convective vortices, forming lineations more sharply defined than for wind rows (figure 4-8). They are independent of topography. The WMO station on Fukuejima reported a wind speed of 6.4 m/s from the north. When corrected for the sea at 10 m elevation, the wind speed became 9.94 m/s. A ship of opportunity just south of Fukuejima three and one half hours later reported a wind speed of 9.8 m/s from 340 degrees. Four regions were analyzed; three 128 by 128 pixels and one 64 by 64 pixels (figure 4-9). Spectra for the two left-most regions reveal directed energy spreads at 269 and 260 degrees, which correspond to wind from 359 and 350 degrees, respectively. The SAR, WMO and ship reported wind directions agree.

The dominant wave component and the wind direction correspond in all four regions. The tidal station at Hirashima, just to the left of the scene, predicted maximum ebb tide about 15 minutes after the time the scene was imaged. The predicted tidal current was 2.12 knts at 165 degrees. This is roughly in the same direction as the wave field and wind flow. Table II presents the digitally extracted and estimated

Reproduced with permission of the copyright owner. Further reproduction prohibited without permission.

Reproduced with permission of the copyright owner. Further reproduction prohibited without permission.

TABLE I

ENVIRONMENTAL PARAMETERS EXTRACTED FROM SAR IMAGE A31A.F14

Region	L (m)	T_{sig} (sec)	C (m/2)	H_{sig} (m)	θ_{Wave} (deg)	U_* (m/2)	C_{10}	Z_o (cm)	W (ppm)	θ_{Wind} (deg)	U_{10} (m/2)
A31A141	94.93	7.80	12.17	2.24	162	0.349	0.00126	0.029	8680	197	-
A31A142	81.37	7.22	11.27	1.99	162	0.349	0.00126	0.03	8680	202	-
A31A143	88.31	7.52	11.74	2.12	169	0.349	0.00126	0.03	8680	-	-
WMO Station	-	-	-	-	-	-	-	-	-	135	9.8 +
Ultra-sonic wave station	-	9.4	-	1.33	-	-	-	-	-	-	-
Ship.	-	3(wave)	-	2(wave)	30?	-	-	-	-	140	12.4
ZEOH	-	7(swell)	-	3.5(swell)	30?	-	-	-	-	140	12.4

+Corrected for elevation of station and for location on land.
The ultrasonic wave station is on the lee side of the island.

?This reading is suspect.

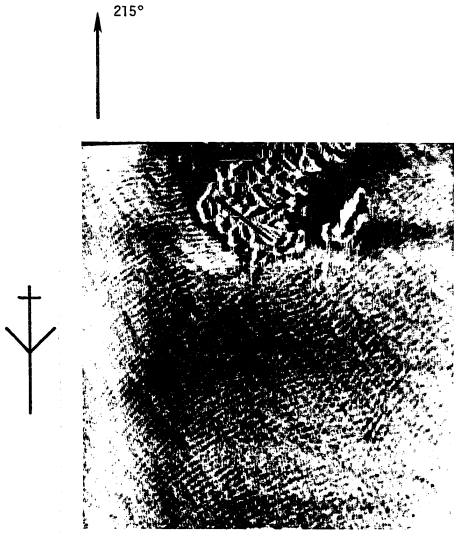

Figure 4-8. Scene N27A.FM9. SAR detected wind streaks and surface waves. This image is in the radar slant-plane.

Reproduced with permission of the copyright owner. Further reproduction prohibited without permission.

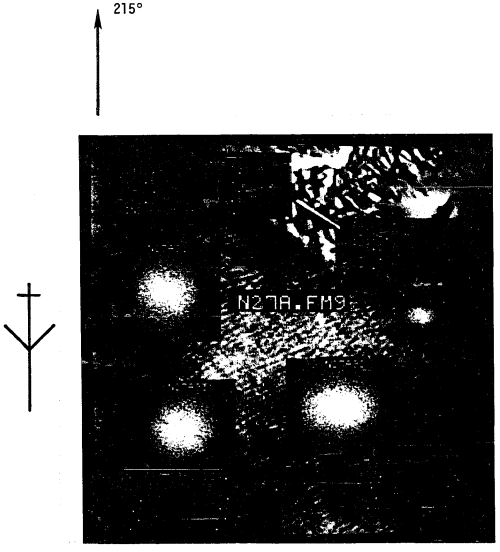

Figure 4-9. Scene N27A.FM9 in the ground-plane with regional spectra superimposed. The gray levels are inverted from Figure 4-8.

Reproduced with permission of the copyright owner. Further reproduction prohibited without permission.

Reproduced with permission of the copyright owner. Further reproduction prohibited without permission.

TABLE II

ENVIRONMENTAL PARAMETERS EXTRACTED FROM SAR IMAGE N27A.FM9

Region	L (m)	T_{sig} (s)	C (m/s)	H_{sig} (m)	θ_{wave} (deg)	U_* (m/s)	C_{10}	Z_o (cm)	W (ppm)	θ_{wind} (deg)	U_{10} (m/s)
N27A91	81.37	7.22	11.27	2.00	9	0.356	0.00128	0.032	9160	359	-
N27A93	83.62	7.32	11.42	2.05	12	0.356	0.00128	0.032	9160	-	-
N27A93	85.67	7.41	11.56	2.09	353	0.356	0.00128	0.031	9160	350	-
N27A94	104.69	8.19	12.78	2.43	25	0.356	0.00128	0.030	9160	-	-
WMO Station	-	-	-	-	-	-	-	-	-	360	9.94+
Ultrasonic Wave Station	-	5.7	-	1.55	-	-	-	-	-	-	-
Ship UJAE	-	4.0?	-	4.0?	-	-	-	-	-	-	-

+Corrected for elevation of station and for location on land.

?This report suspect.

environmental parameters.

Other Wind Pattern Scenes

Four other SAR scenes further substantiate the detection of wind patterns. Scenes N27B.FM6 (figure 4-10), A31A.F12 (Figure 4-11) and N27A.FM9 (figure 4-12) show wind rows resulting from wind wake downwind from topographic features. In N27B.FM6, the wake is produced by small peninsulas protruding into the channel between two of the Gotoh Islands. In A31A.F12, the high return area results from wake downwind from the island of Kabashima, which is situated just to the left of the scene. Scene N27A.FM8 shows wind rows downwind from Fukuejima. The rows align with the wind direction. This is a fetch limited regime, also. The final wind pattern, N27B.FM5, reveals cat's paws downwind from the Gotoh Island of Hisakajima (figure 4-13). The peaks visible to the right rise to approximately 722 m.

Oceanic Fronts

Oceanic fronts are prevalent in the Japanese SAR data. Aside from the current boundary fronts of the Gulf Stream [18], oceanic fronts are noticeably absent from the SAR literature. This may be due to the low resolution of SEASAT data, the longer Bragg wavelengths sensitive to L-band SAR's, and the limited number of environments prone to frontal formation heretofore imaged by aircraft SAR's. The scenes that follow document the detectability of fronts by SAR in the coastal environment. The relative proliferation of oceanic fronts sensed on November 19, as opposed to the November 27 and Augsut 31 missions, alludes to the weather and tidal scenario that encourages surface frontal expression.

November 19 Fronts

The Gotoh Islands were dominated by high pressure throughout

Reproduced with permission of the copyright owner. Further reproduction prohibited without permission.

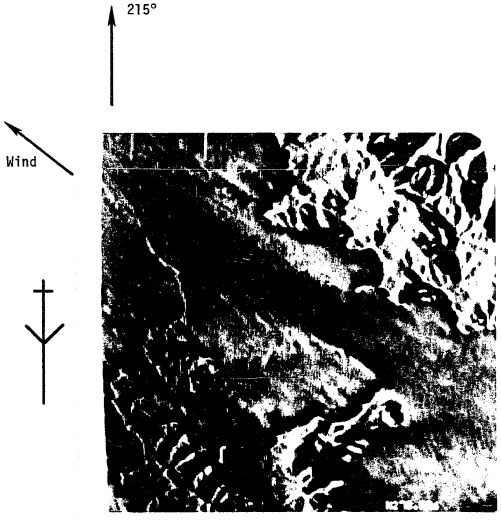

Figure 4-10. Scene N27B.FM6. Increased SAR scattering occurs downwind from topographic features. The dark band through the channel corresponds to unperturbed air and tidal flow. This image is in the radar slant-plane.

Reproduced with permission of the copyright owner. Further reproduction prohibited without permission.

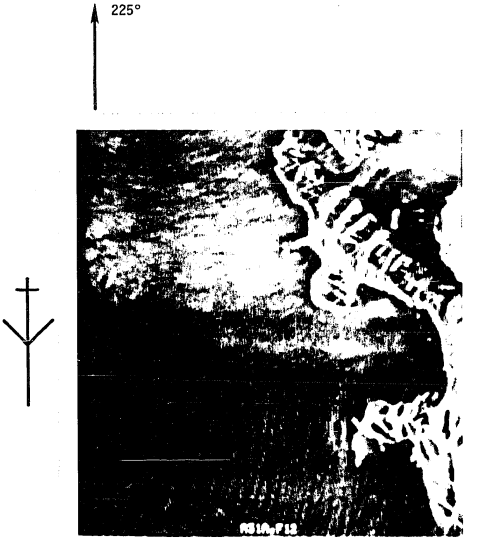

Figure 4-11. Scene A31A.F12. Increased SAR scattering in the upper half of the image is downwind from an island just to the left of the scene. The darker area is where the wind is not obstructed by topography. This image is in the radar slant-plane.

Reproduced with permission of the copyright owner. Further reproduction prohibited without permission.

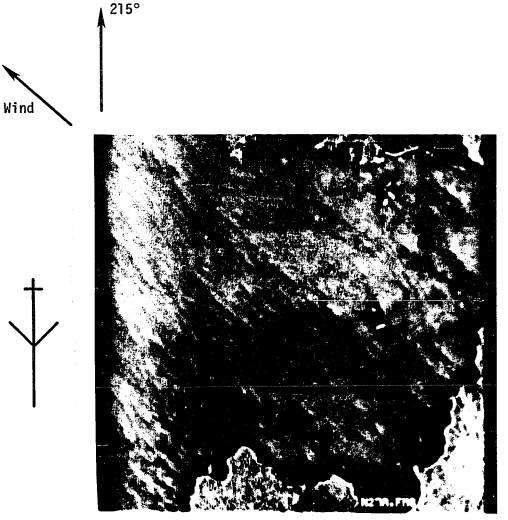

Figure 4-12. Scene N27A.FM8. Wind rows downwind from Fukuejima. Peaks as high as 1407 m exist on Fukuejima, just to the right of the scene. This image is in the radar slant-plane.

Reproduced with permission of the copyright owner. Further reproduction prohibited without permission.

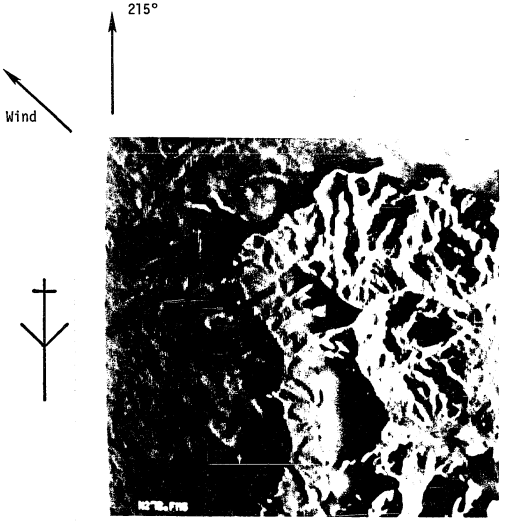

Figure 4-13. Scene N27B.FM5. Cat's paws downwind from Hisakajima. The peaks to the right rise to approximately 722 m. This image is in the radar slant-plane.

Reproduced with permission of the copyright owner. Further reproduction prohibited without permission.

November 19. This was verified by northern hemisphere synoptic weather charts, the WMO station on Fukuejima, and ships of opportunity. Winds were as low as 0.5 m/s, but no higher than 1.54 m/s, well below the threshold of 5 m/s generally assumed necessary for X-band SAR ocean imaging [19] (see table III).

Seas on November 19 were very calm. Wave periods were 1 s and heights 1 m throughout the morning hours. Modulation of what few Bragg scatterers can exist at 1 m/s wind speeds was minimized by these short period, low height waves. Surface wave patterns are absent from the November 19 SAR imagery as expected from the sea state. Air temperatures were about 3 degrees Celsius below sea surface temperatures, implying a moderately stable boundary layer. The waters imaged during this mission were experiencing ebb tide, the tidal current propagating at 165 degrees with an average speed of 1.9 knots. The mission was flown just ahead of slack water time.

Scenes N19A.FM1 and N19B.FM1 display fronts under the influence of the tidal current. In N19A.FM1 (figure 4-14) the frontal boundary is characterized by a different texture to the left than to the right, rather than by a pronounced lineation. The front bulges in the direction of the tidal current. A slight lineation in the more highly textured region just off the small peninsula is oriented in the tidal flow direction and probably represents a small headland shear zone. Wind cannot account for the textural difference across the front. The textured region is probably warmer water than the surrounding waters. This would increase the air-sea temperature difference, and instability would account for an increase in Bragg scatterers. The textured region extends to the right of this scene for more than 7.5 nmi and is about 2 nmi wide. Scene N29B.FM1 (figure 4-15) shows a headland front. The

Reproduced with permission of the copyright owner. Further reproduction prohibited without permission.

TABLE III

ENVIRONMENTAL INFORMATION FOR NOVEMBER 19, 1981, GOTOH ISLANDS

Source	U_{10} (m/2)	θ_{Wind} (deg.)	Sea level Press (mb)	Air. Temp. (^{0}C)	Water Temp. (^{0}C)	T_{sig} (s)	H_{sig} (m)
Fukuejima WMO station @ 0900 hr.	0.59+	360	1024.6	12.8	-	-	-
Ship 9MTU @ 0000 hr.	1.54	230	1024.0	18.0	22.5	1	1
Ship 9MTU @ 0600 hr.	0.51	110	1023.3	19.0	22.0	1	1
Hirashima Tidal Station	Max. ebb tide at 1048 hr., 165 degrees.						

+Corrected for elevation of station and for location on land.

Reproduced with permission of the copyright owner. Further reproduction prohibited without permission.

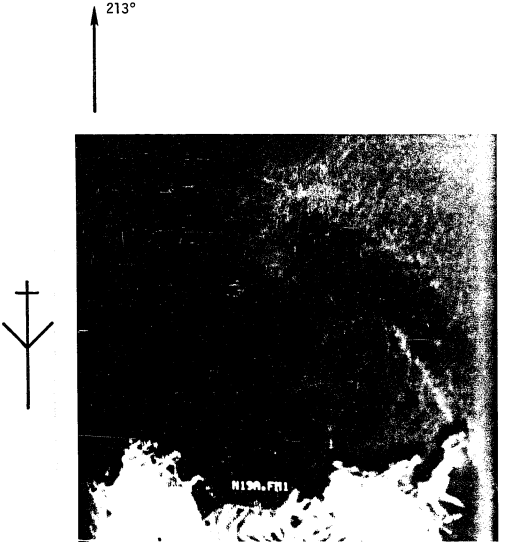

Figure 4-14a. Scene N19A.FM1. The frontal boundary is characterized by a difference in texture. The lineation to the left of the small peninsula is in the direction of the tidal current. This image is in the radar slant-plane.

Reproduced with permission of the copyright owner. Further reproduction prohibited without permission.

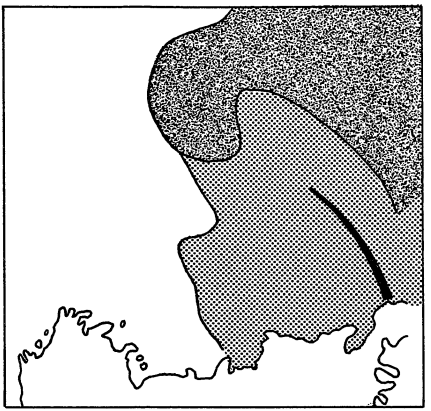

Figure 4-14b. A slant-plane sketch highlighting the textured region and the lineations.

Reproduced with permission of the copyright owner. Further reproduction prohibited without permission.

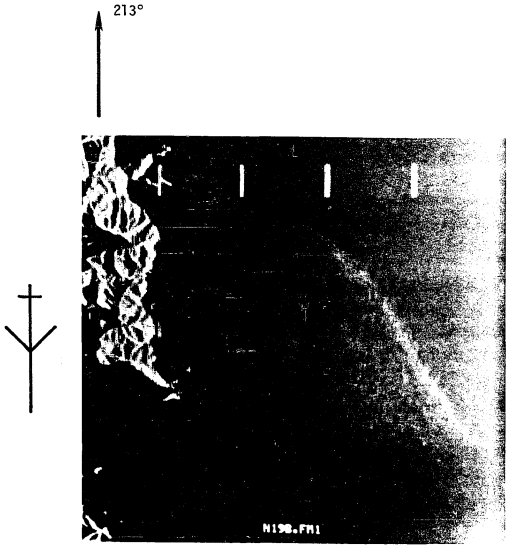

Figure 4-15. Scene N19B.FM1. The headland front is the lineation situated diagonally. It aligns with the tidal current and occurs downstream from Saganoshima. The island is below and to the right of the scene. This image is in the radar slant-plane.

Reproduced with permission of the copyright owner. Further reproduction prohibited without permission.

front is the lineation which trails behind Saganoshima in the direction of the tidal current. Saganoshima is situated below and to the right of this scene.

Scenes N19A.FM2 and N19B.FM2 show two more fronts unique to the data set. N19A.FM2 shows the front as a lineation near shore with no discernible difference in image texture on either side of the front (figure 4-16). N19B.FM2 (figure 4-17) shows a front similar to N19A.FM1 in that it is characterized by a difference in image texture. The dot just inside the textured region is a small boat, probably a fishing boat. The boat is one of over thirty imaged in the area. Although it is difficult to verify in the field correlated SAR imagery, it appears that all but two boats are in a region of slightly more textured water. Wakes of two boats not in the textured waters show them moving toward the textured region. Fishing along thermal fronts is a time honored practice and lends credence to the conjecture that scene N19B.FM2 shows a thermal front.

This scene shows a front differing from those of November 19, since it results from the interaction of a wind driven wave field moving toward the top of the image, and a 3.1 knt tidal current propagating toward the bottom of the image, having passed through a narrow channel. Shear zones generate a high population of Bragg scatterers that express the front in the SAR image. The front is more than a SAR peculiarity since the incoming wave field is refracted to the right of the front (figure 4-18).

Internal Waves

Internal waves are not unique to SAR imagery [20,21], but are peculiar in this data set. Scene N19A.FM4 (figure 4-19) shows the only

Reproduced with permission of the copyright owner. Further reproduction prohibited without permission.

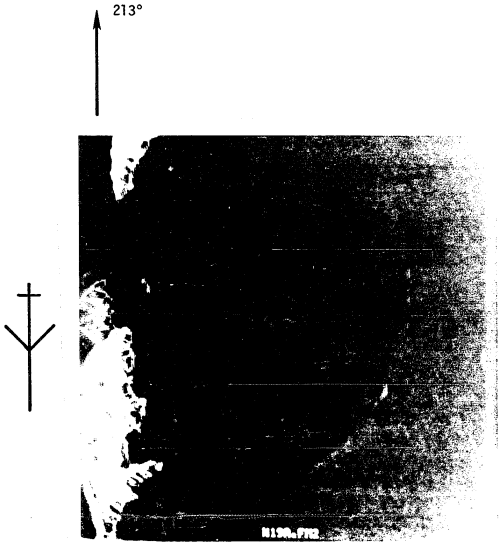

Figure 4-16. Scene N19A.FM2. This front is expressed as a lineation, with no variation in image texture across the front. This image is in the radar slant-plane.

Reproduced with permission of the copyright owner. Further reproduction prohibited without permission.

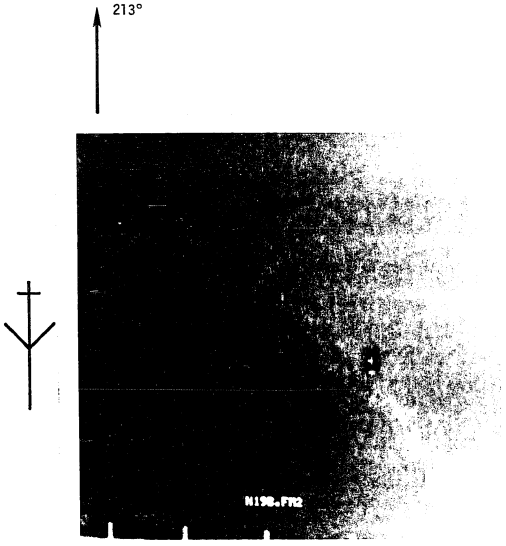

Figure 4-17. Scene N19B.FM2. Another front characterized by textural differences in water masses. This image is in the radar slant-plane.

Reproduced with permission of the copyright owner. Further reproduction prohibited without permission.

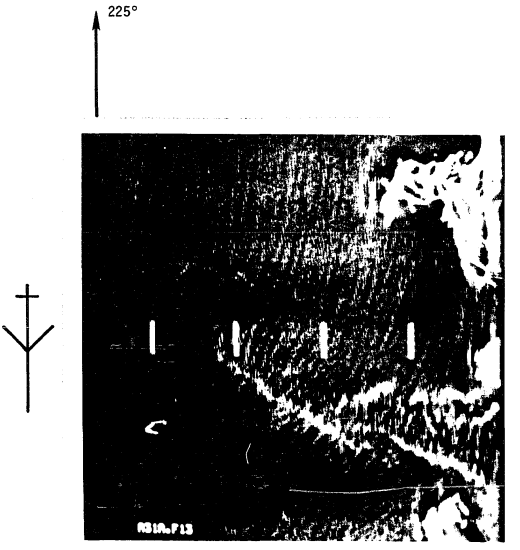

Figure 4-18. Scene A31A.F13. The tidal current is downward, while the wave field propagates upward in the scene. This image is in the radar slant-plane.

Reproduced with permission of the copyright owner. Further reproduction prohibited without permission.

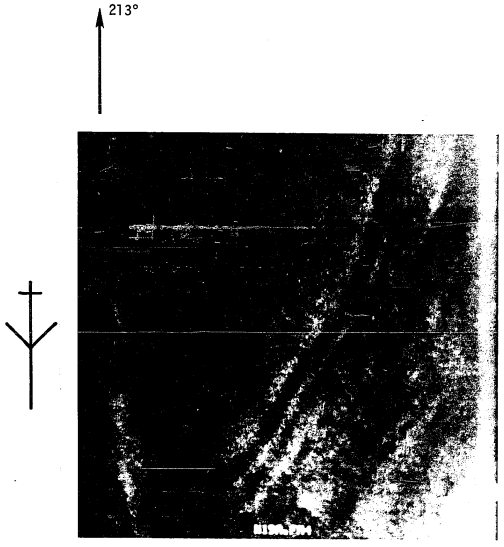

Figure 4-19. Scene N19A.FM4. An internal wave pattern north of the Gotoh Islands. This image is in the radar slant-plane.

Reproduced with permission of the copyright owner. Further reproduction prohibited without permission.

internal wave pattern in the Japanese data. It is located just north of the Gotoh Islands, well away from sources of fresh water runoff. Equally interesting is scene N19C.FM4 (figure 4-20), situated about 5 nmi west and slightly north of N19A.FM4. Scene N19C.FM4 was initially speculated to be a rainfall pattern. Were it so, this might be a more bouyant fresh water source for internal waves induced by the underlying swell. It is unlikely, though, that showers would be present in an area dominated by a 1024 mb atmospheric high, despite a reported cloud cover of 7/10. The WMO weather station on Fukuejima reported no rainfall for this day.

Reproduced with permission of the copyright owner. Further reproduction prohibited without permission.

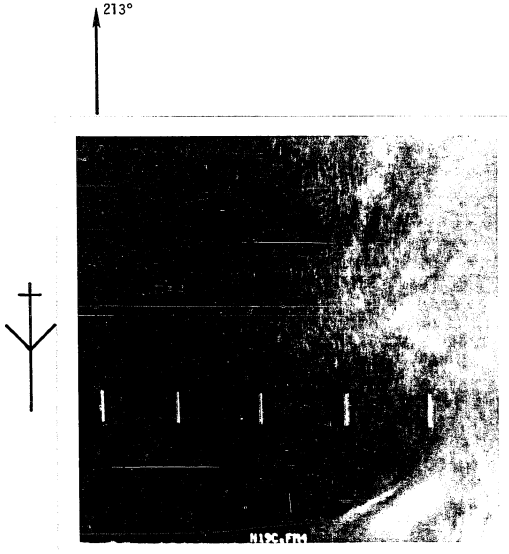

Figure 4-20. Scene N19C.FM4. This unknown surface disturbance was speculated to be rainfall, but it is not likely to be so in an area dominated by high pressure.

Reproduced with permission of the copyright owner. Further reproduction prohibited without permission.

REFERENCES

1. Mattie, M.G., S.V. Hsiao, D.D. Evans, "Wave Direction Measured by Four Different Systems," IEEE J. Oceanic Engineering , Vol. OE-6, No. 3 (July 1978), pp. 87-93.

2. Meadows, G.A., E.S. Kasischke, R.A. Shuchman, "SAR Observations of Coastal Zone Conditions," Proc. 14th Intl. Symp. Remote Sensing Environ., Vol. 2 (Ann Arbor, MI.: ERIM, April 1980), pp. 845-863.

3. Hayes, J.G. and R.A. Shuchman, "SEASAT SAR Ocean Surface Current and Shallow Water Wave Refraction," in Oceanography From Space., J.F.R. Gower, ed., New York, N.Y.: Plenum, 1981, pp. 469-476.

4. Shuchman, R.A., J.D. Lyden, D.R. Lyzenga, "Estimates of Ocean Wavelength and Direction From X- and L- Band Synthetic Aperture Radar Data Collected During the Marineland Experiment," IEEE J. Oceanic Engineering , Vol. OE-8, No. 2 (April 1983), pp. 90-96.

5. Vesecky, J.F. and R.H. Stewart, "The Observation of Ocean Surface Phenomena Using Imagery From the SEASAT Synthetic Aperture Radar: An Assessment," J. Geophys. Research , Vol. 87, No. C5 (April 1982), pp. 3397-3430.

6. Jain, A. "Determination of Ocean Wave Heights from Synthetic Aperture Radar Imagery," Applied Physics , Vol. 13 (1977), pp. 371-382.

7. Harger, R.O., "A Sea Surface Height Estimator Using Synthetic Aperture Radar Complex Imagery," IEEE J. Oceanic Engineering , Vol. OE-8, No. 2 (April 1983), pp. 71-78.

8. U.S. Army Coastal Engineering Research Center Shore Protection Manual : Vol. I. Dept. Army Corps of Engineers, 1977, section 3.51.

9. Hasselmann, K. et.al., "Measurements of Wind-Wave Growth and Swell Decay During the Joint North Sea Wave Project (JONSWAP)," Dtsch. Hydrogr. Z., Erganzungsheft Reihe A., , Vol. 12 (1973), p. 95.

10. Hess, S., Introduction To Theoretical Metheorology , New York, N.Y.: Holt, Rinehart and Winston, 1959, p. 362.

11. Blackadar, A.K., "A Survey of Wind Characteristics Below 1500 Ft.," in Meteorological Monography , Vol. 4, No. 22 (May 1960), pp. 3-11.

12. Hsu, S.A., "Models for Estimating Offshore Winds From Onshore Meteorological Measurements," Boundary-Layer Meterology , Vol. 20 (1980), pp. 341-351.

Reproduced with permission of the copyright owner. Further reproduction prohibited without permission.

13. Amorocho, J. and J. DeVries, "Wind Stress over Water," J. Geophys. Research , Vol. 85, No. C1 (Jan. 1980), pp. 433-442.

14. Hsu, S.A., "A Dynamic Roughness Equation and Its Application to Wind Stress Determination at the Air-Sea Interface," J. Geophys. Research , Vol. 4, (Jan. 1974), pp. 116-120.

15. Wu, J., "Oceanic Whitecaps and Sea State," J. Geophys. Research, Vol. 9 (Sept. 1980), pp. 1064-1068.

16. Wu, J., "Spray in the Atmospheric Surface Layer: Laboratory Study," J. Geophys. Research , Vol. 78, No. 3 (Jan. 1973), pp. 511-519.

17. Wu, J., "Sea Spray: A Further Look," J. Geophys. Research , Vol. 87, C11 (Oct. 1982), pp. 8905-8912.

18. Hayes, R.M., "Detection of the Gulf Stream," in Spaceborne Synthetic Aperture Radar For Oceanography , Baltimore, MD.: Johns Hopkins Univ. Press, 1981, pp. 146-160.

19. Shuchman, R.A., Personal communication.

20. Trask, R.P., and M.G. Briscoe, "Detection of Massachusetts Bay Internal Waves by the Synthetic Aperture Radar on SEASAT," J. Geophys. Research , Vol. 88, No. C3 (Feb. 1983), pp. 1789-1799.

21. Hughes, B.A. and J.F.R. Gower, "SAR Imagery and Surface Truth Comparisons of Internal Waves in Georgia Strait, British Columbia, Canada," J. Geophys. Research , Vol. 88, No. C3 (Feb. 1983), pp. 1809-1824.

Reproduced with permission of the copyright owner. Further reproduction prohibited without permission.

CHAPTER 5

SAR TEXTURE ANALYSIS:

THE DIGITAL IMAGE ANALYSIS PERSPECTIVE

An image transformation that provides more information than the power spectrum is of interest in SAR ocean image feature extraction and characterization. Texture analysis based on gray level co-occurrence (GLC) matrices is an alternative. An image classification experiment conducted by Conners and Harlow [1] which compared the GLC, gray level run length (GLRL), and power spectral (PS) methods, showed the GLC method to be more powerful than the GLRL or PS methods at discriminating Markov textures. The implication is that the GLC matrices contain more textural information than the power spectrum. Appropriately defined measures for the GLC matrices should be able to characterize more image features than the PS method.

This chapter presents a study of periodicity characterization by the GLC method. If the GLC method is to be applicable to SAR ocean wave analysis, it must first be shown to measure wave direction and length. The PS method does this well. This study demonstrates theoretically and experimentally that the GLC method also measures wave direction and length. Computer synthesized wave imagery is used to show that the GLC matrices retain phase information that is sensitive to a measure called cluster shade. This is a new discovery and contributes to our understanding of why the GLC method is a more powerful

Reproduced with permission of the copyright owner. Further reproduction prohibited without permission.

textural discriminator than the PS method. The study is concluded by applying GLC matrix measures to several SAR ocean image wind patterns to assess their utility on roughly periodic and non-periodic patterns.

5.1 The GLC Matrices and Measures

The GLC matrix is essentially an image compression representation. A matrix is generated for each pixel spacing, d, and angle, θ, within the scene. The matrix is square and has as many rows and columns as gray levels in the image. Each GLC matrix element is the probability of going from one gray level, call it "i", to another gray level, "j", given an angle, θ, and an intersample spacing, d, i.e., $S_\theta(i,j|d)$. Obviously, one can easily generate more data than is in the original image if all d's, θ's and all 256 gray levels are considered. Most visually distinct image structures are retained when the image is reduced to 16 gray levels. In this study, equal probability quantization (EPQ) to 16 gray levels was done. EPQ has the advantage of normalizing image contrast differences among scenes due to film processing and digitization [2]. Based on image resolution and knowledge of limiting sizes of features, reasonable values of d may be determined. The same kind of "scene knowledge" can be used to pick reasonable values of θ. With these considerations, GLC matrices do become image compression representations. Figure 5-1 shows the configuration of a GLC matrix representing NG gray levels.

Textural information is extracted from GLC matrices by measures. Six measures were used in this study. They are:

Reproduced with permission of the copyright owner. Further reproduction prohibited without permission.

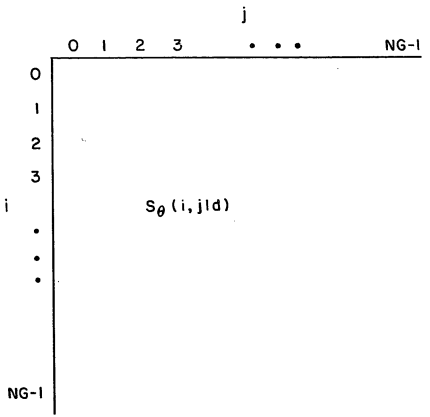

Figure 5-1. The gray level co-occurrence matrix. Each element is the probability of going from gray level i to gray level j, given a direction, θ, and an intersample spacing, d.

Reproduced with permission of the copyright owner. Further reproduction prohibited without permission.

1. Inertia

$$\sum_{i=0}^{NG-1} \sum_{j=0}^{NG-1} (i-j)^2 \; S_\theta(i,j|d) \tag{5-1}$$

2. Energy

$$\sum_{i=0}^{NG-1} \sum_{j=0}^{NG-1} [S_\theta(i,j|d)]^2 \tag{5-2}$$

3. Entropy

$$\sum_{i=0}^{NG-1} \sum_{j=0}^{NG-1} S_\theta(i,j|d) \log S_\theta(i,j|d) \tag{5-3}$$

4. Local Homogeneity

$$\sum_{i=0}^{NG-1} \sum_{j=0}^{NG-1} S_\theta(i,j|d)/(i-j)^2 \tag{5-4}$$

5. Cluster Shade

$$\sum_{i=0}^{NG-1} \sum_{j=0}^{NG-1} (i + j - \mu_x - \mu_y)^3 \; S_\theta(i,j|d) \tag{5-5}$$

6. Cluster Prominence

$$\sum_{i=0}^{NG-1} \sum_{j=0}^{NG-1} (i + j - \mu_x - \mu_y)^4 \; S_\theta(i,j|d) \tag{5-6}$$

where

$$\mu_x = \sum_{i=0}^{NG-1} i \sum_{j=0}^{NG-1} S_\theta(i,j|d) \tag{5-7}$$

Reproduced with permission of the copyright owner. Further reproduction prohibited without permission.

$$\mu_y = \sum_{i=0}^{NG-1} j \sum_{j=0}^{NG-1} S_\theta(i,j|d) \qquad (5\text{-}8)$$

The first four measures are heuristic. They were suggested by Haralick, et.al. [3,4] to measure "... the presence of organized structure within the image," although he notes, "... it is hard to identify which specific textural characteristic is represented by each of these features." The last two measures were suggested by Conners in a paper by Harlow, et.al. [5] and are based upon principles of uniformity and proximity documented by Julesz [6]. If a texture is characterized by a uniformity in gray shade, then higher probabilities will occur in clusters along the main GLC matrix diagonal. Cluster shade and cluster prominence essentially measure the location of uniformity clusters along the matrix diagonal with respect to the means, μ_x and μ_y.

5.2 The Inertia Measure and Wave Period

Periodicity detection is not limited to the power spectrum, but can be done with the inertia measure. This was originally demonstrated by Conners and Harlow [7] when analyzing Brodatz textures [8]. In this section, the inertia measure is analyzed, and four of its characteristics developed and verified. These are:

1. Its ability to detect the period of a simple sinusoidal wave image,
2. Its ability to detect the period of a fundamental frequency and its harmonics,
3. Its insensitivity to relative phase shifts between a fundamental and a harmonic,
4. The relationship between the inertia measure and the auto-

Reproduced with permission of the copyright owner. Further reproduction prohibited without permission.

correlation function.

Following the theoretical developments and verification by computer synthesized wave patterns, the inertia measure shall be applied to SAR ocean imagery. Period detection by the inertia measure shall be compared to that from the power spectrum.

5.2.1 Theoretical Developments of the Inertia Measure

One can easily show that the local minima in the texture measures computed for many d's at a given θ in a sinusoidal image occur at pixel spacings corresponding to the wave period. We start by considering a single sinusoid and sample two points, one at position t and the other offset by some d at the point t_1.

$$f(t) = [\sin \frac{2\pi t}{T} - \sin \frac{2\pi(t-t_1)}{T}]^2 \qquad (5\text{-}9)$$

Remember that the coefficient of the inertia measure has the form $(i-j)^2$, where i and j are gray levels. Likewise, equation (5-9) represents a gray level difference for a given d, where $d=t_1 - t$. Using a trigonometric expansion, equation (5-9) can be rewritten,

$$f(t) = 2 \cos^2 (\frac{\pi(2t-t_1)}{T}) \sin^2 (\frac{\pi t_1}{T}) \qquad (5\text{-}10)$$

where T is the period of the sinusoid. Now we integrate for a large number of periods in the image, neglecting image boundary effects.

$$I = \int_a^b f(t)dt = 2 \sin^2 (\frac{\pi t_1}{T}) \int_a^b \cos^2 (\frac{\pi(2t - t_1)}{T}) dt \qquad (5\text{-}11)$$

The term in the integral can be expanded as,

$$\cos^2 (\frac{\pi(2t-t_1)}{T}) = \cos^2 (\frac{2\pi t}{T} - \frac{\pi t_1}{T}). \qquad (5\text{-}12)$$

Reproduced with permission of the copyright owner. Further reproduction prohibited without permission.

We are integrating over t, and t_1 is a constant, so upon expansion by the trigonometric relation and squaring, we get

$$I = 2 \sin^2 \left(\frac{\pi t_1}{T}\right) \left\{ \int_a^b c_1^2 \cos^2 \left(\frac{2\pi t}{T}\right) dt \right.$$

$$\left. + 2 \int_a^b c_1 c_2 \cos \left(\frac{2\pi t}{T}\right) \sin \left(\frac{2\pi t}{T}\right) dt + \int_a^b c_2 \sin^2 \left(\frac{2\pi t}{T}\right) dt \right\} \qquad (5\text{-}13)$$

where

$$c_1 = \cos \left(\frac{\pi t_1}{T}\right) \qquad \text{and} \qquad c_2 = \sin \left(\frac{\pi t_1}{T}\right) \qquad (5\text{-}14)$$

When solving the integral, we obtain two terms containing $\sin [(4\pi t)/T]$ and one term containing $\sin^2 [(2\pi t)/T]$. When b-a is much greater than T, the terms reduce to zero and a constant, respectively. Therefore, equation (5-13) reduces to

$$I = K \sin^2 \left(\frac{\pi t_1}{T}\right) \qquad (5\text{-}15)$$

where K is a scale constant. $\sin^2 x$ is minimized for $x = n\pi$, $n = 0, \pm 1, \pm 2, \ldots$ Therefore,

$$t_1 = nT \qquad (5\text{-}16)$$

corresponds to the mimimum of the inertia measure. This occurs for intersample spacings corresponding to the wave period.

The same basic development can be used to show that the period of the fundamental and harmonics can be detected by the inertia measure. Furthermore, the fundamental and harmonics need not be in phase with each other. The superposition of the fundamental and harmonics yields a modified version of equation (5-7).

Reproduced with permission of the copyright owner. Further reproduction prohibited without permission.

$$f(t) = \left\{ \sum_{m=1}^{k} [\sin(\frac{2\pi mt}{T} - \phi_m) - \sin(\frac{2\pi m(t-t_1)}{T} - \phi_m)] \right\}^2 \qquad (5\text{-}17)$$

The sin(ax + b) terms in equation (5-17) can be expanded and rearranged so that the expression for integrating over a large number of periods in the image has the form

$$I = \int_a^b f(t)dt = \sum_{m=1}^{k} \sin^2(\frac{m\pi t_1}{T}) \int_a^b \sin^2(\frac{m\pi(2t-t_1)}{T} + 2\phi_m)\, dt. \qquad (5\text{-}18)$$

In a manner similar to the case of the single sinusoidal image, the integral reduces to [9],

$$I = \sum_{m=1}^{k} K \sin^2(\frac{m\pi t_1}{T}). \qquad (5\text{-}19)$$

The $\sin^2 x$ term is minimized whenever

$$t_1 = \frac{nT}{m} = n'T; \qquad n=0,\pm1,\pm2,\ldots,m=0,\pm1,\pm2,\ldots \qquad (5\text{-}20)$$

Whenever n is an integer multiple of m, we have an absolute minimum. This occurs for intersample spacings corresponding to the fundamental frequency, regardless of phase. Local minima occur for rational values of n'. These occur at intersample spacings corresponding to the harmonics.

Finally, let's see how to prove that the inertia measure is essentially the DC biased and scaled autocorrelation function. Let's begin by restating the inertia measure.

$$I(d) = \sum_{i=0}^{NG-1} \sum_{j=0}^{NG-1} (i-j)^2 S_\theta(i,j|d) \qquad (5\text{-}1)$$

Since we are analyzing a large scene, we are interested in the expected value of the inertia measure.

Reproduced with permission of the copyright owner. Further reproduction prohibited without permission.

$$E\{I(d)\} = E\left\{\left|\sum_{i=0}^{NG-1}\sum_{j=0}^{NG-1}(i-j)^2\, S_\theta(i,j|d)\right|\right\} \tag{5-21}$$

$$= \sum_{i=0}^{NG-1}\sum_{j=0}^{NG-1}(i-j)^2\, E\{S_\theta(i,j|d)\} \tag{5-22}$$

Assuming stationarity and an ergodic random process,

$$E\{S_\theta(i,j|d)\} = P(X(t) = i,\ X(t+d) = j) \tag{5-23}$$

where $P(\cdot)$ is the joint probability of a random variable, X, at location t having gray level i, and X displaced from t by d having a gray level j. Upon substituting equation (5-23) into (5-22) and expanding the polynomial,

$$E\{I(d)\} = \sum_{i=0}^{NG-1}\sum_{j=0}^{NG-1} i^2 P(\cdot) + \sum_{i=0}^{NG-1}\sum_{j=0}^{NG-1} j^2\, P(\cdot)$$

$$- 2\sum_{i=0}^{NG-1}\sum_{j=0}^{NG-1} ijP(\cdot) \tag{5-24}$$

$$= 2\sum_{i=0}^{NG-1}\sum_{j=0}^{NG-1} i^2\, P(\cdot) + 2\sum_{i=0}^{NG-1}\sum_{j=0}^{NG-1} ijP(\cdot) \tag{5-25}$$

$$= 2\,(\sigma^2 + \mu^2) - 2R(d) \tag{5-26}$$

where σ^2 is the variance, μ is the mean, and R(d) is the autocorrelation function. The importance of this result is that the power spectrum is the Fourier transform of the autocorrelation function. Therefore, the inertia measure and the power spectrum are equally sensitive to image periodicities.

5.2.2 Empirical Verification

Three computer synthesized wave images and a SAR ocean wave image are processed here to verify the theoretical developments. The first

Reproduced with permission of the copyright owner. Further reproduction prohibited without permission.

two images, figures 5-2 and 5-3, are synthesized images containing a fundamental and one harmonic. Figure 2 was generated from the equation,

$$\zeta(x,y) = a \sin(10X) + a \sin(20X), \tag{5-27}$$

the fundamental making 10 undulations over the 256 pixel wide image. Figure 5-3 was generated from the equation,

$$\zeta(x,y) = a \sin(10X) + a \sin(30X). \tag{5-28}$$

The third image, figure 5-4 was generated with a 60 degree phase shift in the harmonic. Its equation is,

$$\zeta(x,y) = a \sin(10X) + a \sin(20X + \frac{2\pi}{3}). \tag{5-29}$$

A 128 by 128 pixel window was extracted from each image for processing. First, a two-dimensional fast Fourier transform (FFT) was computed on each window. The data were processed first to remove the DC bias and to cosine roll-off 10 percent of the picture near the edges (akin to Hanning windowing), then transformed. Figures 5-5, 5-6 and 5-7 are the FFT magnitudes computed on figures 5-2, 5-3 and 5-4, respectively. The fundamental frequency corresponds to a spatial period in each image of 25.6 pixels. In figures 5-2 and 5-4, the harmonics have a spatial period of 12.8 pixels. In figure 5-3, the harmonic period is 8.5 pixels. Each 128 by 128 pixel window was then processed to extract the inertia measure. No DC bias removal or edge rolling-off was done here. Each window was EPQ reduced to 16 gray levels. GLC matrices for 64 d-θ pairs were computed; θ at 0 degrees and d from 1 to 64 pixels. Inertia was then plotted for all 64 intersample spacings. Figures 5-8, 5-9 and 5-10 show the inertia plots. In figure 5-8, the absolute minimum occurs

Reproduced with permission of the copyright owner. Further reproduction prohibited without permission.

Figure 5-2. A computer synthesized wave image consisting of a fundamental and the second harmonic, both in phase.

Reproduced with permission of the copyright owner. Further reproduction prohibited without permission.

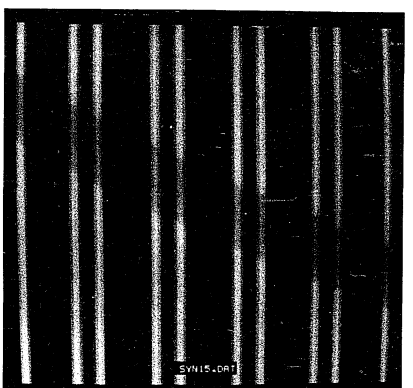

Figure 5-3. A computer synthesized wave image consisting of a fundamental and the third harmonic, both in phase.

Reproduced with permission of the copyright owner. Further reproduction prohibited without permission.

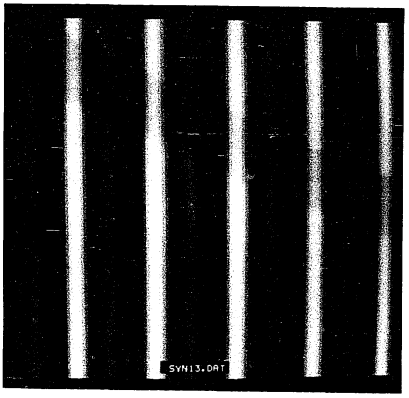

Figure 5-4. A computer synthesized wave image consisting of a fundamental and the second harmonic, the harmonic being out of phase by -60 degrees.

Reproduced with permission of the copyright owner. Further reproduction prohibited without permission.

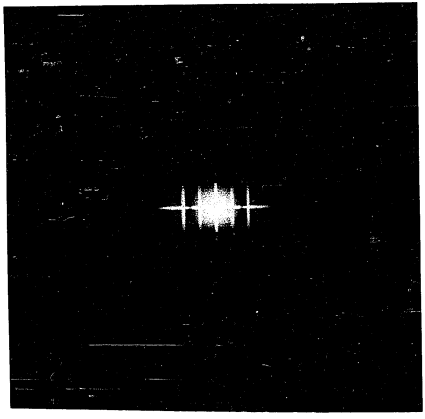

Figure 5-5. The two-dimensional FFT magnitude of the computer synthesized image in Figure 5-2. Note the fundamental and its second harmonic.

Reproduced with permission of the copyright owner. Further reproduction prohibited without permission.

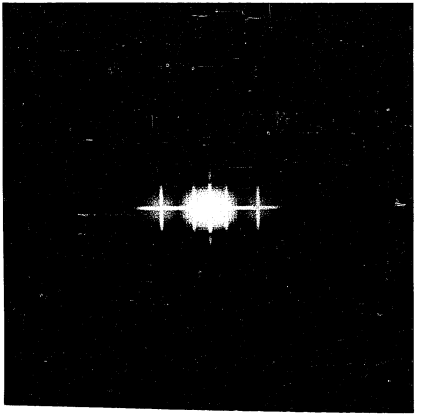

Figure 5-6. The two dimensional FFT magnitude of the computer synthesized image in Figure 5-3. Note the fundamental and its third harmonic.

Reproduced with permission of the copyright owner. Further reproduction prohibited without permission.

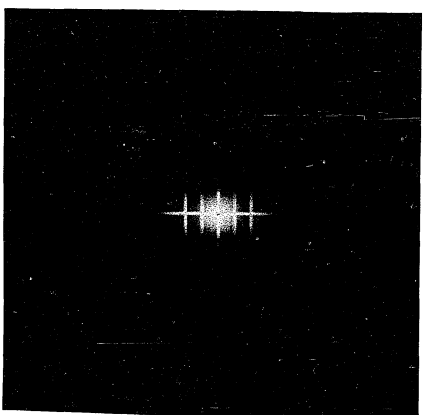

Figure 5-7. The two-dimensional FFT magnitude of the computer synthized image in Figure 5-4. Note the fundamental and its second harmonic.

Reproduced with permission of the copyright owner. Further reproduction prohibited without permission.

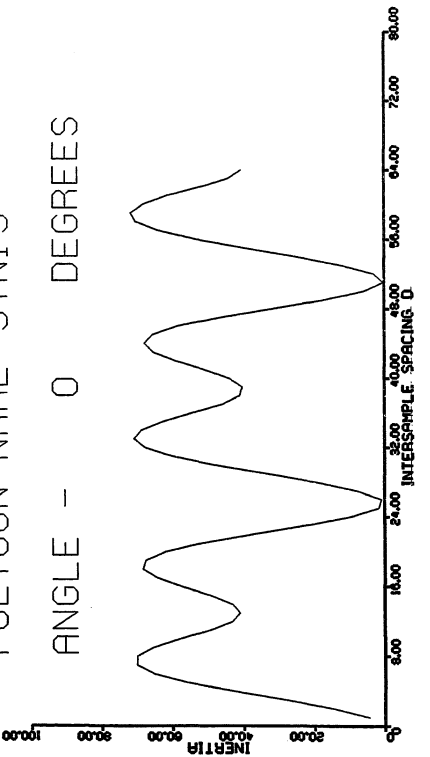

Figure 5-8. The inertia plot of the computer synthesized image in Figure 5-2.

Reproduced with permission of the copyright owner. Further reproduction prohibited without permission.

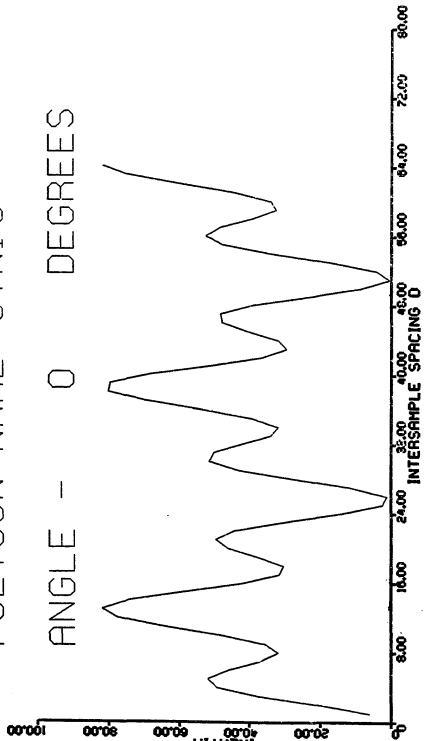

Figure 5-9. The inertia plot of the computer synthesized image in Figure 5-3.

Reproduced with permission of the copyright owner. Further reproduction prohibited without permission.

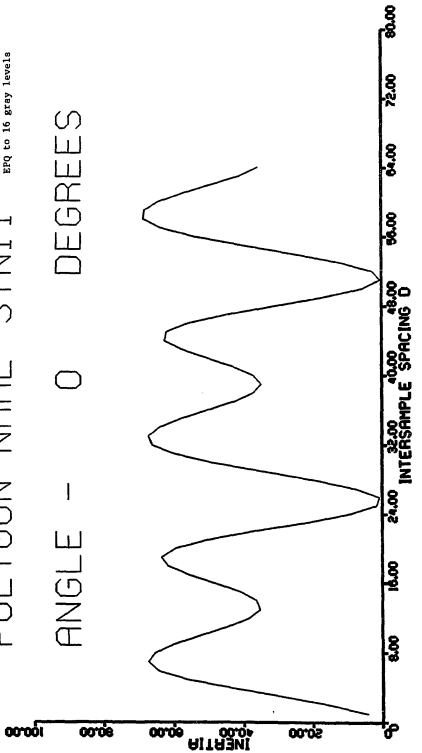

Figure 5-10. The inertia plot of the computer synthesized image in Figure 5-4.

Reproduced with permission of the copyright owner. Further reproduction prohibited without permission.

every 26 pixels, corresponding to the fundamental frequency of 25.6 pixels. The same is true in figures 5-9 and 5-10. In both figures 5-8 and 5-10, the harmonic having a period of 13 pixels is evident. Note that the phase shift of the harmonic is not evident when comparing figures 5-8 and 5-10. Although not shown here, the phase of the FFT for the inertia measure plotted in figures 5-8 and 5-10 does not differ. Finally, figure 5-9 shows the harmonic having a period of 8 pixels, as found in the FFT magnitude.

A similar analysis was done with a SAR ocean image showing long-crested, range traveling waves. The image was taken from the Japanese data set, south of the largest of the Gotoh Islands, Fukuejima. Figure 5-11 shows the ground-plane image with three regions for processing. The largest region, N27C51, is 128 by 128 pixels. The FFT magnitude of this region, after EPQ to 16 gray levels, is shown in figure 5-12. The conjugate pair energy clusters are at a frequency corresponding to a wave period of 7.98 pixels. Figure 5-13 shows the inertia plot computed across the wave crests. The absolute minimum occurs between 7 and 8 pixels. This agrees well with the power spectral result.

5.2.3 Summary of the Wave Periodicity Study

The sensitivity of the inertia measure to wave periodicities reported by Conners and Harlow [7] has been verified. Their work has been extended by this author to show, mathematically and empirically, that the period of harmonics is also detected by the inertia measure and is insensitive to phase. The latter two points are a unique contribution to the understanding of periodicity detection with the inertia measure. This knowledge has been applied to SAR image parameter extraction.

Reproduced with permission of the copyright owner. Further reproduction prohibited without permission.

Figure 5-11. Ground-plane SAR image N27C.FM5 showing long-crested range traveling waves. Region N27C51 is the area analyzed.

Reproduced with permission of the copyright owner. Further reproduction prohibited without permission.

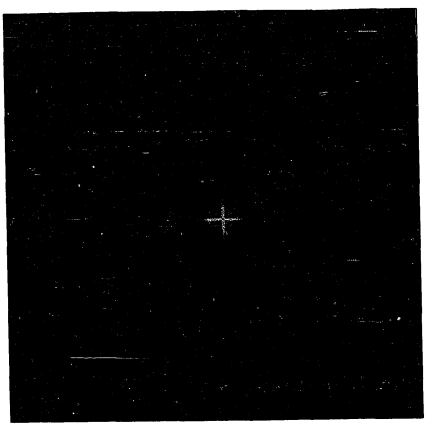

Figure 5-12. The two-dimensional FFT magnitude of the region N27C51 of Figure 5-11. The region was EPQ gray level reduced to 16 levels and the edges cosine weighted before transforming.

Reproduced with permission of the copyright owner. Further reproduction prohibited without permission.

Reproduced with permission of the copyright owner. Further reproduction prohibited without permission.

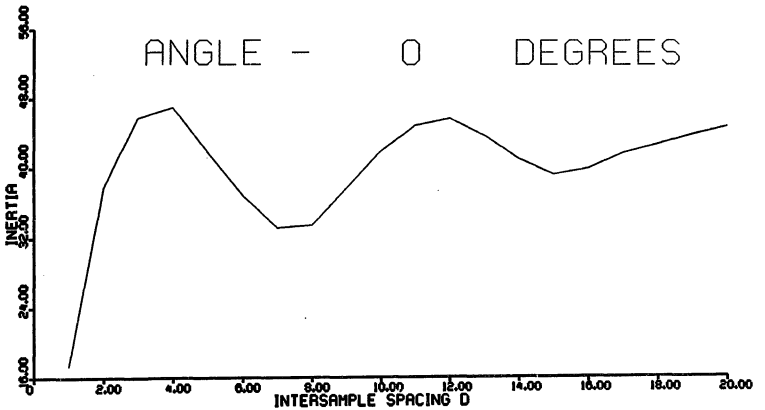

Figure 5-13. The inertia plot for θ across the wave crest. The minimum between 7 and 8 pixels corresponds to the wave length.

5.3 The Inertia Measure and Wave Direction

The inertia measure can be used to determine wave direction. If the image being analyzed is perfectly periodic, and θ is chosen perpendicular to the wave crests, then whenever d = T, the inertia measure will be zero. As θ departs from its position perpendicular to the wave crests, the intersample spacing needed for the inertia measure to become zero increases. Hence, the smallest d for which the inertia measure is a local minimum will always occur when θ is perpendicular to the wave crests.

As an example, consider an image composed of a single sinusoid, having a period of 6.4 pixels propagating horizontally. Four directions shall be analyzed, θ = 0, 45, 90 and 135 degrees. These angles are measured in the trigonometric sense, with 0 degrees being across the wave crests. For each θ, the inertia measure for d's from 1 to 20 pixels are calculated and plotted. Figure 5-14a shows the plot for θ at 0 degrees. The plot shows the wave pattern to have a period of 6 pixels, allowing for quantization to the nearest d. Figure 5-14b shows the inertia plot for θ at 45 degrees. This plot is identical to that for θ at 0 degrees, however, absolute distances measured across pixels at 45 degrees are greater than at 0 degrees by the square root of 2. Were we to say each pixel corresponds to 1 m, then the first minimum in figure 5-14b corresponds to 8.49 m as opposed to 6 m in figure 5-14a. When θ is 90 degrees, the inertia measure is zero for all d's. This is to be expected since the image intensities for θ parallel to the wave crests are identical and independent of d. Figure 5-14c shows this. Finally, for θ at 135 degrees we see the same pattern as when θ was 45 degrees (figure 5-14d).

Reproduced with permission of the copyright owner. Further reproduction prohibited without permission.

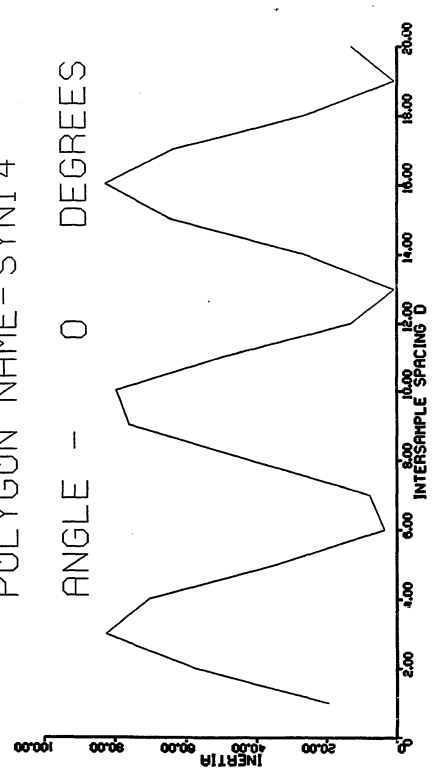

Figure 5-14a. For θ across the wave crests, the inertia plot shows a period of 6 pixels.

Reproduced with permission of the copyright owner. Further reproduction prohibited without permission.

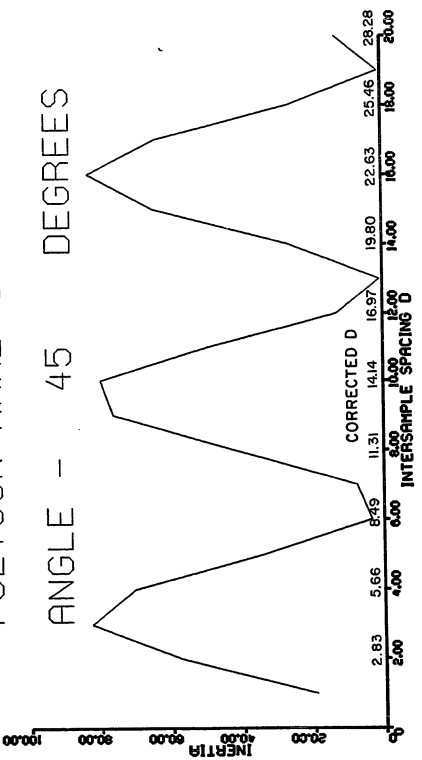

Figure 5-14b. When θ is oriented at 45 degrees, the period increases to 8.49 pixels.

Reproduced with permission of the copyright owner. Further reproduction prohibited without permission.

Figure 5-14c. When θ is oriented along the crests, the inertia measure is zero for all spacings.

Reproduced with permission of the copyright owner. Further reproduction prohibited without permission.

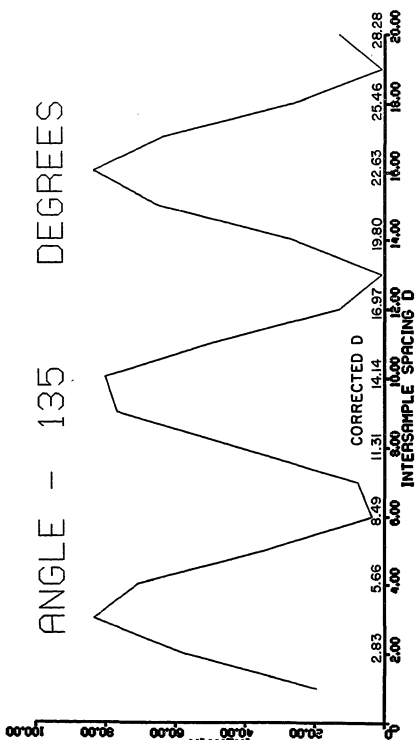

Figure 5-14d. This plot is identical to that in Figure 5-14b, due to wave symmetry.

Reproduced with permission of the copyright owner. Further reproduction prohibited without permission.

This is true because the wave pattern is perfectly periodic and symmetric about θ at 90 degrees.

This same pattern occurs for SAR ocean wave data. The scene N27C.FM5 is used as an example (figure 5-11). The 128 by 128 pixel region is chosen for analysis. Long-crested waves are traveling in the range dimension toward 180 degrees. The inertia plot for θ at 0 degrees shows a local minimum occuring for d at 7 to 8 pixels (figure 5-15a). The spatial resolution of the image is 9.95 m/pixel, so the wave period appears to be 69.6 m to 79.6 m. For simplicity, assume the minimum occurs for a d of 7 pixels. At 45 degrees, the minimum occurs for d at 7 pixels, but when corrected for absolute distance, d is 9.9 pixels or 98.5 m (figure 5-15b). At 90 degrees there is no minimum, and no wavelength (figure 5-15c). The increase in the inertia measure with d results from the scene not being perfectly periodic. When θ is 135 degrees, we see the minimum reappearing for d at 8 pixels, or 112.6 m (figure 5-15d). The difference in the inertia plots for θ at 45 and 135 degrees is attributed to the scene not being perfectly periodic, the wave crests not being perfectly parallel, and a slight deviation in the actual wave propagation direction from 180 degrees. Analysis of the FFT magnitude compares well with the textural analysis. Figure 5-12 shows the FFT magnitude, with a cluster centered at a frequency corresponding to a period of 79.4 m. The waves are traveling toward 176 degrees.

5.4 Cluster Shade and Phase Sensitivity

Several noteworthy discoveries about the cluster shade measure were made in this study. The first is that cluster shade can be used to measure the size of uniformly shaded regions, relative to the image

Reproduced with permission of the copyright owner. Further reproduction prohibited without permission.

Reproduced with permission of the copyright owner. Further reproduction prohibited without permission.

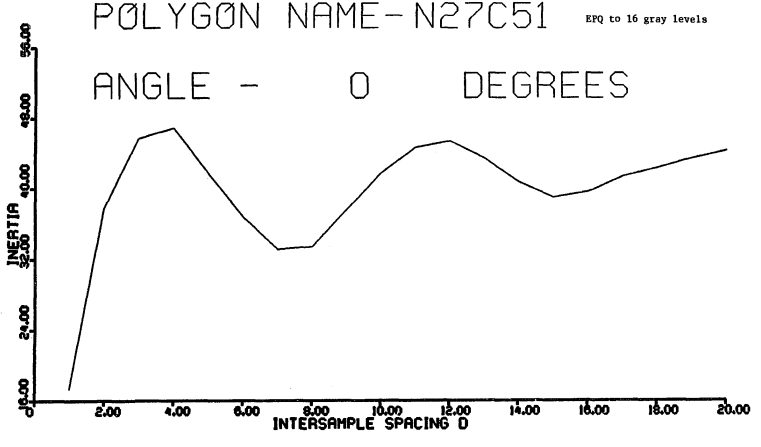

Figure 5-15a. The inertia plot for θ across the SAR ocean wave crests. The minimum corresponds to a wavelength between 69.6 and 79.6 m.

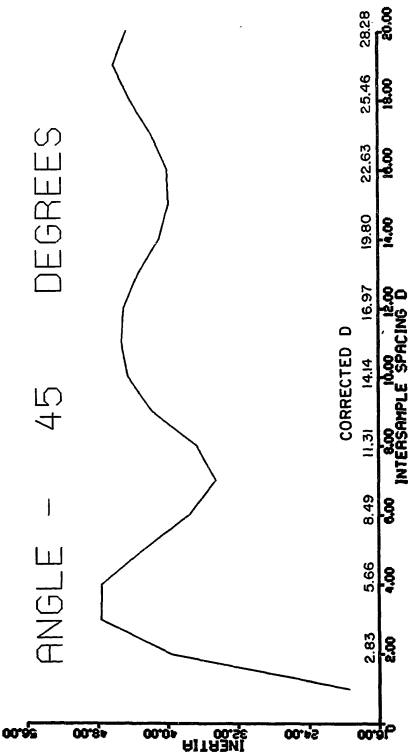

Figure 5-15b. When θ is oriented at 45 degrees, the wavelength increases to 98.5 m.

Reproduced with permission of the copyright owner. Further reproduction prohibited without permission.

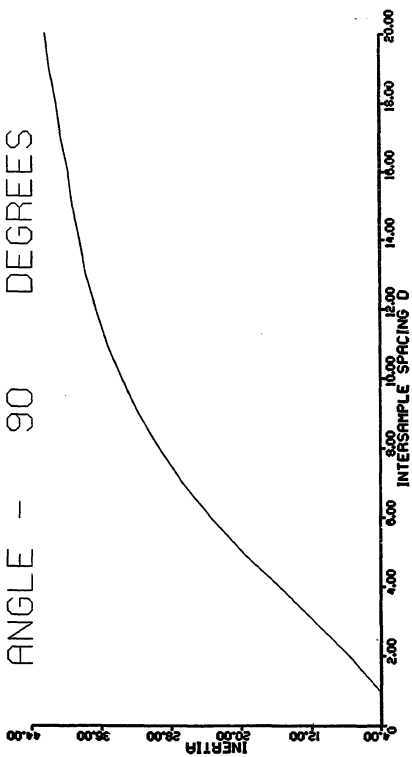

Figure 5-15c. When θ is oriented along the wave crests, there is no minimum.

Reproduced with permission of the copyright owner. Further reproduction prohibited without permission.

Reproduced with permission of the copyright owner. Further reproduction prohibited without permission.

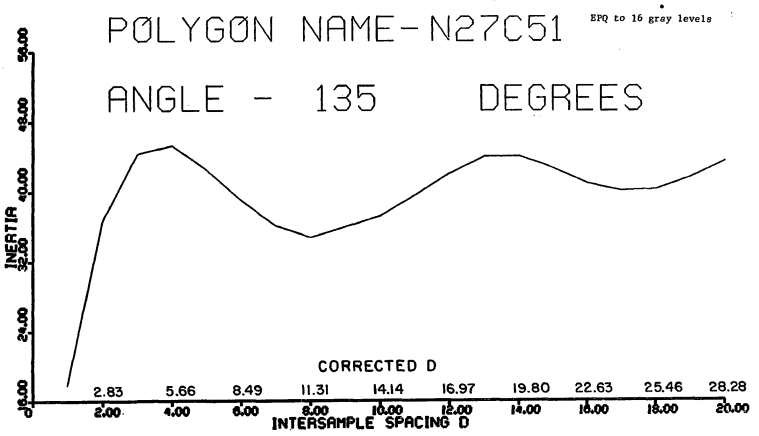

Figure 5-15d. The inertia plot for θ at 135 degrees differs from that at 45 degrees due to deviations from perfect symmetry in the waves.

mean intensity, assuming the areas of uniformity are statistically significant in the scene. Secondly, the cluster shade measure was found to be very sensitive to phase. This fact is especially important since it at least partially explains why cluster shade (or cluster prominence) is automatically selected in image classification exercises over inertia or local homogeneity. It also contributes greatly to our understanding of why the GLC method is more powerful than the PS method at texture discrimination.

A set of five computer synthesized wave images was used in the cluster shade study. Each contained two frequency components, a fundamental and its second harmonic. The phase difference between the fundamental and harmonic was varied from 0 degrees to -30 degrees, -45 degrees, -60 degrees and -90 degrees. The period of the fundamental was 25.6 pixels, and of the harmonic, 12.8 pixels. All processing was done on a 128 by 128 pixel region, with reduction to 16 gray levels by EPQ. Transects across the wave crests were extracted and plotted. Each of the six texture measures was plotted for θ oriented across the wave crests and d varied from 1 to 64 pixels. Fourier analysis was also done on all the measures. The data for each plot were padded on the front and tail with 32 zeros, thereby generating a 128 element, periodic signal. Both the magnitude and the phase of the FFT were computed and plotted.

As mentioned earlier in this chapter, the cluster shade and cluster prominence measures were suggested as a means of quantifying uniformity and proximity in the scene. The computer synthesized wave data verify that the cluster shade measure does so. Consider the image transect and cluster shade plots for phase differences of -30 and -90

Reproduced with permission of the copyright owner. Further reproduction prohibited without permission.

degrees. Figures 5-16a and 5-16b show the transect and cluster shade plot, respectively, for the -30 degree case. Figures 5-17a and 5-17b show the same for the -90 degree case. The mean intensity of both images is 64. If a line is drawn across the transects at a count of 64, and the width of the signal part whose counts are above 64 measured, this width is the same as the widest peak in the cluster shade measure. Likewise, if the width of the signal part whose counts are below the mean is measured, this width will be the same as the shorter, narrower peak in the cluster shade measure. In the -30 degree case, the width of the "bright", i.e. high count value, signal part is 17.5 pixels, while the width of the "dark", i.e. low count value, signal part is 7.5 pixels. These compare with widths of 18.0 and 7.25 pixels in the cluster shade plot. A similar relationship holds for the -90 degree case. Slight discrepancies in widths for all five cases can be attributed to two facts:

1. Neither the fundamental nor harmonic make an even number of cycles across the image. Therefore, quantization errors of up to one pixel can be expected in some cases.
2. The transects were extracted from the 256 gray level image while the cluster shade plots were based on 16 gray levels. This tends to make the raw signal less smooth due to quantization.

An interesting trend in the cluster shade plots for increasing phase differences is the increase in amplitude of the "bright" and "dark" peaks. These correspond directly to the increase in intensity of the signal values for increasing phase difference. The implication

Reproduced with permission of the copyright owner. Further reproduction prohibited without permission.

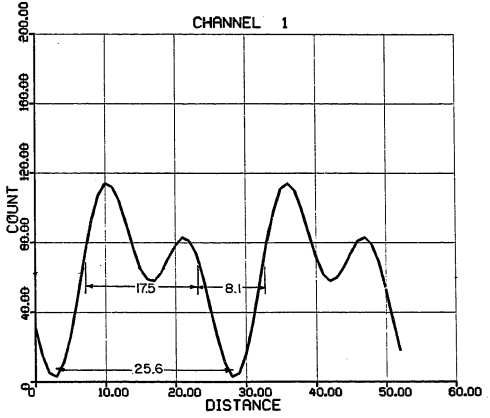

Figure 5-16a. A transect taken across two periods of the computer synthesized wave image composed of a fundamental and second harmonic, the harmonic being -30 degrees out of phase with the fundamental.

Reproduced with permission of the copyright owner. Further reproduction prohibited without permission.

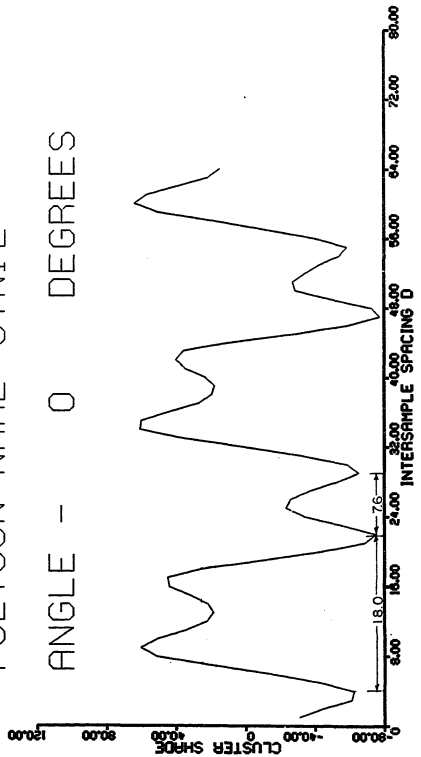

Figure 5-16b. The cluster shade plot of the image whose transect appears in Figure 5-16a. Compare the lobe widths with Figure 5-16a.

Reproduced with permission of the copyright owner. Further reproduction prohibited without permission.

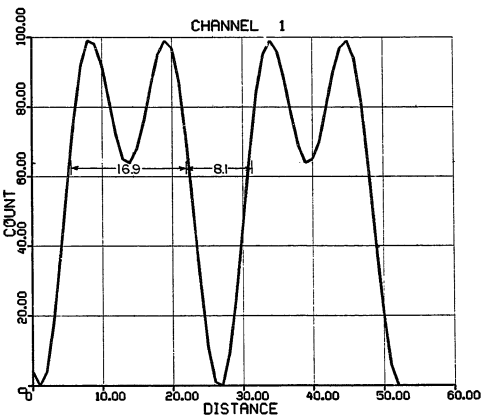

Figure 5-17a. A transect taken across two periods of the computer synthesized wave image composed of a fundamental and second harmonic, the harmonic being -90 degrees out of phase with the fundamental.

Reproduced with permission of the copyright owner. Further reproduction prohibited without permission.

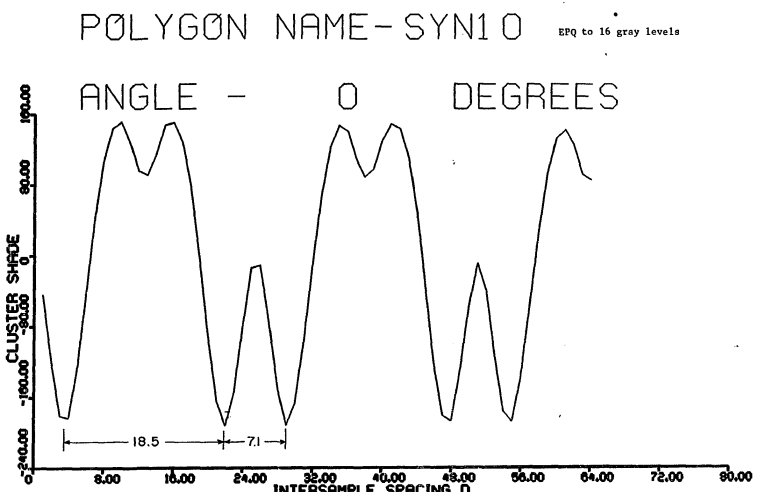

Figure 5-17b. The cluster shade plot of the image whose transect appears in Figure 5-17a. Compare the lobe widths with Figure 5-17a.

Reproduced with permission of the copyright owner. Further reproduction prohibited without permission.

is that the phase change in the imagery which is reflected as intensity changes in the signal is measured by the cluster shade measure. For example, the FFT phase plots of cluster shade for the lower frequencies in the -30 and -90 degree cases differ markedly (figures 5-18a and 5-18b). This is in vivid contrast to the FFT phase of the inertia plots, which are identical (figures 5-19a and 5-19b).

The sensitivity of cluster shade to phase verifies that the GLC matrices retain image phase information. This is a noteworthy revelation in light of the greater discrimination power of the GLC method relative to the PS method. It is well known that the phase of a signal's complex Fourier transform contains more information pertinent to the signal's reconstruction than the magnitude, or power [10]. Images reconstructed from their FFT magnitude, with the phase set constant, show little or no resemblance to the original image. Images reconstructed from their FFT phase, with the magnitude set constant, closely resemble the original scene. Because the GLC matrices retain phase information, they will always yield more powerful discrimination results than the power spectrum. The questions now become, "What texture measures optimally sense image phase, and how does one compare phase measures from the GLC matrices with phase measures from the FFT phase?" These questions are beyond the scope of this dissertation, but suggest an emphasis for further research.

5.5 Inertia and Cluster Shade Applied to Non-periodic SAR Features

The utility of the inertia and cluster shade measures in periodic scenes has been established, but what about their use in measuring roughly periodic or non-periodic features? Because of the mathematical link

Reproduced with permission of the copyright owner. Further reproduction prohibited without permission.

Reproduced with permission of the copyright owner. Further reproduction prohibited without permission.

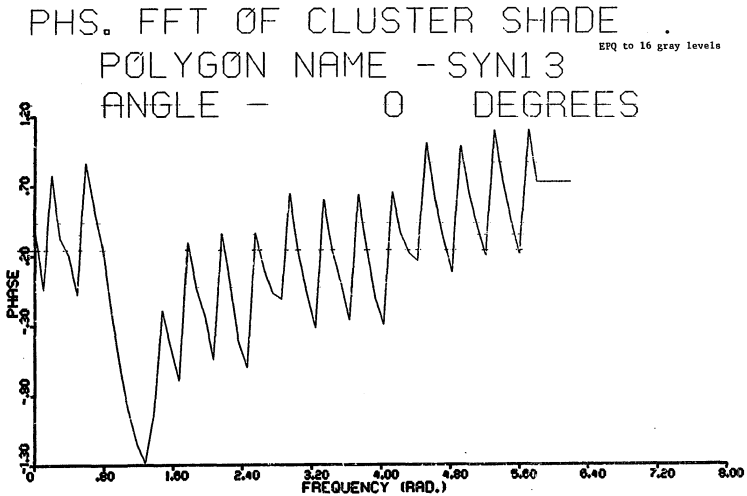

Figure 5-18a. The FFT phase computed on the cluster shade measure for the image whose transect appears in Figure 5-16a. Phases over a window five elements wide were averaged before plotting.

Reproduced with permission of the copyright owner. Further reproduction prohibited without permission.

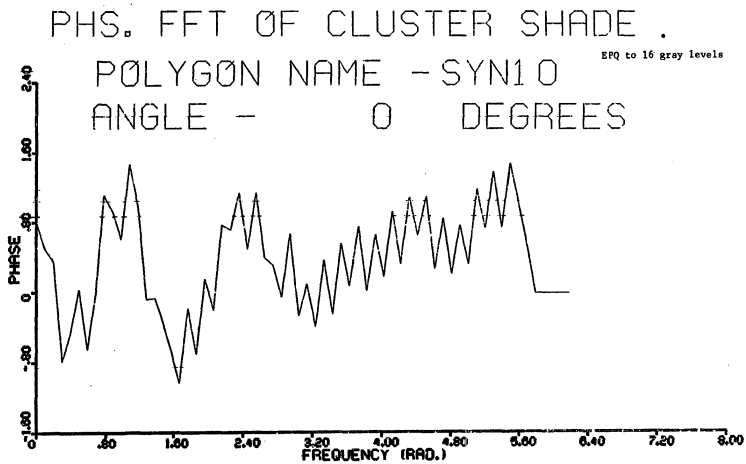

Figure 5-18b. The FFT phase computed on the cluster shade measure for the image whose transect appears in Figure 5-17a. Five element averaging was done before plotting. Note the phase difference between this plot and that shown in Figure 5-18a.

Reproduced with permission of the copyright owner. Further reproduction prohibited without permission.

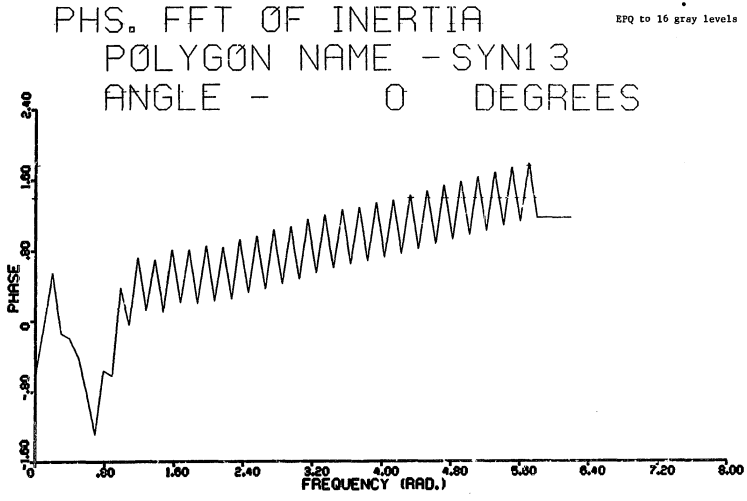

Figure 5-19a. The FFT phase computed on the inertia measure for the image whose transect appears in Figure 5-16a. Phases over a window five elements wide were averaged before plotting.

Reproduced with permission of the copyright owner. Further reproduction prohibited without permission.

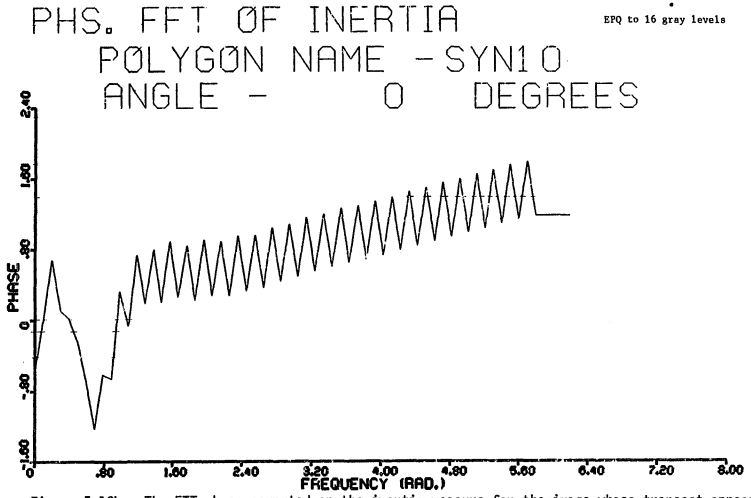

Figure 5-19b. The FTT phase computed on the inertia measure for the image whose transect appears in Figure 5-17a. Five element averaging was done before plotting. Note that this plot is identical to that shown in Figure 5-19a.

between the inertia measure and the autocorrelation function, one would expect the inertia measure to be as successful as the power spectrum at characterizing extreme departures from periodicity. One would also expect the cluster shade measure to be capable of measuring uniformity and proximity only when 1) the uniformity texture is statistically significant in the scene and 2) there is not a great deal of size and placement variation in the uniform texture. The following examples bear this out.

A roughly periodic and non-periodic SAR wind scene were analyzed to assess the inertia and cluster shade measures. The roughly periodic feature is a wind streak pattern on the north end of the Gotoh Islands of Japan. The wind streaks are the thin, light lineations oriented at about 135 degrees in the scene N27A.FM9 (figure 5-20). The 128 by 128 pixel region analyzed is shown in the scene. This region was gray level reduced to 16 gray levels via EPQ. It was then DC bias processed, cosine weighted and two-dimensionally Fourier transformed. The FFT magnitude was generated (figure 5-21). The unbiased, unweighted region was also texture processed for θ at 54 degrees (across the wind streaks) and d from 1 to 64 pixels. Inertia and cluster shade plots were made and are shown in figures 5-22 and 5-23, respectively. The fact that the FFT magnitude shows frequency dispersion radially at 54 degrees attests to the degree of non-periodicity in wind streaks; however, there are a few energy clusters corresponding to a period of roughly 18 pixels. The inertia measure plot does not readily reveal any periodicities. A one-dimensional FFT was performed on the inertia plot, and its magnitude is shown in figure 5-24. The first lobe right of DC corresponds to a period of 20.9 pixels, which is in rough agreement

Reproduced with permission of the copyright owner. Further reproduction prohibited without permission.

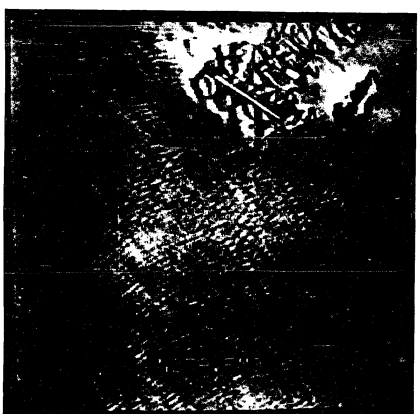

Figure 5-20. Scene N27A.FM9 is from an area on the north end of the Gotoh Islands. Wind streaks within the region N27A91 were analyzed.

Reproduced with permission of the copyright owner. Further reproduction prohibited without permission.

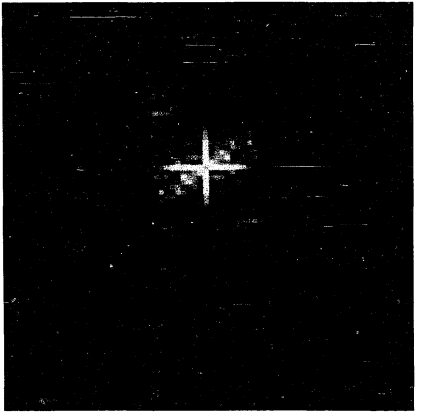

Figure 5-21. The two-dimensional FFT magnitude of the region N27A91 in Figure 5-20. The region was EPQ gray level reduced to 16 gray levels and the edges cosine weighted before transforming. The wind streaks are visible at 54 degrees.

Reproduced with permission of the copyright owner. Further reproduction prohibited without permission.

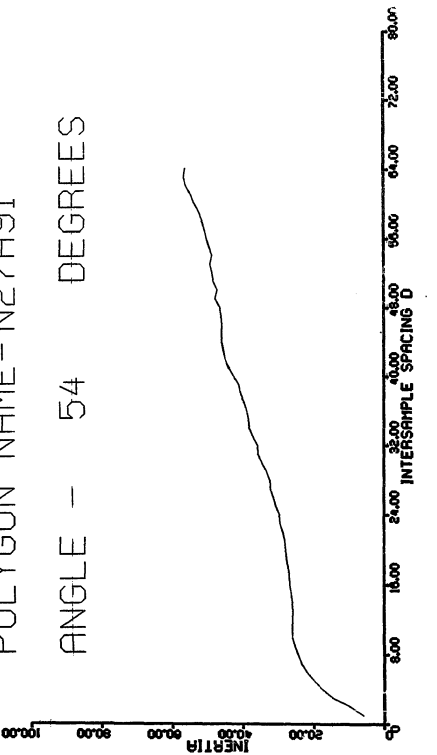

Figure 5-22. The inertia plot computed across the wind streaks.

Reproduced with permission of the copyright owner. Further reproduction prohibited without permission.

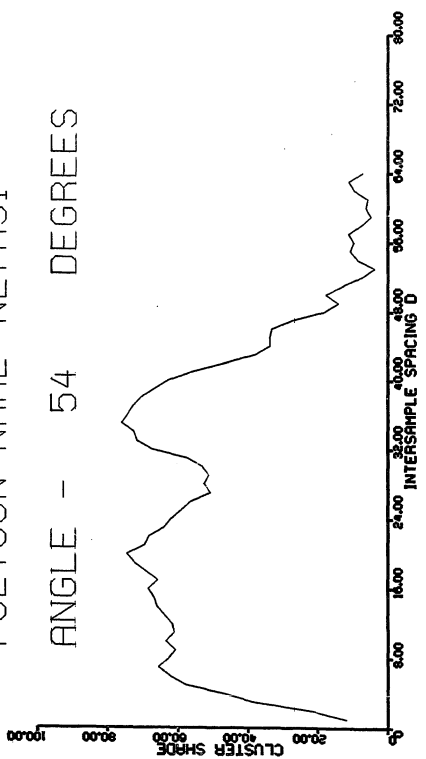

Figure 5-23. The cluster shade plot computed across the wind streaks.

Reproduced with permission of the copyright owner. Further reproduction prohibited without permission.

Reproduced with permission of the copyright owner. Further reproduction prohibited without permission.

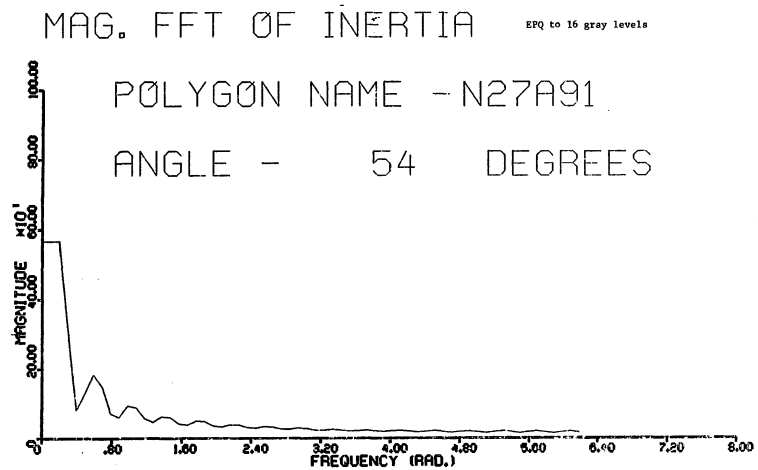

Figure 5-24. The FFT magnitude of the plot in Figure 5-22. The first lobe right of DC corresponds to a period of 20.9 pixels.

with the two-dimensional FFT magnitude. As one would expect, based on the mathematical relationship between inertia and the autocorrelation function, the inertia measure and the power spectrum sense roughly periodic structures equally well. The cluster shade measure shows a relative minimum at approximately 28 pixels and an absolute minimum at 52 pixels. While the local minimum roughly agrees with the wind streak period detected in the FFT magnitude, the 52 pixel period is not visually discernible in the image. This casts doubt on the utility of cluster shade to detect the presence of roughly periodic features such as wind streaks.

The non-periodic wind scene is of cat's paws in the wind wake of one of the Gotoh Islands. Within the scene A31A.F12, a 128 by 128 pixel region was selected. The cat's paws are the dark, roughly round patterns within the polygon marked A31A121 in figure 5-25. A vertical transect was extracted and plotted in figure 5-26 to show the variability in uniformity and proximity. In addition to the FFT magnitude computed on the 16 gray level, DC biased and edge weighted EPQ region, the inertia and cluster shade measures were computed vertically and horizontally for d from 1 to 64. The two-dimensional FFT magnitude is shown in figure 5-27, and the inertia and cluster shade plots are shown in figures 5-28 through 5-31. None of these reveal periodic components, nor does the cluster shade measure show minima corresponding to the width of intensity clusters from the transect shown in figure 5-26. Neither cluster shade nor inertia is sensitive to non-periodic wind features.

Reproduced with permission of the copyright owner. Further reproduction prohibited without permission.

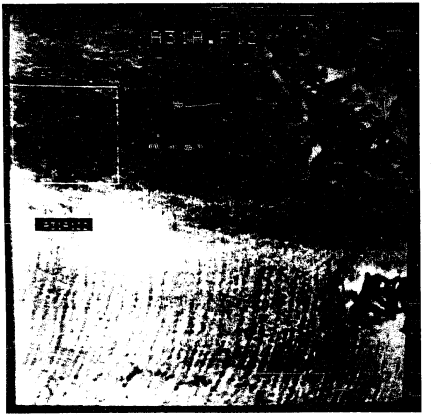

Figure 5-25. Scene A31A.F12. The region A31A121 contains turbulent wind patterns, the result of wind wake from an adjacent island. The roughly round, dark areas are "cat's paws."

Reproduced with permission of the copyright owner. Further reproduction prohibited without permission.

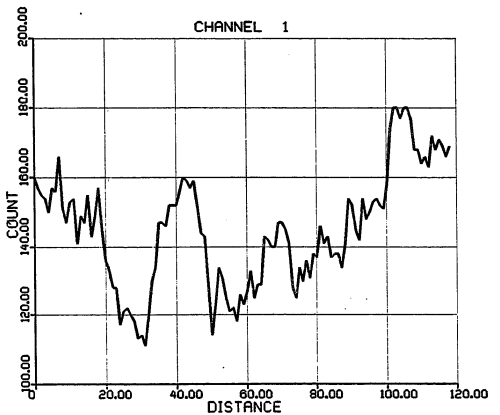

Figure 5-26. A transect extracted vertically across the cat's paws region. Note the variation in uniformity and proximity of intensity signatures.

Reproduced with permission of the copyright owner. Further reproduction prohibited without permission.

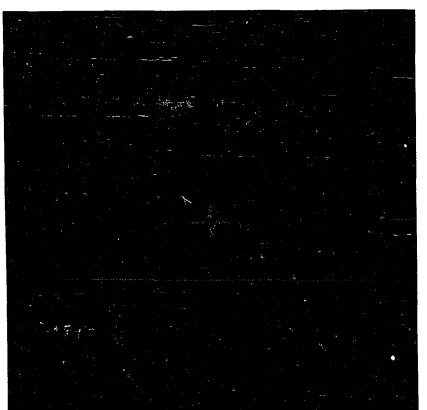

Figure 5-27. The two-dimensional FFT magnitude of the region A31A.F12 in Figure 5-25. The region was EPQ gray level reduced to 16 gray levels and the edges cosine weighted before transforming. The FFT magnitude is essentially isotropic.

Reproduced with permission of the copyright owner. Further reproduction prohibited without permission.

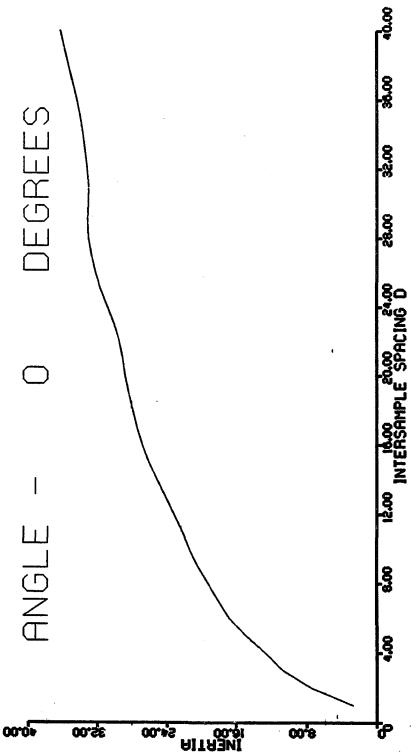

Figure 5-28. The inertia plot computed for the region A31A121, θ = 0 degrees.

Reproduced with permission of the copyright owner. Further reproduction prohibited without permission.

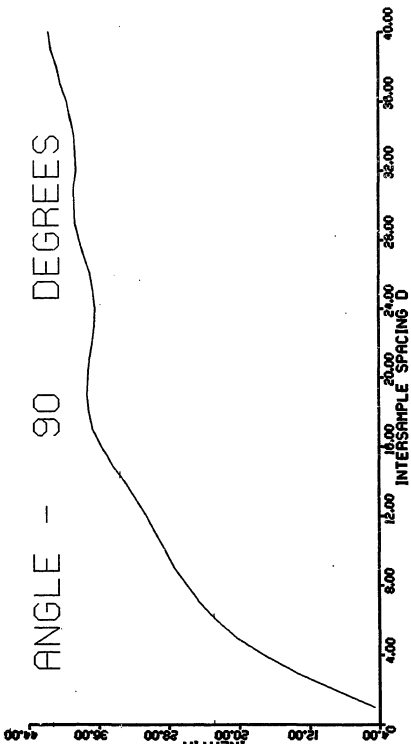

Figure 5-29. The inertia plot computed for the region A31A121, $\theta = 90$ degrees.

Reproduced with permission of the copyright owner. Further reproduction prohibited without permission.

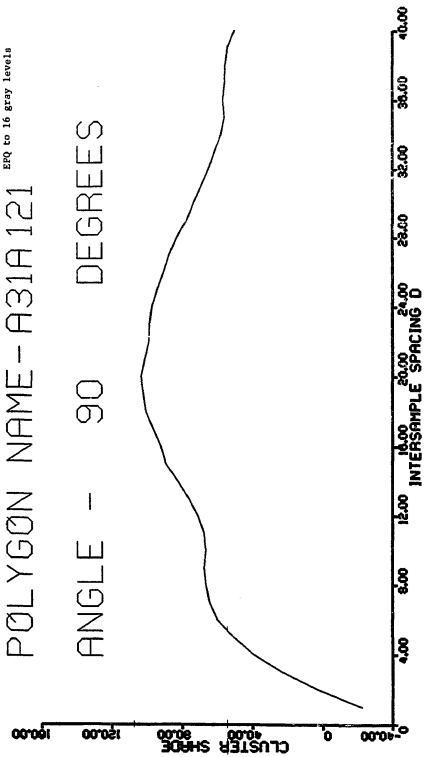

Figure 5-30. The cluster shade plot computed for the region A31A121, θ = 90 degrees.

Reproduced with permission of the copyright owner. Further reproduction prohibited without permission.

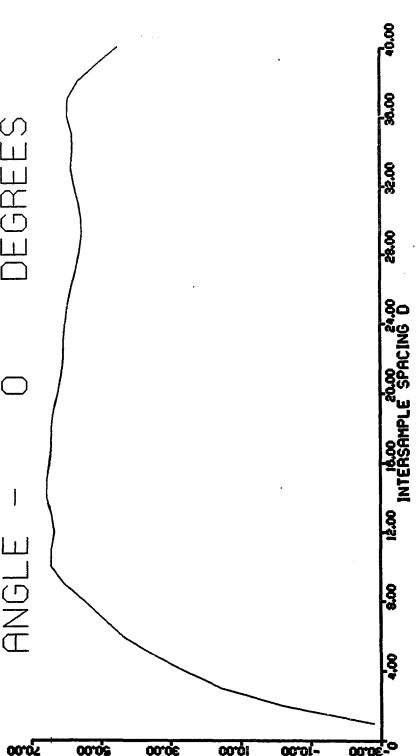

Figure 5-31. The cluster shade plot computed for the region A31A121, θ = 0 degrees.

Reproduced with permission of the copyright owner. Further reproduction prohibited without permission.

REFERENCES

1. Conners, R.W. and C.A. Harlow, "A Theoretical Comparison of Texture Algorithms," IEEE Trans. Pattern Anal. Mach. Intell., Vol. PAMI-2, No. (May 1980), pp. 204-222.

2. Conners, R.W. and C. A. Harlow, "Equal Probability Quantization and Texture Analysis of Radiography Images," Comp. Graph. Image Proc., Vol. 8, No. 3, (Dec. 1978), pp. 447-463.

3. Haralick, R.M. and K. Shanmugan, "Computer Classification of Reservoir Sandstones," IEEE Trans. Geosci. Electron., Vol. GE-11 (Oct. 1973), pp. 171-177.

4. Haralick, R.M., K. Shanmugan, I. Dinstein, "Textural Features for Image Classification," IEEE Trans. Syst., Man Cybernet., Vol. SMC-3, No. (Nov. 1973), pp. 610-621.

5. Harlow, C.A., R.W. Conners, M.M. Trivedi, D.A. DiRosa and R.E. Vasquez-Espinosa, "Texture Analysis and Urban Land Use Classification," in Proc. SOUTHEASTCON, Huntsville, Alabama (April 1981), pp. 115-119.

6. Julesz, B., "Visual Pattern Discrimination," IRE Trans. Inf. Theory, It-8 (1962), pp. 84-92.

7. Conners, R.W. and C.A. Harlow, "Toward a Structural Textural Analyzer," Comp. Graph. Image Proc., Vol. 12, No. 3 (March 1980), pp. 224-256.

8. Brodatz, P., Textures: A Photographic Album For Artists And Designers , ERS. New York, N.Y.: Dover Publications, 1966.

9. Mastin, G.A., "Periodicity Detection: The Power Spectrum versus the Inertia Texture Measure," RSIP Tech. Report No. RSIP TR 301.83, Remote Sensing and Image Processing Lab., Louisiana State University, Baton Rouge, LA, March 1983.

10. Oppenheim, A.V. and J.S. Lim, "The Importance of Phase in Signals," Proc. IEEE , Vol. 69, No. 5 (May 1981), pp. 529-541.

Reproduced with permission of the copyright owner. Further reproduction prohibited without permission.

CHAPTER 6

CONCLUSIONS AND RECOMMENDATIONS FOR FURTHER RESEARCH

A number of conclusions and recommendations can be drawn from the new research in chapters 4 and 5. Their diversity can best be managed by considering the research from two frames of reference, geophysical analysis and digital image analysis.

From the geophysical frame of reference, a heretofore suspected but undocumented capability of SAR imagery has been demonstrated, and two potentially valuable applications of SAR image analysis introduced. Determining wind direction from wind rows, wind streaks and turbulent zones is a unique result of this research and emphasizes the utility of high resolution X-band SAR imagery for synoptic scene analysis. The increased resolution of the SAR aircraft imagery, when compared to SEASAT, accounts for our ability to visually identify wind patterns and adequately sample them for computer processing. The shorter wavelengths of the X-band Bragg scatterers are more sensitive to wind flow than those of L-band SAR systems, making X-band the preferential SAR frequency band. The two applications of SAR image analysis introduced in chapter 4 extend SAR utilization beyond determining wave direction and length. Existing empirical relations allow a number of important sea state parameters to be estimated. Wavelength, easily and fairly reliably extracted from any point in a SAR image, along with wind speed, has been shown here to estimate wave height and aerodynamic roughness parameters. Routine esti-

Reproduced with permission of the copyright owner. Further reproduction prohibited without permission.

mation of these parameters can and should be used to refine sea state empirical relations and thereby provide a better synoptic analysis technique. The second application unites these estimates with existing digital hardware and software capabilities to display spectra, imagery and text simultaneously. This creates synoptic sea state charts very similar in function to synoptic weather charts. No other sensor in combination with a computer can generate these charts day and night, regardless of cloud cover.

Most of the future work in geophysical SAR image analysis should center on building a research data base. Currently available surface weather and sea state data should accompany SAR imagery of selected areas in the base. Time series analysis is very important, so the selected areas should be routinely imaged and documented. Increased availability of digital SAR systems would greatly simplify and broaden synoptic SAR geophysical analysis capabilities. The data base would allow quantitative refinement of SAR parameter estimation relations and thereby provide an increasingly reliable scene analysis tool.

From the digital image analysis frame of reference, two extremely important conclusions can be drawn. The first is that texture analysis based on the GLC matrix method is a valuable tool in SAR scene analysis. The inertia measure has been shown to be as valuable as the power spectrum, and the inertia measure is just one of many measures. Secondly, the cluster shade measure has demonstrated a significant aspect of the GLC matrices. The matrices retain both magnitude and phase information from the scene. Inertia has been theoretically and empirically linked to magnitude information, while cluster shade has been experimentally linked to phase. This finding offers a partial, if not complete, ex-

Reproduced with permission of the copyright owner. Further reproduction prohibited without permission.

planation of why Conners and Harlow [Ref. 1, Chpt. 5] found the GLC matrix method to be superior to the PS method at texture discrimination.

Future research in texture analysis should move beyond PS analysis and concentrate on phase analysis. The move beyond PS analysis is particularly important in SAR image analysis because the additional information in phase data represents a valuable resource which must be tapped, despite a traditional affinity to PS analysis by the geophysical and engineering community. Whether done in the GLC matrix domain or in the Fourier domain, a concentrated effort must be made to identify phase sensitive measures. The cluster shade measure is just one of many that are conceivable. This is especially important since image analysts have long known that image reconstruction is best done with phase data rather than with magnitude data, yet no systematic measures of phase sensitivity have been suggested to date.

Reproduced with permission of the copyright owner. Further reproduction prohibited without permission.

APPENDIX 1

BASIC STRIPMAP SAR PHYSICS

STRIPMAP GEOMETRY

The stripmap SAR imaging geometry is shown in Figure A-1. The radar is side-looking and mounted in an aircraft (or spacecraft). As the radar antenna is transported in the azimuth, or along-track, dimension, the radar's physical aperture illuminates a ground strip with microwave radiation having a beamwidth, β , and depressed from the aircraft's horizontal plane by an angle α. The range from the aircraft to any point, P, on the ground is the slant-plane distance, R. R_0 is the slant-plane range to the center of the beamwidth.

RANGE RESOLUTION

Range, or across-track, resolution is determined by the time delay of pulsed transmitted signals. The round trip propagation time, ΔT, for a target at slant-range R is

$$\Delta T = \frac{2R}{c} \qquad \text{(A-1)}$$

where c is the speed of light. The time length of each pulse, τ, and the pulse length, lp are related by the expression

$$lp = c\tau \qquad \text{(A-2)}$$

Two targets separated in slant-range by a distance ΔR will be resolved

Reproduced with permission of the copyright owner. Further reproduction prohibited without permission.

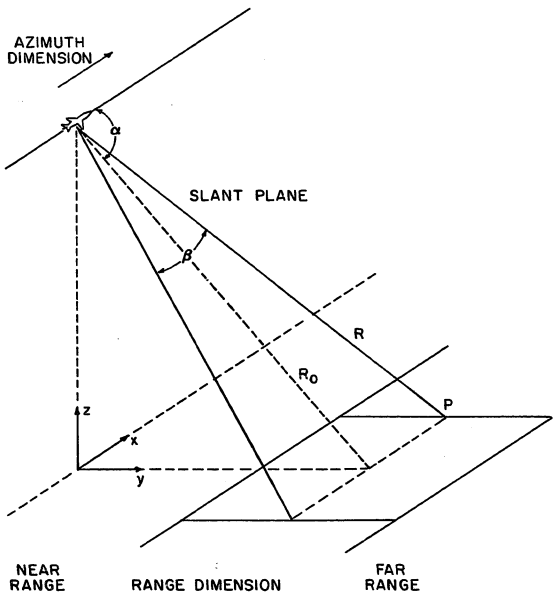

Figure A-1. SAR geometry.

Reproduced with permission of the copyright owner. Further reproduction prohibited without permission.

as long as

$$\Delta R \geq \frac{l_p}{2} = \frac{c\tau}{2} \quad . \tag{A-3}$$

In other words, the two targets can only be resolved if the return from the first target is separated in space from that of the second target. The minimum target separation which allows this is one where the round trip travel distance between the first and second targets equals one pulse length. The round trip travel distance must therefore be at least half the slant-range target separation. This is illustrated in Figure A-2.

The slant-range resolution, ρ_R, is then

$$\rho_R = \frac{c\tau}{2} \quad . \tag{A-4}$$

This corresponds to a signal bandwidth given by

$$W = \frac{1}{\tau} = \frac{c}{2\rho_R} \quad . \tag{A-4a}$$

The preceeding development assumes a rectangular pulse. Based on this, improved range resolution is achieved by transmitting shorter, narrower pulses. Decreasing the pulse width implies increasing the radar bandwidth which results in increased noise. This requires a proportional increase in pulse amplitude to assure a reasonable signal-to-noise ratio at the receiver. Furthermore, increasing the pulse repetition frequency increases the number of times targets in the radar beam return the signal. Returns from targets farther in range may not be received until the next pulse is transmitted, causing a range

Reproduced with permission of the copyright owner. Further reproduction prohibited without permission.

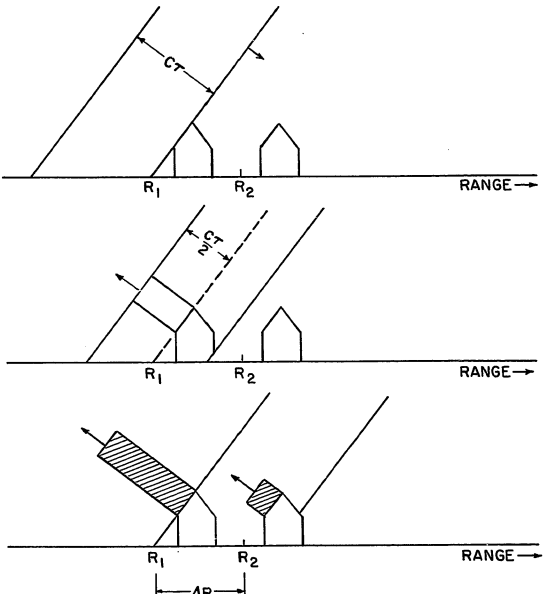

Figure A-2. Slant-range resolution for a rectangular pulse. Two targets are resolved when the pulse round trip travel distance between the targets equals one pulse length.

Reproduced with permission of the copyright owner. Further reproduction prohibited without permission.

sorting dilemma called range ambiguity. It is therefore impractical to try to produce short, narrow pulses for high range resolution SAR's. Practicality dictates transmitting a longer, "smoother" pulse to increase the average power, decrease noise and increase range. High resolution dictates short pulses. The solution is to transmit a chirped signal. A long pulse length signal having the appropriate frequency response is generated with fairly low peak power, modulated up to microwave frequencies and transmitted. The received signal is amplified and compressed. Lower frequencies arrive first, but are delayed longer than the higher frequencies, yielding a short pulse with increased peak amplitude. In optical systems, the received, expanded pulse is recorded directly on film. Compression is done by lenses in the optical correlator.

Although the rectangular pulse development does not represent the practical implementation, it is still conceptually valid and is usually regarded as the standard model in the literature.

A final point concerning range determination should be made. The rectangular pulse model assumes targets of equal height. Taller objects, such as towers, will have their top portion return the signal with a delay characteristic of a short object nearer the radar in the ground-plane. Tall objects will then appear to have been laid down in the image, with their top nearer in range than their bottom. This is called range lay-over and is a function of the imaging geometry. Range lay-over does not influence the fundamental resolution of the system, but can obscure targets nearer in the ground-range dimension.

Reproduced with permission of the copyright owner. Further reproduction prohibited without permission.

AZIMUTH RESOLUTION

Azimuth, or along-track, resolution may be developed by first considering the properties of a real aperture imaging radar, then applying Doppler concepts to develop the synthetic array concept which yields higher resolution. The starting point is a model of a real aperture antenna pattern based on Frauenhaufer diffraction.

From the geometry in Figure A-3,

$$D \sin \theta = d \quad . \tag{A-5}$$

The microwave phase difference between elements, e_1 and e_2 is given as

$$\phi = \frac{2\pi d}{\lambda_o} \tag{A-6}$$

and substituting equation (A-5) into equation (A-6) we get

$$\phi = \frac{2\pi D \sin\theta}{\lambda_o} \quad . \tag{A-7}$$

At this point, two simplifying assumptions may be made. The first relates the interelement spacing, D, to the length of the antenna, L.

$$L = D(n-1) \tag{A-8}$$

If we consider the antenna to be composed of a very large number of elements, then

$$L \simeq Dn \tag{A-9}$$

and

$$\phi = \frac{2\pi L \sin\theta}{n\lambda_o} \quad . \tag{A-10}$$

Reproduced with permission of the copyright owner. Further reproduction prohibited without permission.

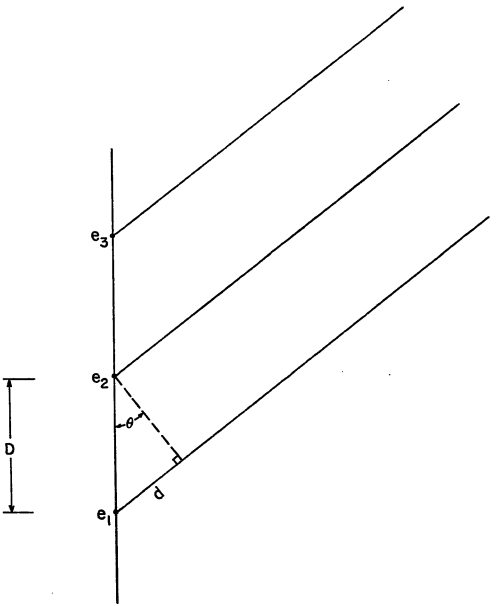

Figure A-3. Real aperture radar antenna composed of elements, e_i, separated by a distance, D.

Reproduced with permission of the copyright owner. Further reproduction prohibited without permission.

The second assumption is that θ is small, making $\sin\theta \simeq \theta$. Then,

$$n\phi = \frac{2\pi L\theta}{\lambda_0} \tag{A-11}$$

or

$$\frac{n\phi}{2} = \frac{\pi L\theta}{\lambda_0} \tag{A-12}$$

Let the amplitude and phase of the energy received at an antenna element be represented by a phasor. The antenna pattern is then formed by vectorially summing the phasors for all elements. If we assume the amplitude of each phasor is identical, then the total energy received is the scalar sum of amplitudes at each element and is represented by an arc of length A_0. The resultant energy amplitude is the vector sum, A, as shown in Figure A-4. The ratio of the chord length, A to the arc length, A_0, is the ratio of the resultant amplitude at any element along the antenna to the total energy received by the antenna. The chord length, A, is determined from the geometry of Figure A-5,

$$\sin\frac{n\phi}{2} = \frac{A/2}{R} \tag{A-13}$$

$$A = 2R \sin\frac{n\phi}{2} \tag{A-14}$$

The arc length is simply stated

$$A_0 = Rn\phi \tag{A-15}$$

so that the energy amplitude relationship for the antenna is

Reproduced with permission of the copyright owner. Further reproduction prohibited without permission.

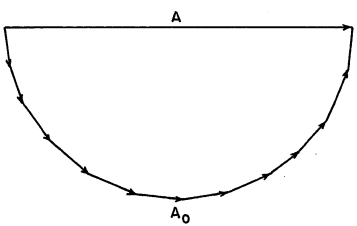

Figure A-4. Phasor plot of all antenna elements.

Reproduced with permission of the copyright owner. Further reproduction prohibited without permission.

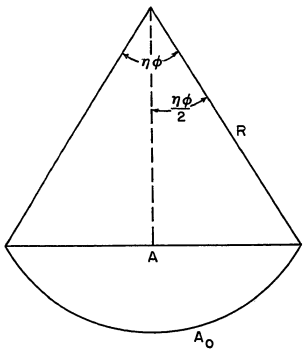

Figure A-5. Phasor plot geometry.

Reproduced with permission of the copyright owner. Further reproduction prohibited without permission.

$$\frac{A}{A_0} = \frac{\sin \frac{n\phi}{2}}{\frac{n\phi}{2}} \tag{A-16}$$

or

$$A = A_0 \frac{\sin \gamma}{\gamma} \tag{A-17}$$

where $\gamma = \frac{n\phi}{2}$. The first null occurs when

$$\gamma = \pi k \quad ; \; k = 1,2,... \tag{A-18}$$

and substituting equation (A-12) we get

$$\gamma = \frac{n\phi}{2} = \frac{\pi L \theta}{\lambda_0} = \pi k \tag{A-19}$$

and the first null occurs at the angle

$$\theta = \frac{\lambda_0}{L} \quad . \tag{A-20}$$

The angular width between the symmetrically distributed first null is 2θ. Antenna beamwidth is defined as the half-power angle of this main lobe of the antenna pattern. The half-power points occur at

$$\pm \frac{\theta}{2} = \pm \frac{\lambda_0}{2L} \tag{A-21}$$

so the angular beamwidth, β, is represented as

$$\beta = 2\left(\frac{\theta}{2}\right) = \frac{\lambda_0}{L} \tag{A-22}$$

Reproduced with permission of the copyright owner. Further reproduction prohibited without permission.

which is a fundamental antenna relation.

Azimuth resolution is a function of β and the range to the target. This is easily seen when we project the antenna pattern in range, as shown in Figure A-6. Targets further in range have a lower resolution than at near range because resolvable targets must be separated in azimuth by at least an angle of β, and β increases with range. Slant-plane azimuth resolution is given by

$$\rho_A = \beta R \qquad \text{(A-23)}$$

Substituting equation (A-22) yields

$$\rho_A = \frac{\lambda_o R}{L} \qquad \text{(A-24)}$$

which not only states that resolution is a function of range, but states that the resolution at range R may be increased by increasing L or decreasing λ_o. All weather imaging restricts λ_o and the physical antenna length, L, is limited by aircraft performance restrictions.

The synthetic aperture approach overcomes this seemingly unsolvable dilemma by synthesizing a large L antenna. As the antenna is transported between two points in space, the radar pulse repetition frequency and the aircraft (or spacecraft) velocity are adjusted so that antenna element transmissions occur in the same locations as a physical antenna having the length of the flight path. Phase information is stored during antenna synthesis. Signal processing is later done to sum the amplitude and phase of the received energy, thereby creating the antenna pattern. The result is a pattern having a narrower beamwidth and

Reproduced with permission of the copyright owner. Further reproduction prohibited without permission.

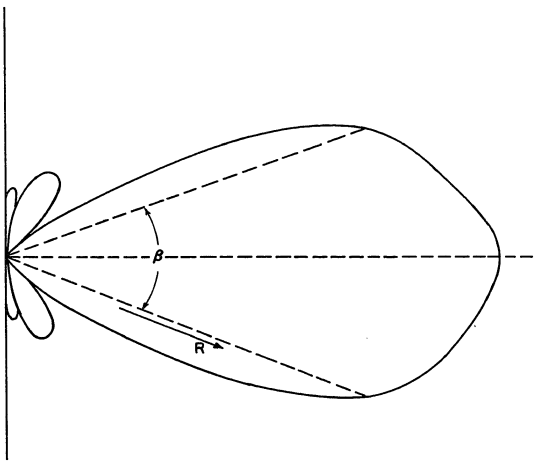

Figure A-6. Real aperture antenna pattern.

Reproduced with permission of the copyright owner. Further reproduction prohibited without permission.

therefore greater azimuth resolution.

If the radar transmits and receives energy from each elemental position of the synthetic antenna, the phase difference between positions is

$$\phi = \frac{2\pi(2R)}{\lambda_o} = \frac{4\pi R}{\lambda_o} \qquad \text{(A-25)}$$

The factor 2R corresponds to the round trip phase difference for a target at slant-range R. The slant-range to a target varies as the antenna moves

$$R = (R_o^2 + x^2)^{1/2} \qquad \text{(A-26)}$$

where R_o is the broadside range to the target as shown in Figure A-7. Substituting equation (A-26) into (A-25) yields

$$\phi = \frac{4\pi}{\lambda_o}(R_o^2 + x^2)^{1/2} \qquad \text{(A-27)}$$

$$= \frac{4\pi R_o}{\lambda_o}\left(1 + \frac{x^2}{R_o^2}\right)^{1/2} \qquad \text{(A-28)}$$

Terms of the form $(1+\epsilon)^{1/2}$ may be expanded as

$$(1+\epsilon)^{1/2} = 1 + \frac{\epsilon}{2} - \frac{\epsilon^2}{8} + \ldots \qquad \text{(A-29)}$$

so, taking the first 2 terms,

Reproduced with permission of the copyright owner. Further reproduction prohibited without permission.

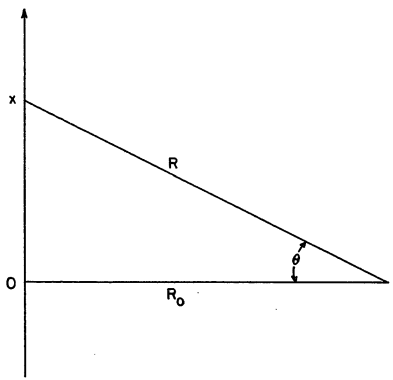

Figure A-7. Slant-plane geometry.

Reproduced with permission of the copyright owner. Further reproduction prohibited without permission.

$$\phi = \frac{4\pi}{\lambda_o}(R + \frac{x^2}{2R_o}) \tag{A-30}$$

$$= \phi_o + \frac{2\pi x^2}{\lambda_o R_o} \tag{A-31}$$

where ϕ_o is the constant phase term. The Doppler frequency shift associated with a target is the time rate of change of phase given by

$$\nu = \frac{1}{2\pi} \frac{d\phi}{dt} \tag{A-32}$$

$$= \frac{1}{2\pi} \frac{d}{dt} [\frac{4\pi}{\lambda_o}(R_o^2 + x_o^2)^{1/2}] \tag{A-33}$$

$$= \frac{2}{\lambda_o} \frac{x}{(R_o^2 + x^2)^{1/2}} \frac{dx}{dt} \tag{A-34}$$

$$= \frac{2V}{\lambda_o} \sin \theta \tag{A-35}$$

which is the Doppler equation. The factor of 2 is attributed to two shifts which occur; one received at the target due to the apparent motion of the radar toward the target, and one received at the antenna due to the apparent motion of the target toward the radar.

Two targets at the same range are resolved in azimuth by the difference in their Doppler shifts. If one target is at an angle θ_1 relative to the antenna, and the other target is at θ_2 then the Doppler shift difference is

Reproduced with permission of the copyright owner. Further reproduction prohibited without permission.

$$\Delta\nu = \nu_2 - \nu_1 = \frac{2V}{\lambda_o}(\sin\theta_2 - \sin\theta_1) \qquad \text{(A-36)}$$

For small θ, $\sin\theta \simeq \theta$ and

$$\Delta\nu \simeq \frac{2V}{\lambda_o}\ \Delta\theta \qquad \text{(A-37)}$$

The Doppler angle, $\Delta\theta$, is physically limited by the half-power beamwidth of the antenna. Therefore,

$$\beta = \Delta\theta \qquad \text{(A-38)}$$

Substituting equation (A-38) into (A-37) yields

$$\frac{\lambda_o}{2\beta} = \frac{V}{\Delta\nu} \qquad \text{(A-39)}$$

where $V/\Delta\nu$ is the azimuth resolution. Finally,

$$\rho_A = \frac{\lambda_o}{2\beta} \qquad \text{(A-40)}$$

and substituting equation (A-20),

$$\rho_A = L/2 \qquad \text{(A-41)}$$

Equation (A-41) is a famous result. It says that the maximum resolution of a SAR is half the length of the physical antenna. It is remarkable that a narrow beam antenna pattern is created from many antennas having a short length, and therefore a wide beamwidth.

Reproduced with permission of the copyright owner. Further reproduction prohibited without permission.

APPENDIX 2

SOFTWARE LISTINGS AND DATA

The number of lines of code prohibit the inclusion of software listings in this dissertation. Source code is on file in the Remote Sensing and Image Processing Laboratory tape library, Department of Electrical and Computer Engineering, Louisiana State University, Baton Rouge, Louisiana 70803. Line printer listings and magnetic tape backups are in the care of Dr. Charles Harlow, director of the laboratory. It should be noted that all software is written in FORTRAN 77 and was implemented on a Perkin-Elmer 8/32 minicomputer. Almost all of the SAR processing software is written as overlays which interface with a large image processing package called ELAS, written and distributed by the National Aeronautics and Space Administration.

Image data analyzed in this dissertation are also on file in magnetic tape format in the RSIP tape library. Release of this data may require the prior approval of the Japan Self Defense Air Force. Inquiries should be forwarded to Dr. Oscar Huh, Coastal Studies Institute, Louisiana State University, Baton Rouge, Louisiana 70803.

Reproduced with permission of the copyright owner. Further reproduction prohibited without permission.

VITA

Gary Mastin was born in Wichita, Kansas,on March 6, 1954. He is the son of Mary Helen and Arthur W. Mastin, both educators retired from the Wichita Public Schools. Gary graduated from Wichita High School North in 1972. The following fall he began his undergraduate work in physics at Ottawa University, Ottawa, Kansas. He graduated Summa Cum Laude from Ottawa with a B.A. in physics in May of 1976. Gary completed an M.S. in electrical engineering at the University of Missouri-Columbia in August of 1977. During his studies at the University of Missouri, Gary held a research assistantship in the Bioengineering and Advanced Automation Laboratory. His research dealt with digital image analysis of congenital heart defects in chest radiographs. In September of 1977 Gary began work as a research engineer with the Environmental Research Institute of Michigan (ERIM), Ann Arbor, Michigan. The majority of his work in the Digital Image Processing Department concentrated on digital processing and analysis of high resolution synthetic aperture radar imagery. Gary was granted an extended leave of absence from ERIM in August of 1979 to pursue a Ph.D at Louisiana State University, Baton Rouge, Louisiana. During his four years at Louisiana State, Gary held a research assistantship, working for the Coastal Studies Institute at the Remote Sensing and Image Processing Laboratory. Funding for his research came from the Office of Naval Research. Gary also participated in the Maritime Remote Sensing Experiment, North Sea (MARSEN) while at Louisiana State. He assisted the Naval Research Laboratories in radar

Reproduced with permission of the copyright owner. Further reproduction prohibited without permission.

data collection from the tower Nordsee. Following the completion of his Ph.D., Gary will be employed at Sandia National Laboratories in Albuquerque, New Mexico, where he will continue his digital image processing and analysis activities.

Reproduced with permission of the copyright owner. Further reproduction prohibited without permission.

EXAMINATION AND THESIS REPORT

Candidate: Gary A. Mastin

Major Field: Engineering Science

Title of Thesis: Computer Analysis of Coastal Ocean Features in Synthetic Aperture Radar Imagery

Approved:

Major Professor and Chairman

Dean of the Graduate School

EXAMINING COMMITTEE:

Joseph N. Suhayda

S. A. Hsu

Richard K. Conner

Donald H Kuff

J. M. Coleman

Date of Examination:

May 5, 1983

Reproduced with permission of the copyright owner. Further reproduction prohibited without permission.